# BEYOND CONVENTIONAL LI-ION: AQUEOUS LI ION BATTERIES AND MIXED METAL FLUORIDE CATHODES FOR LI AND LI-ION BATTERIES

A Dissertation
Presented to
The Academic Faculty

by

Daniel Gordon

In Partial Fulfillment
of the Requirements for the Degree
Doctor of Philosophy in the
School of Materials Science and Engineering

Georgia Institute of Technology
August 2018

# BEYOND CONVENTIONAL LI-ION: AQUEOUS LI ION BATTERIES AND MIXED METAL FLUORIDE CATHODES FOR LI AND LI-ION BATTERIES

Approved by:


Dr. Gleb Yushin, Advisor
School of Materials Science and Engineering
*Georgia Institute of Technology*

Dr. Meilin Liu
School of Materials Science and Engineering
*Georgia Institute of Technology*

Dr. Faisal Alamgir
School of Materials Science and Engineering
*Georgia Institute of Technology*

Dr. Alexander Alexeev
School of Mechanical Engineering
*Georgia Institute of Technology*

Dr. Paul Kohl
School of Chemical and Biomolecular Engineering
*Georgia Institute of Technology*


Date Approved: May 18, 2018

# ACKNOWLEDGEMENTS

Thank you to my advisor, Dr. Gleb Yushin, for your guidance and support over the entire course of the PhD program. You shared your expertise and always-optimistic outlook toward challenges in countless discussions over the years. Thank you also to my other committee members – Dr. Alamgir, Dr. Alexeev, Dr. Liu, and Dr. Kohl – for your valuable feedback.

Many current and former research group members eagerly assisted with research and made working in the laboratory fun and memorable. Thank you Jim, Qiao, Ani, Dong-Chan, Ah-Young, Yiran, Martin, Rebecca, Tim, Enbo, Billy, Xiaolei, Wenbin, Sacha, Kostia, Shuchen, Michelle, Nox, Jung-Tae, Sofiane and others.

I made many great friends with classmates in MSE. The camaraderie, whether we were studying for qualifying exams or decompressing, made the graduate school experience much richer. I especially wish the best to Brian, Alex, Stefany and Judy – I hope to stay in touch!

I am of course grateful for the support of my family, who always show tremendous faith in me and cheer me on. Their support during this PhD program is just one example of that.

# TABLE OF CONTENTS

# LIST OF FIGURES

# SUMMARY

The drive to adopt clean and renewable but intermittent sources of energy, improve the longevity of portable electronic devices, and improve the cost and range of electric vehicles motivates research into advanced electrochemical energy storage devices. While commercial Li ion batteries rely on the "rocking chair" concept of Li ion storage and an organic or polymer electrolyte, other less-developed technologies promise unique benefits with regard to gravimetric and volumetric capacities, safety, rate capability, or cost. A variety of different high-capacity conversion cathode materials have lately garnered attention, including S-, Se-, Te-, Br-, I- based cathodes, $Li_2O_2$ and LiOH cathodes, and metal fluorides – the first topic of this dissertation.[1] In addition, alternative electrolytes offering features such as improved safety have been explored, including oxide and sulfide solid electrolytes and aqueous Li salt electrolytes – the second topic of this dissertation.[2-4]

Increasing the cell-level safety and capacity of Li ion batteries can have a secondary benefit of decreasing the overall cost of a battery storage system. That is, improved safety can reduce the requirement to overbuild battery systems out of safety concerns. Increased energy density means that the same energy storage capacity can be achieved with a smaller format battery system, decreasing total costs for inactive materials (such as the separator, cell casing, current collectors, etc.) and significant assembly costs.

Meanwhile, despite the promise of each of these alternative battery technologies, significant research is required to understand how to ameliorate the current disadvantages of these technologies. A successful commercial battery system must meet all performance

requirements with regard to capacity, power capability, safety, thermal stability, and others, not merely excel in one aspect. This dissertation thus focuses on identifying not only the promises of aqueous Li ion battery and metal fluoride cathode technologies, but also the origins of undesirable attributes of the state of the art technologies and possible ways to ameliorate these pitfalls.

# CHAPTER 1. BACKGROUND

## 1.1 General Theory on Behavior of Electrochemical Devices

Electrochemical energy storage devices can store energy through electron-transfer – or Faradaic – reactions, in which the oxidation state of a chemical species changes during charge/discharge, or through double-layer charging (illustrated in Figure 2), in which charged ions are attracted to/repelled from an electrically-charged surface without the transfer of electrons from one chemical species to another. A battery is a device in which most of the charge is stored through Faradaic reactions, which leads to relatively stable charge and discharge voltages (determined by the difference in the redox potential – defined later – of the electrochemical reaction at the cathode versus the redox potential of the electrochemical reaction at the anode) and relatively high charge/discharge capacity. In contrast, an electrochemical double layer capacitor (EDLC) is a device which relies on double-layer charging for energy storage, and thus charges/discharges relatively quickly but has limited charge/discharge capacity and a voltage profile similar to that of a dielectric capacitor (in which the voltage is nearly directly proportional to state of charge). Hence, with regard to choosing electrochemical energy storage devices for practical applications, high specific energy and energy storage density typically come at the trade-off of high specific power and power density, as is illustrated in Figure 1. Significant current research effort is aimed toward simultaneously increasing both the power of and total energy storage of electrochemical energy storage devices.

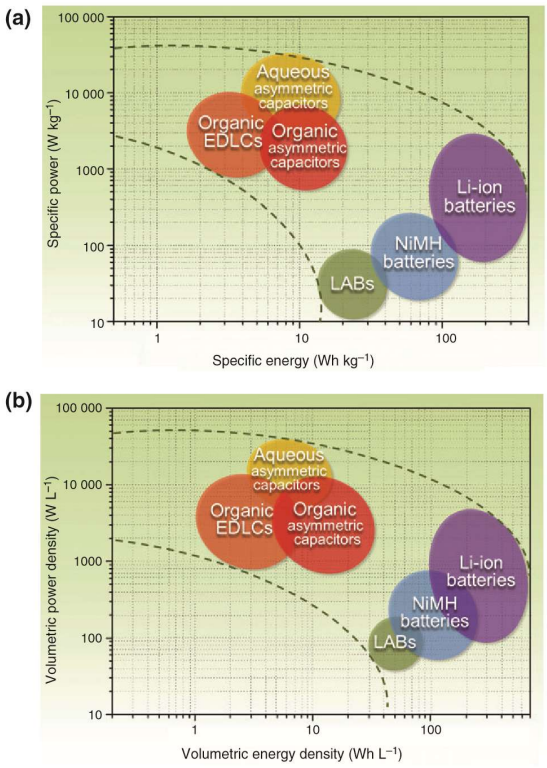


**Figure 1 Illustration of the trade-off between specific power and specific energy, or power density and energy density, of current electrochemical energy storage devices (reproduced with permission from [5])**

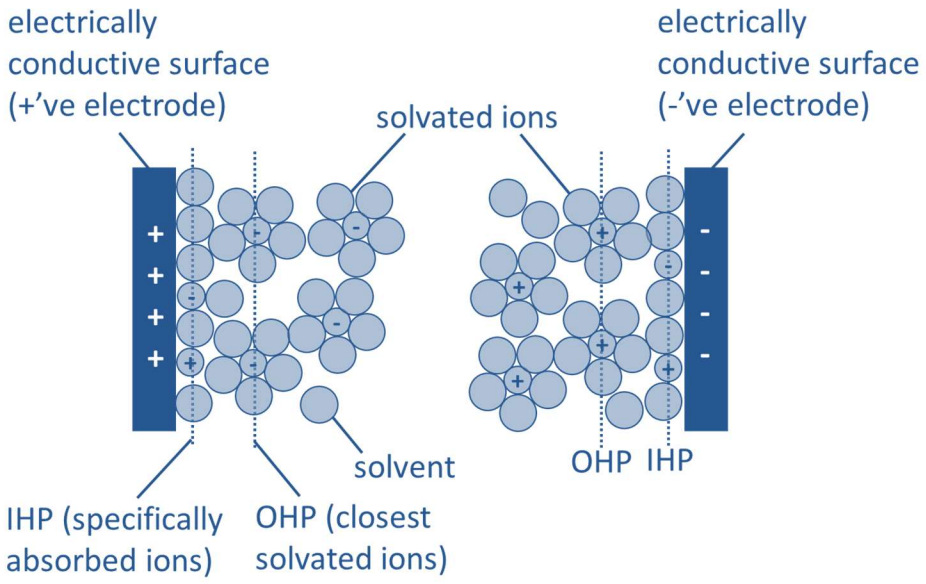


**Figure 2 Illustration of double-layer capacitance [6]**

### *1.1.1 Thermodynamics of charge/discharge*

In order to define the redox potential for an electron-transfer reaction, and to draw a connection between the Gibbs free energy change of an overall electrochemical reaction and the cell voltage, it is useful to "derive" the Nernst equation. For any electrochemical cell, the "half reaction" that takes place at the cathode can be written as:

$$\nu_{O,cathode} O_{catho} \quad + ne \rightleftharpoons \nu_{R,cathode} R_{catho} \tag{1}$$

where $\nu$'s are stoichiometric coefficients, *O* and *R* represent a species in the oxidized and reduced states, respectively, *e* represents an electron, and *n* is a positive integer. Similarly, the "half reaction" that takes place at the anode can be written as:

$$\nu_{R,anode} R_{anode} \rightleftharpoons \nu_{O,anode} O_{anode} + ne \tag{2}$$

Combining the two reactions above describes the overall (net) electrochemical reaction that takes place with the transfer of *n* electrons through the external circuit:

$$\nu_{O,catho} \quad O_{cathod} \quad + \nu_{R,anode} R_{anode} \rightleftharpoons \nu_{R,cathode} R_{cathode} + \nu_{O,anode} O_{anode} \tag{3}$$

For a battery, the cathode and anode chemistries are chosen such that the above reaction proceeds spontaneously – and is thus associated with a reduction in Gibbs free energy – going from left to right. As for any chemical reaction, we can express the change in Gibb's free energy in terms of the stoichiometric coefficients and the activities for each species (written for *n* moles of electrons transferred through the external circuit):

$$\Delta G = \Delta G_0 + RT \ln\left(\frac{{a_{R,cathode}}^{\nu_{R,cathode}} {a_{O,anode}}^{\nu_{O,anode}}}{{a_{O,cathode}}^{\nu_{O,cathode}} {a_{R,anode}}^{\nu_{R,anode}}}\right) \tag{4}$$

$\Delta G_0$ represents the Gibbs free energy change when every species is in its standard state (that is, when a = 1 for all species). Assuming conditions of constant temperature and pressure and no heat generation, the change in Gibbs free energy equals the electrical work associated with the reaction. Thus, we can also express $\Delta G$ and $\Delta G_0$ in terms of the potential difference across the electrochemical cell, $|E_{reversible}|$:

$$|\Delta G| = W_{electrical} = nF|E_{reversible}|;\ |\Delta G_0| = nF|E_{0,reversible}| \tag{5}$$

To introduce the concept of electromotive force (denoted $\varepsilon_{reversible}$), we express the equations above with $-\varepsilon_{reversible}$ substituted for $|E_{reversible}|$ as follows:

$$\Delta G = -nF\varepsilon_{reversible};\ \Delta G_0 = -nF\varepsilon_{0,reversible} \tag{6}$$

The electromotive force (EMF), $\varepsilon_{reversible}$, is positive if and only if the overall reaction proceeds spontaneously from left to right as written (since this corresponds to a negative $\Delta G$).

Combining the above equations, we derive the Nernst equation for a "full-cell":

$$\varepsilon_{reversible} = \varepsilon_{0,reversible} + \frac{RT}{nF}\ln\left(\frac{a_{R,catho}{}^{\nu_{R,cathode}} a_{O,anode}{}^{\nu_{O,anode}}}{a_{O,cathode}{}^{\nu_{O,cathode}} a_{R,anode}{}^{\nu_{R,anode}}}\right) \tag{7}$$

Note that the voltage of the cell depends on the activities (and thus concentrations) of the oxidized and reduced forms of the chemical species that take part in the reaction.

It is often convenient to refer to the redox potential for a particular electrode/electrochemical reaction versus a standard reference electrode/electrochemical reaction, such as the standard hydrogen electrode (SHE). For the SHE, protons can be

reduced to $H_2$ gas, and the reverse can take place with the oxidation of $H_2$ gas to form protons. The activities of $H_2$ and protons are both chosen to be one. Thus, the Nernst equation can be written for a hypothetical "half-cell" cell with the electrode of interest opposite the SHE:

$$\varepsilon_{reversible,half-cell} = \varepsilon_{0,reversible,half-cel} + \frac{RT}{nF} \ln(\frac{{a_R}^{\nu_R}}{{a_O}^{\nu_O}}) \quad (8)$$

where $\varepsilon_{reversible,half-cell}$ is the redox potential of the electrode of interest, $\varepsilon_{0,reversible,half-cel}$ is the standard redox potential of the electrode of interest with all species in their standard states (a = 1 for all species), and $a_R$, $a_O$, $\nu_R$ and $\nu_O$ represent the activities and stoichiometric coefficients for species reacting at the electrode of interest. Having defined half-cell potentials, one can determine the full-cell potential (EMF) for a battery with any two anode and cathode half-cell reactions from the difference in the half-cell potentials:

$$\varepsilon_{reversible,full\ cell} = \varepsilon_{reversible,anode} - \varepsilon_{reversible,catho} \quad (9)$$

### *1.1.2 Kinetics of charge/discharge*

It is also useful to address the kinetics of charge/discharge, since the Nernst equation only predicts the voltage of a battery when the electron transfer reactions and the movement of charge carriers occurs infinitely slowly or in a reversible manner. During actual charge/discharge, a variety of "polarizations" arise in a battery, causing the discharge voltage to be lower than that predicted thermodynamically and the required charge voltage to be higher than that predicted thermodynamically. Figure 3 illustrates the difference between the actual or "operating" voltage of a battery and the

thermodynamically-predicted "open-circuit" voltage. Primary contributors to the lower voltage are the Ohmic resistance of the electrolyte, the resistances to electron transfer due to the activation energies required to drive the reactions at each electrode one way or the other (identified as the "activation polarization" in Figure 3; the voltage drop associated with this resistance is called the voltage "overpotential"), and mass-transport limitations (identified as the "concentration polarization" in Figure 3).

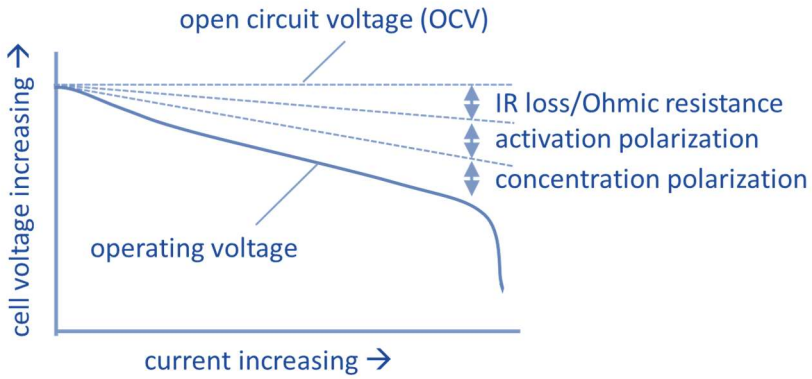


**Figure 3 Illustration of battery polarizations during discharge (adapted from [7])**

The Butler-Volmer equation analytically describes the relationship between the voltage overpotential – the difference between the actual, measured electrode potential and the equilibrium, reversible electrode potential – and the current that travels through the electrode-electrolyte interface [6]:

$$i = FAk^0[C_O e^{-\alpha\frac{F}{RT}\left(E-E^{0\prime}\right)} - C_R e^{(1-\alpha)\frac{F}{RT}\left(E-E^{0\prime}\right)}] \quad (10)$$

where $i$ is the current, $F$ Faraday's constant, $A$ the electrode area, $k^0$the standard rate constant, $C_O$ and $C_R$ the oxidized and reduced form of the chemical species, respectively, $\alpha$ the transfer coefficient (with a value between 0 and 1), $R$ the universal gas constant, $T$

temperature, and $E - E^{0'}$ the voltage overpotential. This can be derived by assuming that the activation energy to oxidize/reduce a chemical species and rate of oxidation/reduction reaction follow an Arrhenius-type relationship [6].

## 1.2 Background on Li and Li-ion batteries

Li batteries (utilizing a Li metal anode) and Li-ion batteries (utilizing a different anode material than Li metal; LIBs) shuttle $Li^+$ ions between the anode and the cathode during charge/discharge. Li is an appealing choice for the construction of a rechargeable battery for a wide variety of applications, as the light weight of Li and the wide potential difference between different redox reactions involving different Li-containing compounds and $Li^+$ ions allow for the construction batteries with relatively high specific energy and energy density. A schematic for the operation of a typical Li-ion battery is provided in Figure 4. Key components include (a) electrically-conductive current collectors, which provide a low-resistance pathway for electrons to travel between the active material and the external circuit, (b) cathode/anode electrode active materials, which reversibly store $Li^+$ ions and must be both electrically- and $Li^+$ ion-conductive, (c) polymer binder, to hold the electrode particles in close electrical contact with one another, (d) electrically conductive additive (usually C) mixed in with the electrode active material particles, (e) ionically-conductive but electrically-insulative electrolyte, which allows $Li^+$ ions to travel between the anode and cathode and (f) a porous polymer separator to prevent electrical shorting of the battery cell. Each of these components is discussed in more detail below.

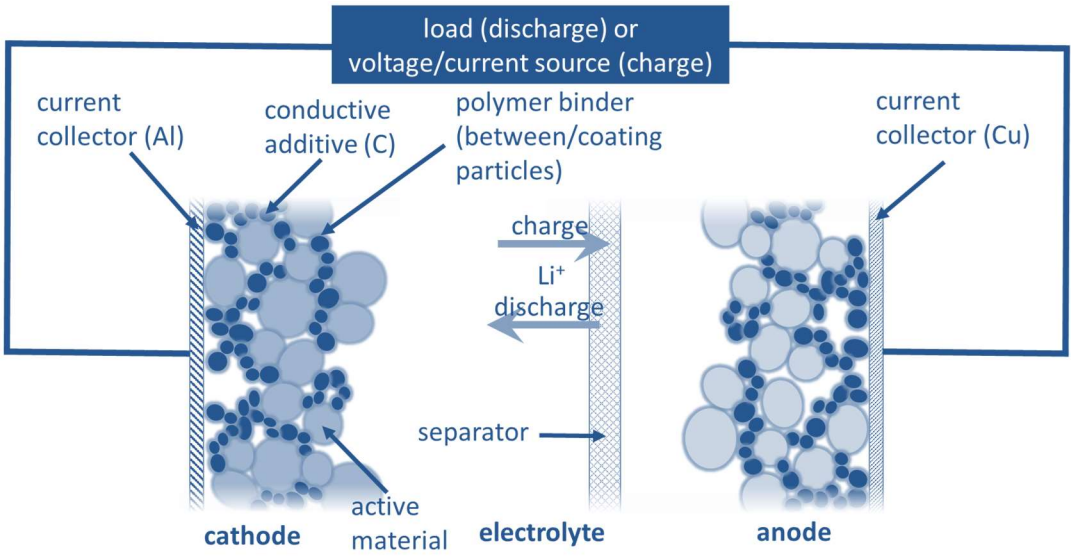


**Figure 4 Schematic of a typical lithium ion battery**

### *1.2.1 Active materials*

Redox reactions for LIBs fall under one of three broad categories depending on the chosen electrode chemistry, although only intercalation reactions have been employed commercially until recently: (a) intercalation reactions, in which a $Li^+$ ions occupy vacancies in the host compound and can be intercalated/inserted and deintercalated/deinserted without dramatic chemical or structural transformation of the host compound (such as $Li^+$ ions in $Li_xFePO_4$ where $0 \leq x \leq 1$; see Figure 5), (b) conversion reactions, in which chemical bonds of the active material are broken and new bonds are formed (such the transformation of rutile-structured $FeF_2$ to rocksalt-structured LiF and Fe metal, and visa versa; see Figure 6), and (c) alloying reactions between Li and a metal or semiconductor (e.g. for Li with Si, Ge, Sn, and variety of other elements).[8, 9] Today's commercial LIBs primarily utilize intercalation compounds, in part due to their typically small volumetric changes during charge/discharge – which prevents physical separation

and thus electrical isolation of active material and which enables stable solid electrolyte interphase (SEI) formation – and due to their channels for rapid Li ion diffusion which enable high charge/discharge rate capability.[8, 9] For the cathode, commercial intercalation compounds include $LiFePO_4$ or "LFP," $LiCoO_2$ or "LCO," $LiMn_2O_4$ or "LMO," $LiNi_{0.33}Mn_{0.33}Co_{0.33}O_2$ or "NMC," and $LiNi_{0.8}Co_{0.15}Al_{0.05}O_2$ or "NCA." Each of these materials has its tradeoffs. LFP, for instance, has a lower electrode potential than LCO (leading to a lower voltage battery), yet it is also more thermally stable and avoids the use of toxic Co. Under heating, LFP is not prone to release $O_2$ gas like LCO, which helps to avoid the hazards of cell ruptures and fires. A typical commercial anode consists of graphitic C, in which $Li^+$ ions are stored between the graphitic planes (one $Li^+$ can be stored per six C atoms), or $Li_4Ti_5O_{12}$ (lithium titanate or "LTO") for ultra-high current batteries.

The development of LFP touches on some general themes in the development of suitable active material particles for LIBs. LFP was first reported as a member of a class of phospho-olivine compounds (also including $LiMnPO_4$ and $LiNiPO_4$) for LIBs by Padhi et al. in 1997.[10] In order to improve LFP's electrochemical performance to practically utilize it in LIBs, several approaches have been taken to address the low intrinsic ionic and especially electronic conductivities. Extensive studies have been performed on synthesis methods to reduce particle size/distances of solid-state $Li^+$ ion diffusion, apply conductive carbon coatings and subsequent electrochemical performance. [11-13] Also discussed are isovalent and aliovalent substitutions to the compound.[14] These developments have enabled high capacity even at high charge/discharge rates (even ~30C in the literature) and have been successfully employed commercially.

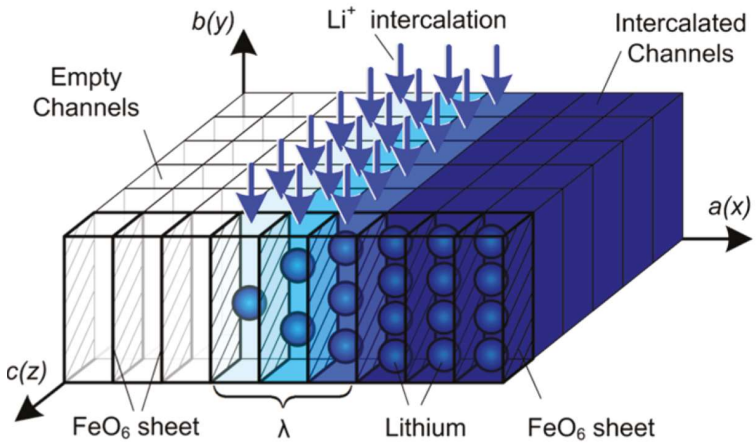


**Figure 5 Illustration of Li intercalation into $Li_xFePO_4$ (reproduced with permission from [15])**

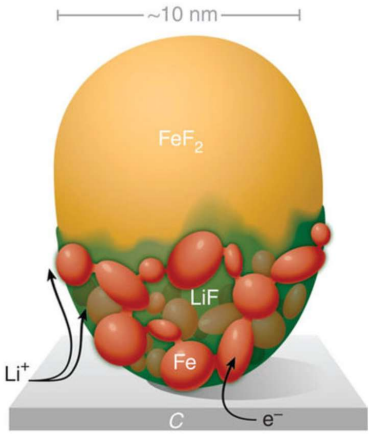


**Figure 6 Illustration of conversion reaction of $FeF_2$ into LiF and Fe metal (reproduced with permission from [16])**

### *1.2.2 Electrolyte*

A variety of characteristics are desired for Li ion battery electrolytes, including a high ionic conductivity, low viscosity, high dielectric constant, good wettability of the electrodes and separator, low melting point, high boiling point, high flash point, wide

potential stability window, low cost and environmental friendliness. [17, 18] A typical electrolyte is composed of a lithium salt and several different solvents to achieve these characteristics. $LiPF_6$ salt is the most popular commercial lithium salt and alkyl carbonates the most commonly chosen solvents. [17, 18]

While organic electrolytes are not typically entirely stable at the relatively high and low electrode potentials of commercial LIB electrode materials, they are also chosen for their ability form a stable solid-electrolyte-interphase (SEI) layer on the electrode surfaces, preventing further electrolyte decomposition while not impeding the transport of $Li^+$ ions.[18] This Li-permeable, electrically insulative layer forms during the first several charge-discharge cycles, and leads to limited irreversible "loss of Li" or exclusion of Li from taking part in electrochemical reactions due to its incorporation in the SEI layer (for instance, in the form of LiF). An illustration of a typical SEI layer is shown in Figure 7. The layer consists of decomposed organic solvent, additives and electrolyte salt, and can vary in composition from one location to another. In order to form a stable SEI layer on the anode, ethylene carbonate has been found to be a necessary component of the solvent mixture. [17, 18] In addition, a small portion of fluoroethylene carbonate (FEC) or vinylene carbonate (VC) are commonly added to help form a suitable SEI layer. During electrochemical cycling, FEC decomposes into VC and LiF, while VC decomposes in each case to form $HCO_2Li$, $Li_2C_2O_4$, $Li_2CO_3$, and polymerized VC.[19]

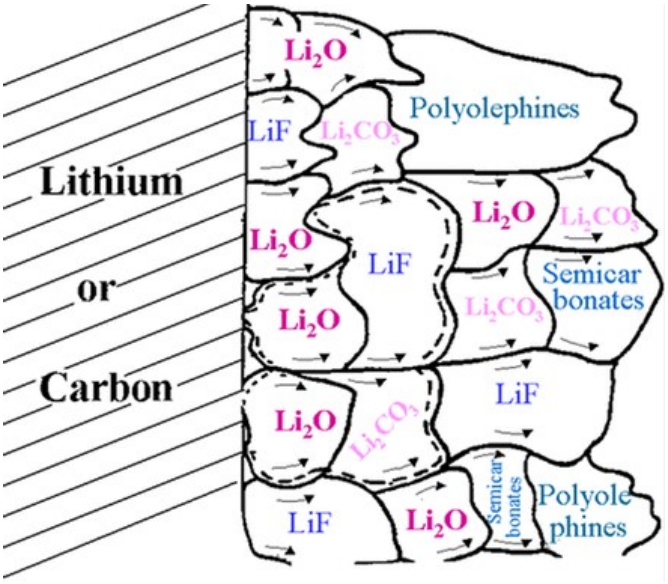


**Figure 7 Illustration of solid electrolyte interphase (SEI) formation with organic electrolyte (reproduced with permission from [20])**

### *1.2.3 Separator*

Most separators in the commercial battery market are porous polyolefin membranes (polyethylene or polypropylene) with ~15-32 micron thickness and ~38-45% porosity. [21] After production via either a standardized "wet" or "dry" process, they are often treated with surfactants or plasma-treated to allow them to be easily wetted by the electrolyte. [21] In this thesis, such membranes optimized for Li ion battery applications were obtained from Celgard. Aqueous electrolyte experiments were instead conducted with a glass fiber membrane, suitable due to the ease with which it wets with water.

### *1.2.4 Current Collectors*

The current collector of choice for the cathode in commercial LIBs is Al foil. Although Al is thermodynamically unstable at the high electrode potentials of popular

cathode materials (~3.5V-4.2V vs. $Li/Li^+$), a bare Al surface can be passivated through reactions with $LiPF_6$ decomposition products and trace water content – forming on the surface passivating layers including such phases as LiF, $Al_2O_3$, and $AlPO_4$.[22] [23] Since Al cannot be used for low-potential anode materials as it will electrochemically alloy with Li, Cu foil is popularly used for the anode current collector. Note that neither of these metal current collectors were found to be suitable for the construction of Li ion batteries with the high salt concentration aqueous electrolytes explored in this thesis due to severe corrosion. Thus, stainless steel and titanium current collectors were used for the "proof of concept," recognizing that cheaper and lighter alternatives may need to be explored in the future.

### *1.2.5 Conductive Additives*

The high electrical and thermal conductivities of various carbons make them a virtually ubiquitous feature of battery electrodes. Many electrode active materials have insufficient electrical conductivity leading to extremely high polarization or electrochemical isolation of active material particles without the use of an electrically-conductive additive. Although electrochemically inactive, C additives provide the necessary highly-conductive pathways for electrons to travel through the electrode. Heat dissipation is critical, as well, as the energy lost to the various internal resistances in a battery cell is dissipated in the form of heat. Efficient heat dissipation is important to prevent decomposition of active materials and electrolyte. The popular forms of carbon used are graphite and carbon black powders.[24] More recently, single walled carbon nanotubes (SWCNTs) have also been marketed as a substitute C additive (such as Tuball$^{TM}$ produced by OCSiAl LLC).

The amount of C used in a battery electrode should be minimized in order to reduce the inactive mass fraction and volume fraction of the electrode and thus overall weight and size of the battery. However, as commonly illustrated in a percolation curve, a critical volume fraction of C additive is required to realize the benefits with regard to increased electrical interconnectivity/decreased overall resistance of an electrode. That is, below a critical amount of C additive there is little beneficial effect and above the same critical amount there are diminishing returns. Due to their high aspect ratios and excellent ability to conduct current through the electrode, typically only a small volume or mass fraction of carbon nanotubes is required in an electrode to lend it sufficient electrical conductivity. Figure 8 illustrates the benefits of adding various mass fractions of single-walled carbon nanotubes to a nano-sized lithium titanate electrode. Between ~5-10 wt. %, a dramatic benefit in capacity is realized due to the increase in overall electrical connectivity of the electrode. The optimum CNT content depends strongly on the size and shape of the particles, type of binder and other slurry and electrode parameters and may be as little as 0.1-0.3 wt. %.

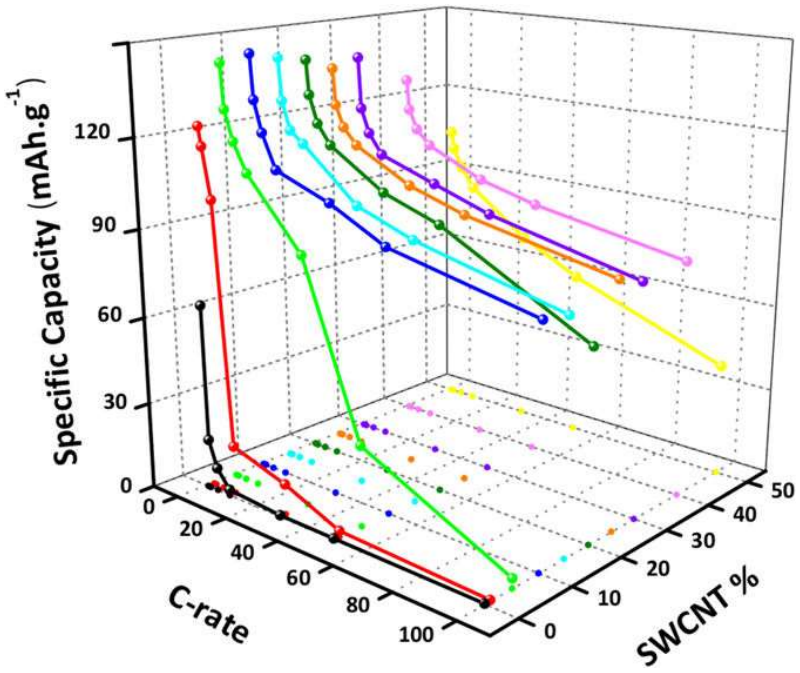


**Figure 8 Specific capacity as a function of SWCNT mass percent and C-rate for nano-lithium-titanate-single-walled-carbon-nanotube Li ion battery electrodes (reproduced with permission from [25])**

### *1.2.6 Polymer Binder*

The polymer binder holds the active material particles and conductive additive in close contact with one another and the current collector in order to maintain electrical connectivity. Battery electrodes are commonly produced by casting a slurry of polyvinylidene difluoride (PVDF) dissolved in N-methylpyrrolidine (NMP) and suspended active material and conductive additive particles onto the metal current collector. Recently, PVDF and NMP have been partially substituted with more health- and environmentally-friendly styrene butadiene copolymer (SBR) dissolved in water. It is important to recognize that the swelling and mechanical properties of the binder have an impact on the electrochemical performance. Namely, PVDF swells as much as 30 wt. % in organic electrolyte, which has the beneficial effect of allowing Li ion transport through the binder

but a detrimental effect on the mechanical binding properties. [26] SBR swells in organic electrolytes a much more limited amount than PVDF. [26]

### 1.3 Aqueous Li-Ion Battery Chemistry

Aqueous Li-ion batteries (ALIBs) employ an aqueous electrolyte in place of a conventional organic electrolyte. Lithium salts that have been explored in the literature for use in aqueous electrolyte include $Li_2SO_4$, $LiNO_3$, LiCl, LiOH, and LiTFSI.[27-44] There are numerous potential advantages in the choice of an aqueous electrolyte: water is non-toxic and nonflammable, ameliorating common safety and environmental concerns associated with organic solvents in organic electrolyte LIBs.[45, 46] The conductivity of aqueous electrolytes is also relatively high, up to several orders of magnitude higher than that of common organic electrolytes.[47] In principle, this may enable the construction of batteries with ultra-thick electrodes to enable higher practical energy storage densities, or ultra-high-power batteries that charge and discharge at faster rates.

However, there are several significant challenges to the development of a practical ALIB. Firstly, pure water is only thermodynamically stable over an approximately 1.23V window, the position of which depends on the pH value (as commonly illustrated in a Pourbaix diagram). This is particularly problematic since aqueous Li-salt electrolytes do not commonly decompose to form a passivating SEI layer. The absence of such an electrically insulative SEI layer allows continued rapid decomposition of water into $O_2$ and $H_2$ gases at electrode potentials outside of the window of thermodynamic stability for water. Figure 9 illustrates the potentials of $O_2$ and $H_2$ evolution for pure water as a function of pH, provided as an approximation of the potentials of aqueous electrolyte

decomposition. It further illustrates the electrode potentials for common LIB electrode materials, many of which exceed the upper or lower limits of thermodynamic stability for water. $O_2$ evolution becomes exponentially more severe (as predicted by the Butler-Volmer equation) as the electrode potential is increased beyond the potential indicated in the diagram. Similarly, $H_2$ evolution becomes exponentially more severe as the electrode potential is lowered below the potential indicated in the diagram.

Electrolyte decomposition can adversely affect the operation of the battery in numerous ways. Firstly, decomposition of the electrolyte can eventually lead to loss of an ionically-conductive medium for $Li^+$ ion transport. Secondly, currents associated with electrolyte decomposition can make it difficult to charge the battery and lead to poor Coulombic efficiency. Thirdly, local pH changes near the electrode surface resulting from water decomposition can lead to instability of the electrode active materials. [43] Fourthly, $O_2$ and $H_2$ bubbles formed on the electrode surface can effectively create an ionically insulative barrier to $Li^+$ motion. Finally, gas evolution can lead to mechanical disintegration of the electrode.

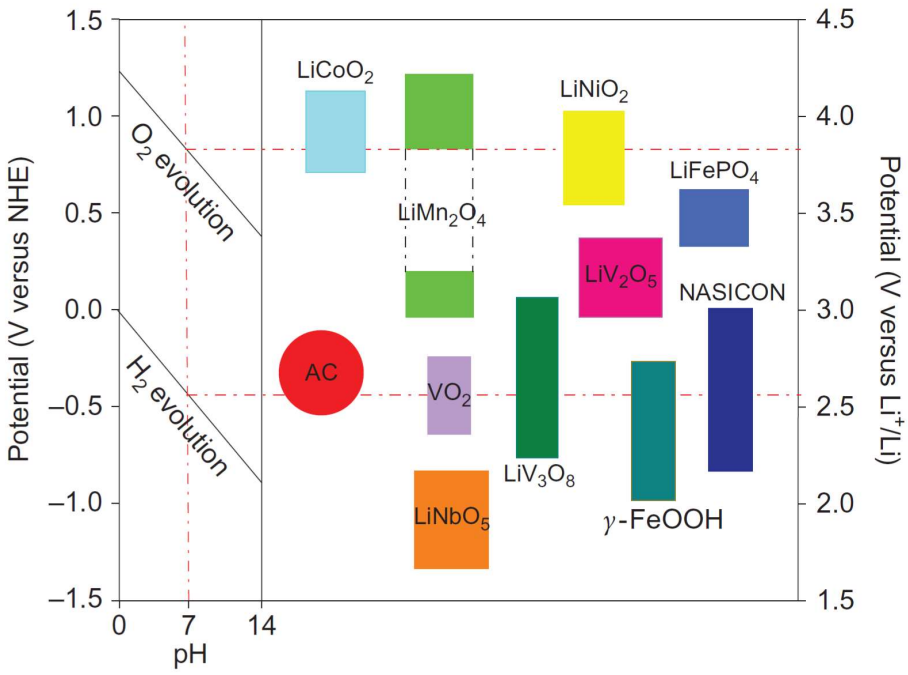


**Figure 9 Diagram of common LIB electrode potentials and $O_2$ and $H_2$ evolution potentials for water (reproduced with permission from [48])**

Although the research is in the nascent stage, the choice of electrolyte salt and salt concentration has been shown to affect the potential of aqueous electrolyte decomposition, or enable the formation of a passivating surface layer similar to that of an organic electrolyte cell. For high salt concentrations, the activity of water is decreased along with the fraction of free water molecules. LiTFSI has garnered attention as an aqueous electrolyte salt due to its stability in water and very high solubility.[43, 44] Notably, Suo et al. show that increasing the concentration of LiTFSI, leads to decreased $H_2$ and $O_2$ evolution. [43] Furthermore, Suo et al. report that LiTFSI can decompose on the surface of an electrode in an aqueous electrolyte to form a LiF passivating surface layer, similar to an organic electrolyte, which may further reduce $H_2$ and $O_2$ evolution.[43] Building on the concept of a "water-in-salt" battery, Suo et al. demonstrate that the addition of a second

salt to create a “water-in-bisalt” electrolyte can further reduce the water activity and increase the stability of the aqueous electrolyte.[49] This enabled the construction of a 2.5V battery with C-coated $TiO_2$ and $LiMn_2O_4$ as anode and cathode materials, respectively. Such a concept was additionally demonstrated with $LiVPO_4F$ as the active material for both the cathode and the anode, since it can accommodate up to two Li ions per V ion.[50] The cathode reaction is associated with the transition between $VPO_4F$ and $LiVPO_4F$ and the anode reaction is associated with the transition between $LiVPO_4F$ and $Li_2VPO_4F$. Yamada et al. demonstrate the benefit of ultra-low water activity of a hydrate melt electrolyte. They successfully cycle a battery relying on such an electrolyte with $Li4Ti5O_{12}$ as a relatively high capacity, low electrode potential anode.[51]

Others have investigated the assembly of an aqueous Li ion battery with an interfacial layer between an electrode of very low potential and the aqueous electrolyte, enabling the use of anodes such as Li metal.[46, 52]. For instance, Wang et al. utilize a combination of a LISICON film and gel polymer electrolyte on the surface of a Li metal anode.[52] This prevented the generation of $H_2$ gas when the coated electrode was placed in contact with $Li_2SO_4$ aqueous solution, yet allowed for the transport of $Li^+$ ions to enable a high voltage aqueous lithium ion battery to function.

A second category of challenges in the development of ALIBs is the instability of the electrode active materials in contact with aqueous electrolyte. Side reactions between the electrode active material and oxygenated aqueous electrolyte may possibly lead to deintercalation of $Li^+$ ions from the electrode material, as projected by Luo et al. [48]. They predict that at a single electrode surface (without current travelling through the

external circuit), $Li^+$ deintercalation will spontaneously occur in conjunction with oxygen reduction in the following overall reaction:

$$Li(intercalated) + (1/4)O_2 + (1/2)H_2O \leftrightarrow Li^+ + OH^- \quad (11)$$

Luo et al. also predict that $Li^+$ deintercalation can spontaneously occur with water reduction at even lower electrode potentials in the following overall reaction:

$$Li(intercalated) + H_2O \leftrightarrow Li^+ + OH^- + (1/2)H_2 \quad (12)$$

They present data that suggests that eliminating the presence of dissolved oxygen dramatically increases the cycle stability of the electrode active materials. Other side reactions between the electrode active materials and the electrolyte which may give rise to diminished capacity include dissolution of the active material into the electrolyte (which may depend on the solution pH) and $H^+$ intercalation instead of $Li^+$ intercalation. [53] For instance, NMC and LCO have been found to allow significant $H^+$ cointercalation. [53] Subsequent to the research presented in this thesis, $LiCoO_2$ was found to form a resistive layer of Co(II)O on the particle surfaces.[54] The layer thickness and deleterious effects on cycle stability could be lessened by reducing water activity through the use of high Li salt concentrations.

### 1.4 Metal Fluoride Conversion Cathodes for Li- and Li-Ion Batteries

Commercial intercalation cathode materials are only able to accommodate a maximum of one $Li^+$ ion per transition metal ion in the cathode material, while C and LTO anodes have similarly small volumetric and gravimetric $Li^+$ ion storage capacities. By contrast, conversion materials or alloying materials can store significantly more $Li^+$ ions

per unit mass or unit volume. Metal fluorides, in particular, can accommodate two or three $Li^+$ ions per transition metal ion, giving rise to very high gravimetric and volumetric capacities. Calculated values for the redox potentials of the reactions and gravimetric and volumetric capacities are displayed in Figure 10. When paired with a high-capacity anode such as Si or Li metal, the benefits with regard to unit stack-normalized energy density are fully realized, as illustrated in Figure 11. This measurement estimates the energy density taking into account the volume of the internals of the battery – the current collectors, active material layers, and separator – while forgoing the added volume of the cell casing and other components of a battery system for ease of calculation. Notably, several other assumptions are also made, such as the suitable ratios of the active materials to inactive C additive and polymer binder.

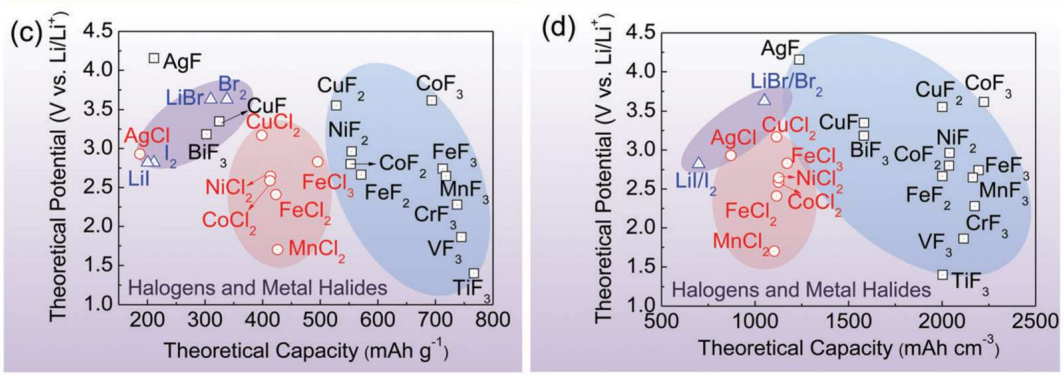


**Figure 10 Theoretical potentials and capacities of ionic compounds for LIBs (reproduced with permission from [1])**

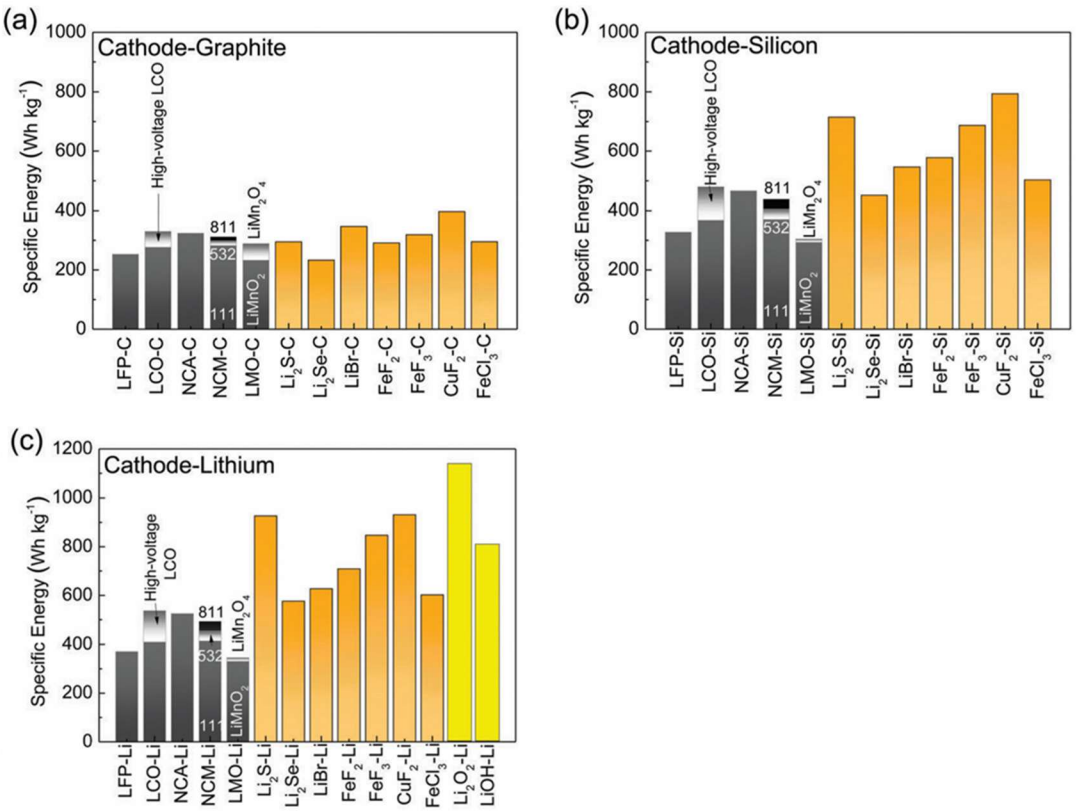


**Figure 11 Unit stack-normalized volumetric capacities (reproduced with permission from [1])**

Ideally, a cathode may be produced with $CuF_2$ due to its relatively high theoretical electrode potential versus other metal fluoride compounds, high theoretical capacity, and exclusion of toxic Co. However, to-date, studies on the electrochemical behavior of $CuF_2$ have shown that the lithiation reaction is highly irreversible. Thus, a variety of other research studies have focused on compounds such as $FeF_3$, $FeF_2$, and $CoF_2$, which undergo more reversible reactions yet still have attractive electrode potentials and theoretical capacities. These studies may ultimately provide useful knowledge for tackling the irreversibility observed with $CuF_2$ cathodes.

On discharge of a battery with a metal fluoride cathode, the metal fluoride undergoes a conversion reaction with $Li^+$ to form (fully-reduced) metal (M) and LiF phases (read left to right for the cathode half reaction during battery discharge):

$$MF_2 + 2Li^+ + 2e^- \leftrightarrow M + 2LiF \quad (13)$$

or

$$MF_3 + 3Li^+ + 3e^- \leftrightarrow M + 3LiF \quad (14)$$

The resulting morphology is typically observed to comprise of fine metal nanoparticles among a "sea" of smaller LiF crystals, as illustrated in Figure 6.

Despite their theoretical promise, metal fluorides suffer from a relatively large voltage hysteresis and poor capacity retention in experimental studies of their charge-discharge behavior. For intercalation materials, voltage plateaus for charge and discharge may be very close in potential. For instance, for a half-cell comprising of a $LiFePO_4$ cathode and Li metal counter electrode, the charge and discharge plateaus are separated by a voltage difference on the order of ~100 mV (see Figure 28g). In contrast, typical charge/discharge plateaus for metal fluoride cathodes are displayed in Figure 12. The separation between the charge and discharge voltages is on the order of 1V.

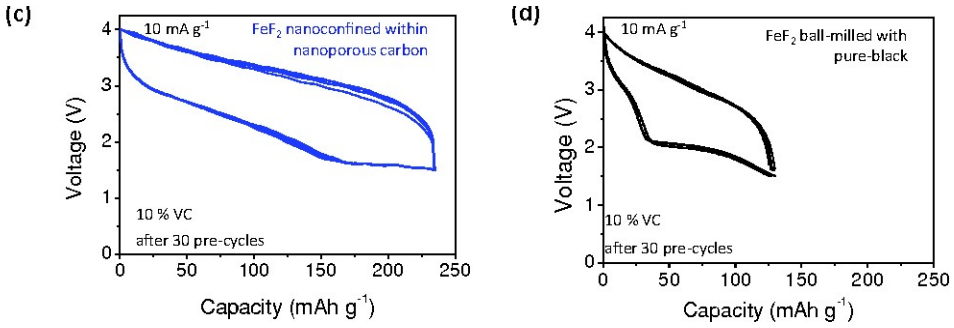


**Figure 12 Charge-discharge voltage profiles for $FeF_2$ either nanoconfined in porous C or ball-milled with PureBlack® C (reproduced with permission from [55])**

# CHAPTER 2. METHODS

## 2.1 Electrochemical Impedance Spectroscopy (EIS)

Electrochemical impedance spectroscopy (EIS) can be used to probe the resistances, capacitances and inductances within a battery system to help determine the causes of better/worse battery performance with respect to capacity retention, rate capability, voltage hysteresis, etc. A sinusoidal voltage is applied to an electrochemical cell over a range of different frequencies (sequentially) and the phase difference and the amplitude of the resulting sinusoidal current are measured. The complex impedance – giving the phase and amplitude relationship between the voltage and current – as a function of the oscillation frequency is commonly plotted in a Nyquist plot, where the horizontal and vertical axes represent the real and imaginary components of the impedance, respectively. With an appropriately chosen equivalent circuit that well-describes the physical phenomena occurring in the electrochemical cell, values for the charge transfer resistance, double layer capacitance, etc. can be determined by fitting an equation for the equivalent circuit impedance to the experimental data.

A simple equivalent circuit used to describe a battery is the Randles circuit (see Figure 13), which corresponds with the Nyquist impedance plot illustrated in Figure 14. The equivalent series resistance is the sum of the solution resistance of the electrolyte and electrical resistance of the leads, current collector, and active material layer. The capacitance represents the double layer (non-faradaic) charging at the electrode-electrolyte interface, while the charge transfer resistance represents the resistance for driving faradaic electrochemical reactions. These two circuit elements are chosen to be in parallel since

current can travel through the battery at the electrolyte-electrode interface simultaneously via faradaic reactions and double-layer charging. The Warburg impedance is an element that simulates the mass-transport limitations in the device.

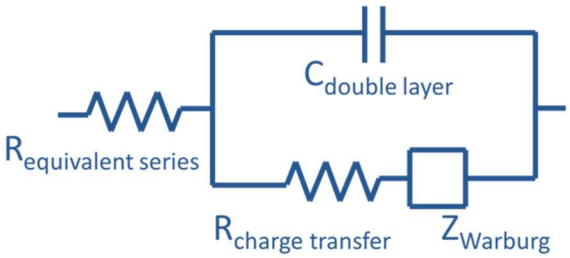


**Figure 13 Randles equivalent circuit**

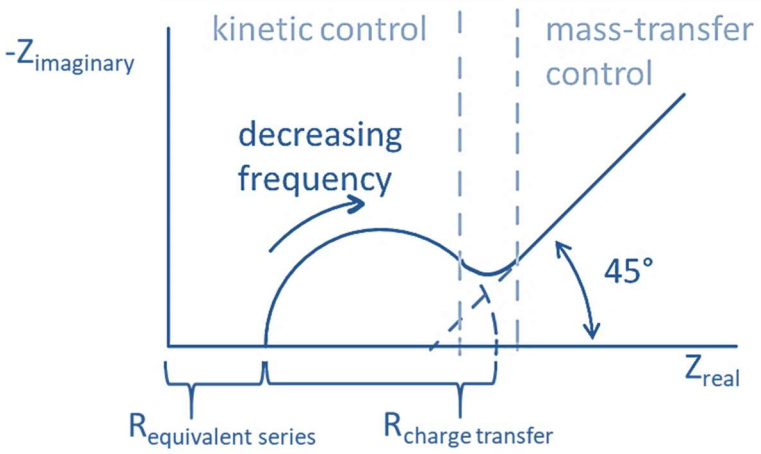


**Figure 14 Nyquist impedance plot for a Randles equivalent circuit (adapted from [6])**

Illustrating how the circuit in Figure 13 gives rise to the Nyquist plot in Figure 14 requires a brief review of phasors and complex impedance. Commonly, sinusoidal waves of the same frequency are represented as phasors, which are vectors that have magnitudes equal to the amplitudes of the waves they represent and which rotate 360° in a 2-D complex plane at the waves' frequency. The phase difference between two waves is represented by

the phase angle maintained between the phasors. The magnitude of a wave at a particular point in space as a function of time can be determined by projecting its phasor onto a chosen fixed axis. The complex impedance (Z) defines the relationship between the oscillating voltage and current when they are described using phasors (*E* and *I*, respectively):

$$E = IZ \tag{15}$$

In this case, we choose to project the phasors onto the horizontal real axis to determine the magnitude of the current and the voltage at a fixed point in space. As for any complex number, we can write:

$$Z = Z_{real} + iZ_{imaginary} = Ze^{i\varphi} \tag{16}$$

Here, $\varphi$ represents the phase angle, Z the magnitude of the complex impedance, and $Z_{real}$ and $Z_{imaginary}$ the real and imaginary components of Z. An inspection of the amplitude and phase relationships between voltage and current give rise to the following equations for the complex impedance of individual circuit elements:

$$\text{Resistor: } Z = R, \text{ where R is a real number} \tag{17}$$

$$\text{Capacitor: } Z = -i/(\omega C), \text{ where } \omega \text{ is the oscillation frequency (in rad/s) and C is the capacitance} \tag{18}$$

Since a resistor has no frequency dependence, it is represented in a Nyquist plot by a single point on the real axis (see Figure 15). A capacitor, however, is represented by a line on the imaginary axis where each point corresponds to the impedance at a particular oscillation frequency (see Figure 15).

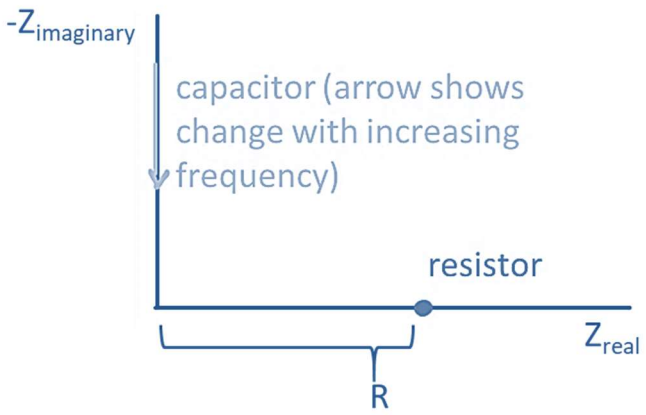


**Figure 15 Nyquist plot for an ideal resistor and for an ideal capacitor**

When two circuit elements are connected in series, the total impedance is simply the sum of the individual impedances:

$$Z_{total} = Z_1 + Z_2 \tag{19}$$

When two circuit elements are connected in parallel, the total impedance is determined as follows:

$$\frac{1}{Z_{total}} = \frac{1}{Z_1} + \frac{1}{Z_2} \tag{20}$$

Thus, for a capacitor and resistor in parallel:

$$Z_{total} = \frac{1}{\frac{1}{Z_{resistor}} + \frac{1}{Z_{capacitor}}} \tag{21}$$

$$Z_{total} = \frac{1}{\frac{1}{R} + \omega Ci} \tag{22}$$

For $\omega \rightarrow 0$, $Z_{total} \rightarrow R$. For $\omega \rightarrow \infty$, $Z_{total} \rightarrow 0$. Over a range of frequencies, the Nyquist plot forms a semicircle where each point represents the impedance at a particular

frequency (see Figure 16). Adding a resistor in series with the resistor-capacitor loop shifts the semicircle to the right by the magnitude of this additional resistance. This produces a plot similar to Figure 14 for the kinetically-controlled region.

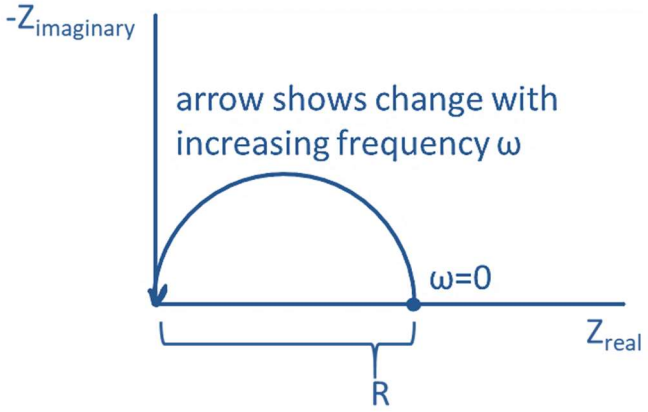


**Figure 16 Nyquist plot for a resistor-capacitor loop (resistor and capacitor in parallel)**

## 2.2 Cyclic voltammetry (CV)

To obtain a cyclic voltammogram (CV), the voltage of a working electrode versus a reference electrode is swept at a constant rate between two potential limits and repeated for multiple cycles while the current is measured. This is contrast to charge-discharge, in which the current is fixed and the changing, uncontrolled voltage is measured. For the purpose of understanding the features of a CV (typically plotted as current versus voltage), it is useful to understand the profile for an ideal R-C circuit in which a resistor and capacitor are in series. This is a useful analogy for the behavior of a double layer capacitor, in which the resistor is the equivalent series resistance and the capacitor the capacitance of the double-layer. Figure 17 displays the CV for an R-C circuit.

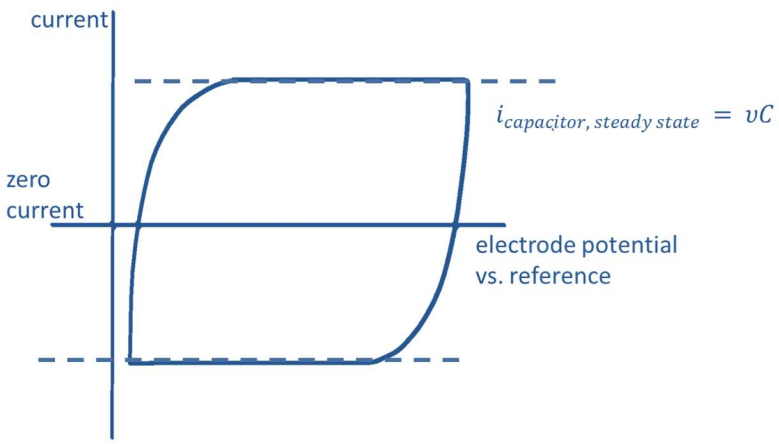


**Figure 17 Cyclic voltammogram for an R-C circuit [56]**

The magnitude of the steady state current value that is asymptotically approached as the voltage sweeps in a particular direction is given by:

$$i_{capacitor,\ stead\ \ state} = \upsilon C \tag{23}$$

where υ is the scan rate. Notably, the steady state current is directly proportional to the scan rate. In contrast, the peak currents generated by reversible faradaic reactions (illustrated in Figure 18) vary with the square root of the scan rate according to the Randles–Sevcik equation [6]:

$$i_{faradaic,\ peak} = 0.4463\ (\frac{F^3}{RT})^{1/2} n^{3/2} A D^{1/2} C^* \upsilon^{1/2} \tag{24}$$

In this equation, $F$ is the Faraday constant, $R$ is the gas constant, $T$ is the temperature, $n$ is the number of electrons transferred, $A$ is the electrode surface area, $D$ is the diffusion coefficient, $C^*$ is the concentration, and $\upsilon$ is the scan rate.

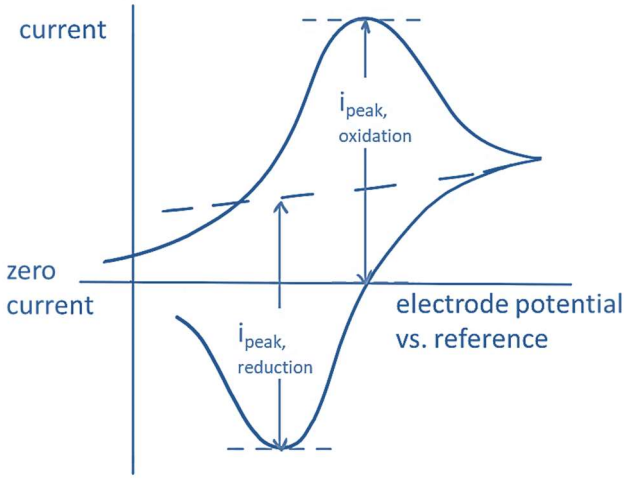


**Figure 18 Illustration of a Faradaic oxidation peak during a linear voltage sweep (adapted from [6])**

Dividing the expressions for $i_{faradaic,\ peak}$ and $i_{capacitor,\ steady\ state}$, we see that the ratio of the peak current for a faradaic reaction to the steady state current for double layer charging varies with $\upsilon^{-1/2}$ :

$$\frac{i_{faradaic,\ peak}}{i_{capacitor,\ steady\ state}} \propto \upsilon^{-1/2} \tag{25}$$

This means that for an electrode-electrolyte interface that exhibits both faradaic charge transfer reactions and double layer charging, the faradaic charge-transfer behavior is more apparent at slow scan rates (as $\upsilon \to 0$, $\frac{i_{faradaic,\ peak}}{i_{capacitor,\ steady\ state}} \to \infty$) while the capacitive behavior is more apparent at fast scan rates (as $\upsilon \to \infty$, $\frac{i_{faradaic,\ peak}}{i_{capacitor,\ steady\ state}} \to 0$).

## 2.3 Charge-Discharge (C-D)

Constant-current charge-discharge (C-D) can be used to simulate the use of a battery under near real-world conditions. This is performed using a galvanostat, a device which can regulate a current while measuring the voltage across two leads. (In contrast, a potentiostat is a device in which the voltage across two leads is regulated and resulting current is measured.)

It is convenient to refer to rates of charge and discharge in terms of the total time it would take for a full charge or discharge of a battery or in terms of the C-rate. A C-rate of 1C corresponds with the constant current required to fully charge or discharge a battery in 1 hour. A rate of C/20 or 5C represents constant current required to fully charge or discharge a battery in 20 hours or 12 minutes, respectively.

## 2.4 Scanning Electron Microscopy (SEM)

In this thesis, scanning electron microscopy was especially useful for observing the size and morphology of the fresh active materials, the distributions of active material, binder, conductive additive and open volume (porosity) in fresh electrodes, and changes in particle morphology and particle surfaces following C-D.

## 2.5 Transmission Electron Microscopy (TEM)

In this thesis, transmission electron microscopy complemented SEM in observing the size and morphology of fresh active materials. It uniquely provided the capability to observe changes to the active material particle surfaces, such as the formation of

amorphous surface layers on LFP of just several nanometers thickness after cycling with aqueous electrolyte.

## 2.6 Energy Dispersive Spectroscopy (EDS)

Energy dispersive spectroscopy (EDS) can be performed during SEM or TEM to quantitatively or semi-quantitatively determine the elemental composition of a material. With the exception of light Li, He and H, most other elements can be easily detected. EDS functions by emitting X-ray photons toward the sample, which upon hitting the sample excite electrons in innermost shells of the electron clouds and leave behind holes for more outer-shell electrons to refill. The transition of an electron from a more outer shell to a more inner shell is accompanied by the emission of an X-ray photon, of energy equal to the change in energy for the electron which transitioned between shells. This is illustrated in Figure 19. Since the energy levels for each element are (for the most-part) unique to that element, measuring the energy of emitted X-rays can indicated the presence of a particular element. The technique is limited only by overlapping energies for electron energy shell transitions for multiple elements, and the fact that X-rays emitted have varying energies and can be reabsorbed to differing degrees by the sample before escaping. Thus, a correction to the raw data (depending on the sample type) is required to make a highly quantitatively-accurate estimations of elemental composition.

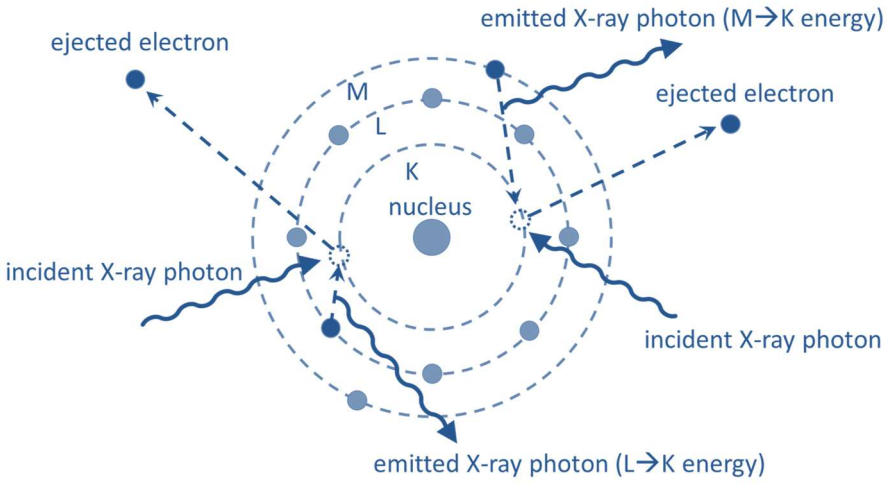


**Figure 19 Illustration of energy dispersive spectroscopy (EDS)**

## 2.7 X-ray Diffraction (XRD)

Powder X-ray diffraction (XRD) is employed as a bulk analysis technique, as the sample is ground-up/homogenized and the incident X-rays easily penetrate and diffracted X-rays escape from particles with diameters on the order of several microns. Powder XRD can be used to determine the crystal structures present in a sample and the associated unit cell dimensions. Incident X-rays are scattered off of the crystal lattice planes as shown in

Figure 20 and constructively interfere for particular values of $2\theta$ dependent on the interplanar spacing $d$ according to Bragg's Law (here $n$ is an integer and $\lambda$ is the X-ray wavelength):

$$n\lambda = 2d\sin\theta \tag{26}$$

Each diffraction peak can be attributed to constructive interference from a particular set of crystal lattice planes (e.g. 110 planes, or 111 planes, etc.). In addition to the peak angles allowing one to back-calculate the spacing between the lattice planes, broadening

of the diffraction peaks can indicate a breakdown of long-range lattice order, for instance, due to variations in the lattice parameter in different locations in the sample due to compositional variations, the presence of any defects such as dislocations or stacking faults, or inhomogeneous stress and strain in the sample.

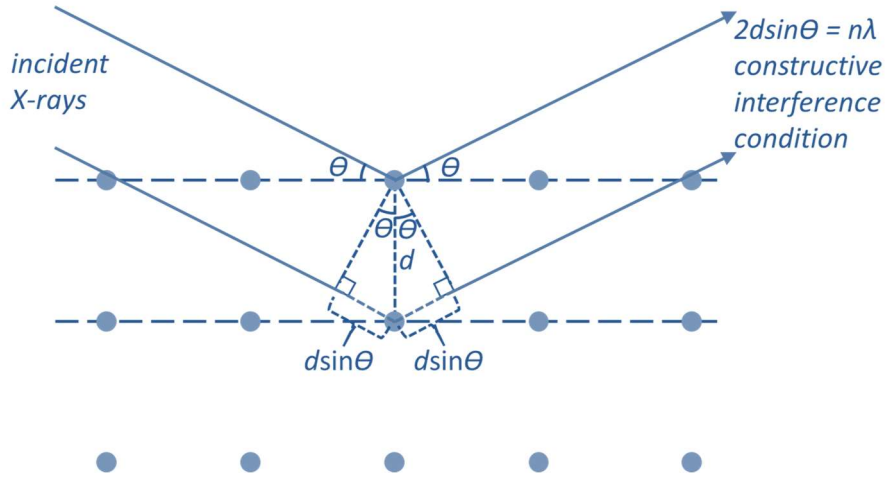


**Figure 20 Illustration of Bragg's Law for X-ray diffraction (XRD)**

In addition, the Scherrer equation describes an empirical relationship between the mean size of crystalline domains ($\tau$) and the full width half maximum line broadening ($\beta$) assuming a grain size no larger than several hundred nanometers:

$$\tau = \frac{K\lambda}{\beta \cos\theta} \tag{27}$$

In this equation, K is the "shape factor" – assigned a value near 1 (commonly 0.9) depending on the shape of the crystalline domains – $\lambda$ is the X-ray wavelength, and $\theta$is the Bragg angle. Particles must be composed of crystalline domains of the same size (when particles are single crystals) or smaller (when particles are multicrystalline). Assuming it is unknown whether the particles are single crystals or multicrystalline, and since line broadening can also be attributed to other breakdowns of long-range crystalline order (but

not necessarily formation of distinct crystalline domains, for instance with dislocations) and to instrumentation, the Scherrer equation is often used to estimate a *lower boundary* on the possible particle size.

The XRD setup used in this thesis was of the standard Bragg – Brentano geometry, illustrated in Figure 21, in which the X-ray source and the detector remain at fixed radii from the sample for all diffraction angles, allowing for better focusing of the X-ray beam on the sample and sharper diffraction peaks. A narrow divergence slit between the X-ray source and the sample and a second narrow receiving slit between the sample and the detector contribute to a well-defined X-ray beam path. In addition, parallel metal planes called Soller slits were placed in the incident and scattered X-ray beam paths to further prevent the X-rays diverging from the intended beam path and still reaching the detector.

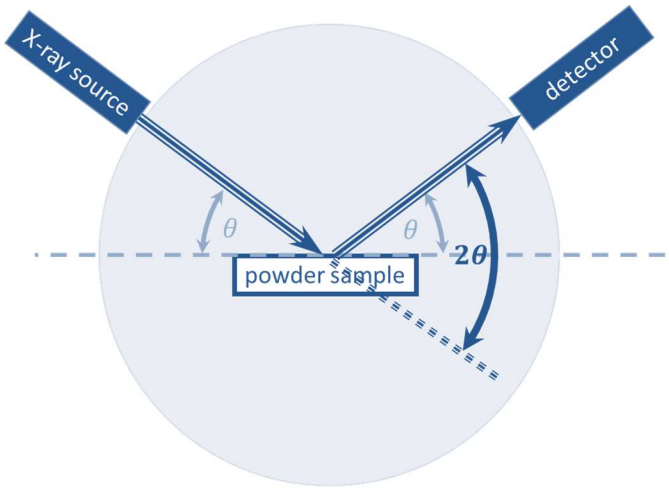


**Figure 21 Bragg-Brentano geometry**

## 2.8 X-ray Photoelectron Spectroscopy (XPS)

X-ray photoelectron spectroscopy (XPS) and time-of-flight secondary ion mass spectroscopy (TOF-SIMS) are two techniques that are used to probe the surface chemistry

rather than the bulk chemistry of a material. By incrementally etching away the surface, each technique can also be used to map the near-surface chemistry as a function of depth from the surface. These techniques are important for battery research and especially post-mortem studies as side reactions between the active material particles and the electrolyte at the particle-electrolyte interface (including the formation of a solid electrolyte interphase via decomposition of electrolyte on the electrode surface) can lead to increased cell polarization, or even complete electrochemical isolation of active material and hence loss of capacity.

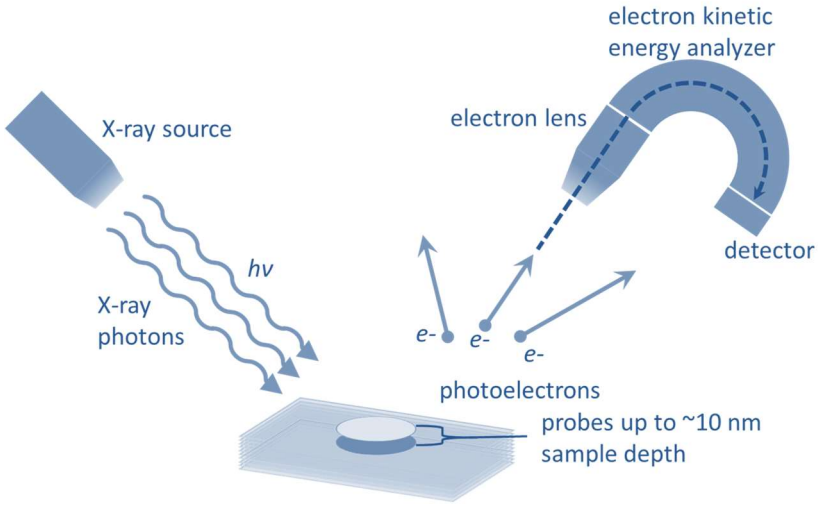


**Figure 22 X-ray photoelectron spectroscopy (XPS) diagram**

In an XPS instrument, X-rays are used to excite electrons from the sample surface and eject them from the material into a vacuum (via the so-called photoelectric effect), as illustrated in Figure 22. A detector measures the precise kinetic energy of these photoelectrons as well as the number of photoelectrons of a specific kinetic energy. Thus,

it can probe the presence of specific chemical bonds and the oxidation states of ions as well as quantitatively describe the elemental composition of the surface.

## 2.9 Time-of-Flight Secondary Ion Mass Spectroscopy (TOF-SIMS)

TOF-SIMS allows for high spacial resolution probing of ~2 nm layers of a surface with ~300 nm scale lateral resolution. As illustrated in Figure 23, TOF-SIMS uses charged ion bombardment of the sample surface to eject ions from the sample surface. The ejected ions are accelerated to the same kinetic energy. Based on the time it takes for the ions to travel a fixed distance to a detector, their velocity and subsequently their mass are calculated.

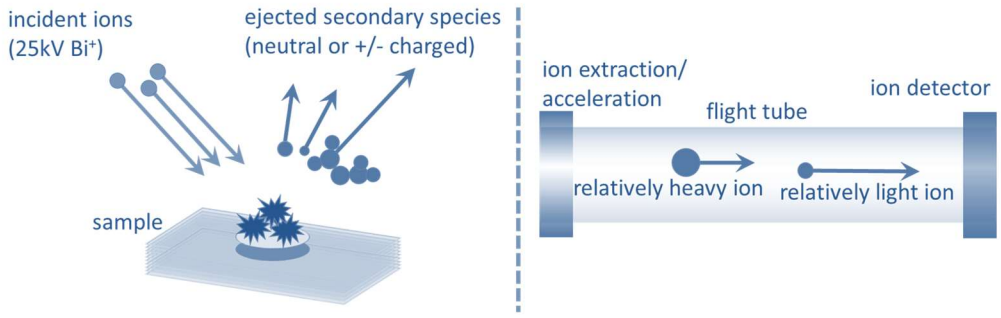


**Figure 23 Tim of flight secondary ion mass spectroscopy (TOF-SIMS) diagram**

## 2.10 Fourier Transform Infrared Spectroscopy (FTIR)

Infrared spectroscopy probes the molecular bonds present in a sample via their excitation by and absorption of particular infrared electromagnetic frequencies. Fourier transform infrared spectroscopy uses a "broadband" light source of multiple electromagnetic frequencies and relies upon a Fourier transform algorithm to deconvolute the absorbances at particular electromagnetic frequencies. Attenuated total reflectance

(ATR) FTIR relies upon the interaction of the totally-internally-reflected infrared beam with a sample in contact with the ATR crystal via an "evanescent" wave that extends beyond the surface of the ATR crystal. This provides a convenient way to probe the infrared bands absorbed by samples that are relatively opaque to infrared waves and without altering the sample in any way for the measurement.

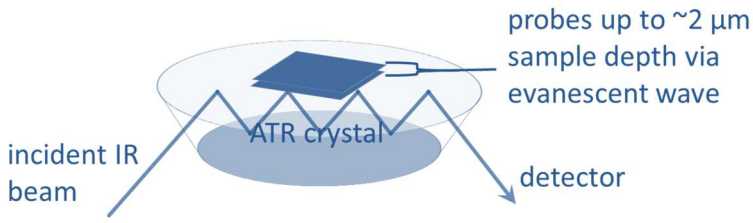


**Figure 24 Attenuated total reflectance fourier transform infrared spectroscopy (ATR FTIR) diagram**

## 2.11 Raman Spectroscopy

Figure 25 illustrates the possibilities for the coupled absorption and re-emission of photons by a material in a Raman spectrometer. Photons absorbed by the sample excite electrons, which subsequently relax to their original energy state along with the emission of a photon (elastic Rayleigh scattering), a lower energy state along with the emission of a higher energy photon (inelastic anti-Stokes Raman scattering), or a higher energy state along with a lower energy photon (inelastic Stokes Raman scattering).[57] In other words, in inelastic Raman scattering, the sample either gains or loses energy with the cumulative transition of an electron to a higher or lower energy level. The Raman spectrum displays the intensity of scattered photons versus their frequency shift from the incident photon

frequency, thus revealing the differences in energy of various electron energy levels for atoms in the sample.

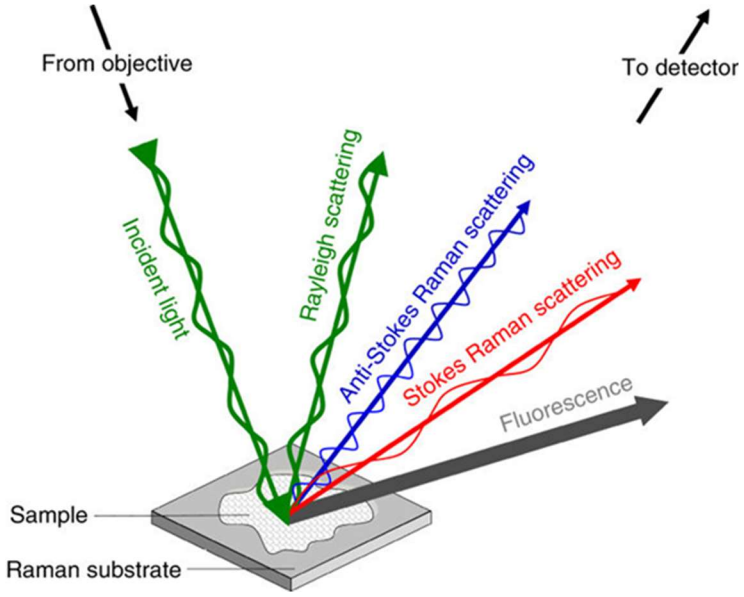


**Figure 25 Diagram of Raman Spectroscopy (Reproduced With Permission From [57])**

# CHAPTER 3. ENHANCING CYCLE STABILITY OF LITHIUM IRON PHOSPHATE IN AQUEOUS ELECTROLYTES BY INCREASING ELECTROLYTE MOLARITY

*Parts are reproduced with permission from Gordon D., Wu M. Y., Ramanujapuram A., Benson J., Lee J. T., Magasinski A., Nitta N., Huang C., Yushin G. (2016). Enhancing Cycle Stability of Lithium Iron Phosphate in Aqueous Electrolytes by Increasing Electrolyte Molarity. Adv. Energy Mater., 6: 1501805. doi: 10.1002/aenm.201501805*

## 3.1 Introduction

Rechargeable aqueous lithium ion batteries (ALIBs) constructed with non-flammable, environmentally-friendly, and low-cost electrolytes such as $Li_2SO_4$ or $LiNO_3$ solutions in water hold promise as a safer, faster and less expensive alternative to organic-electrolyte-based lithium ion batteries for the variety of applications in which current state-of-the-art lithium ion batteries have proven their success. These applications include energy storage for electric vehicles, energy-efficient industrial equipment and the electrical grid with the introduction of intermittent renewable sources of energy. Due to higher conductivity of the aqueous electrolytes, the mass transport limitations of organic electrolytes can be overcome which allows for the use of cells with thicker (and thus cheaper to produce) electrodes while simultaneously achieving faster charging capabilities. Additional cost savings could be realized if the use of dry-rooms and expensive and moisture sensitive organic electrolytes could be avoided. Due to high flammability of conventional LIBs with organic electrolytes and a fear of a thermal runaway, formation of

battery packs in electric vehicles and other applications typically adds ~40-75 % to the weight, volume and cost of the individual cells. Such undesirable expenditures could be greatly reduced in ALIBs because of their greatly enhanced safety characteristics. Although typically restricted to lower cell voltages due to the evolution of oxygen gas on the cathode at higher potentials or hydrogen gas on the anode at lower potentials, several approaches could be utilized to increase the voltage and thus specific energy of ALIBs. For example, Wang et al. have recently demonstrated fully-functioning high voltage ALIBs by preventing a direct contact of aqueous electrolytes with a Li anode surface.[58] Such promises stimulated significant interest in the novel ALIB technology.

Several types of lithium intercalation compounds commonly used in organic electrolytes have already been tested with aqueous electrolytes and found to undergo similar redox reactions. $LiFePO_4$ (LFP), in particular, has attracted attention for ALIB studies due to its good performance in high power commercial cells with organic electrolytes and relatively low potential of LFP, which should prevent oxygen evolution in aqueous electrolytes during cell charging. Interestingly, LFP and other intercalation compounds in aqueous electrolytes were found to suffer from unique mechanisms of degradation. For instance, Luo et al. investigated the impact of dissolved oxygen on the stability of $LiTi_2(PO_4)_3$ in aqueous $Li_2SO_4$ solution.[48] They suggested that in its reduced state $Li_{3-x}Ti_2(PO_4)_3$ can react with dissolved oxygen in the electrolyte leading to capacity loss, especially when charged/discharged at a relatively slower rate of C. [48] After the removal of oxygen from the electrolyte, they demonstrated greatly improved capacity retention for a battery constructed with carbon-coated electrodes using $LiTi_2(PO_4)_3$ and $LiFePO_4$ (LFP) electrodes in 1M $Li_2SO_4$ aqueous solution. He et al. studied the stability of

LFP in 0.5M $Li_2SO_4$ solutions with and without the presence of dissolved oxygen and of varying pH[34] and found that basic solutions and the presence of dissolved oxygen accelerated capacity loss. The authors suggested that LFP undergoes some undesirable side reactions with $OH^-$ and dissolved oxygen. W. Porcher et al. studied the stability of LFP in water without electrochemical charge-discharge. Chemical analysis of supernatant liquids revealed that Li and to a lesser extent $PO_4^{3-}$ dissolved into the solution[59]. They also observed a small amount of Fe in the solution. The fraction of original $Li^+$ and $PO_4^{3-}$ that dissolved depended on the amount of starting $LiFePO_4$ relative to amount of solvent, as well as pH.

In this chapter we report on the significant impact of lithium salt concentration on the cycling stability of a typical commercial LFP powder in aqueous electrolytes. Currently, the most concentrated electrolytes allowed approximately 80% of the maximum discharge capacity to be retained after 500 charge-discharge cycles at a 1.1C rate. After conducting careful post-mortem analysis we propose that undesirable side reactions of aqueous electrolytes with LFP induced electrochemical separation of individual particles within the electrode, leading to the observed capacity fading. Reduction in the concentration of "free" water molecules (not participating in ion hydration shells) that are mostly responsible for the undesirable side reactions between the cathode and electrolyte noticeably improves electrode stability. Therefore, we propose that increasing salt concentration in aqueous solutions offers a new, previously not discussed route for the cycle stability enhancements of LFP and other cathode materials for aqueous metal ion batteries.

## 3.2 Results and Discussion

To investigate the charge-discharge behavior of LFP in aqueous electrolytes, we used a typical commercial powder. The powder X-ray diffraction (XRD) spectrum confirmed the olivine crystal structure of LFP (Figure 26a). Scanning electron microscopy (SEM) showed particles of a round or oblong shape with a maximum particle diameter on the order of 1-2 microns (Figure 26b). Energy dispersive spectroscopy (EDS) confirmed the correct atomic ratios of Fe:P:O of 1:1:4 for $LiFePO_4$ (Figure 26c). The EDS spectrum also revealed the presence of approximately 6 wt.% C. Since this could be linked either to contamination within the SEM chamber or intentional additions to improve electrical conductivity, we also conducted transmission electron microscopy (TEM) (Figure 26d, e) and Raman spectroscopy (Figure 26f) studies to confirm the presence of C. High resolution TEM with EDS showed that C is intermixed with the $LiFePO_4$ particles. In addition, it is present as 1-2 nm disordered layer (Figure 26d and e). The Raman spectra clearly show broad D, G and 2D bands typical for C with sufficient degree of disorder and defects (Figure 26f). EDS did not detect significant amounts of other impurity elements.

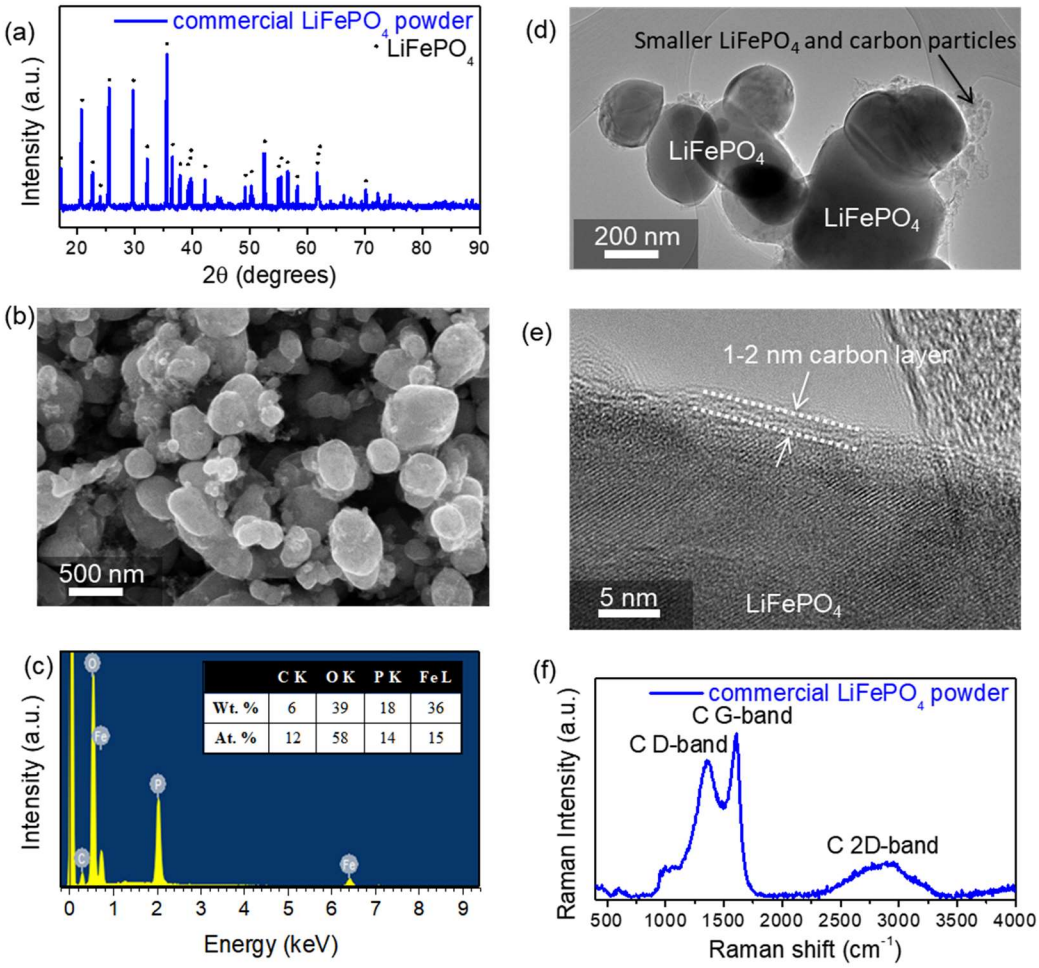


**Figure 26 Characterization of commercial $LiFePO_4$ powder (Gelon LIB Co., China) used in this study: (a) powder X-ray diffraction spectrum, (b) SEM image, (c) EDS spectrum, (d) TEM image of entire particles, (e) TEM image of a particle surface, and (f) Raman spectrum.**

Both working electrodes (WE) and counter electrodes (CE) were prepared with LFP as the active material. The CE was partially delithated and constructed to exhibit larger capacity loading. During electrochemical cycling Li is moved back and forth between the WE and the CE in aqueous electrolyte solutions. Such an experimental design was chosen for several reasons. First, this design minimizes polarizations at the CE relative to polarizations at the WE during constant-current rate capability tests with a two-electrode cell. That is, it avoids the possibility of the CE with a different active material becoming more polarized than the WE and strongly impacting observed rate capability. Second, it avoids the complication of determining whether better or worse cell stability result from lesser or greater degradation of the CE, WE or both, in order to assess the impact on the cycling stability of LFP. Third, this experimental design avoids the use of a reference electrode (RE) that could drift in potential over time.

Constant-current charge-discharge (C-D) tests were conducted to evaluate the cycling stability as well as the rate performance of the LFP in aqueous solutions of different compositions (Figure 27). The electrochemical cells were charged and discharged at a 1.1C rate for the first 10 cycles, then charged and discharged for three cycles at each rate of 2.1C, 3.2C, 5.3C and 8.5C, and subsequently charged and discharged at a 1.1C rate for 500 total charge-discharge cycles. Potential limits were chosen to be +/- 0.4V for the WE versus the CE, suitable since the reversible redox reaction occurring at the WE and CE was the same.

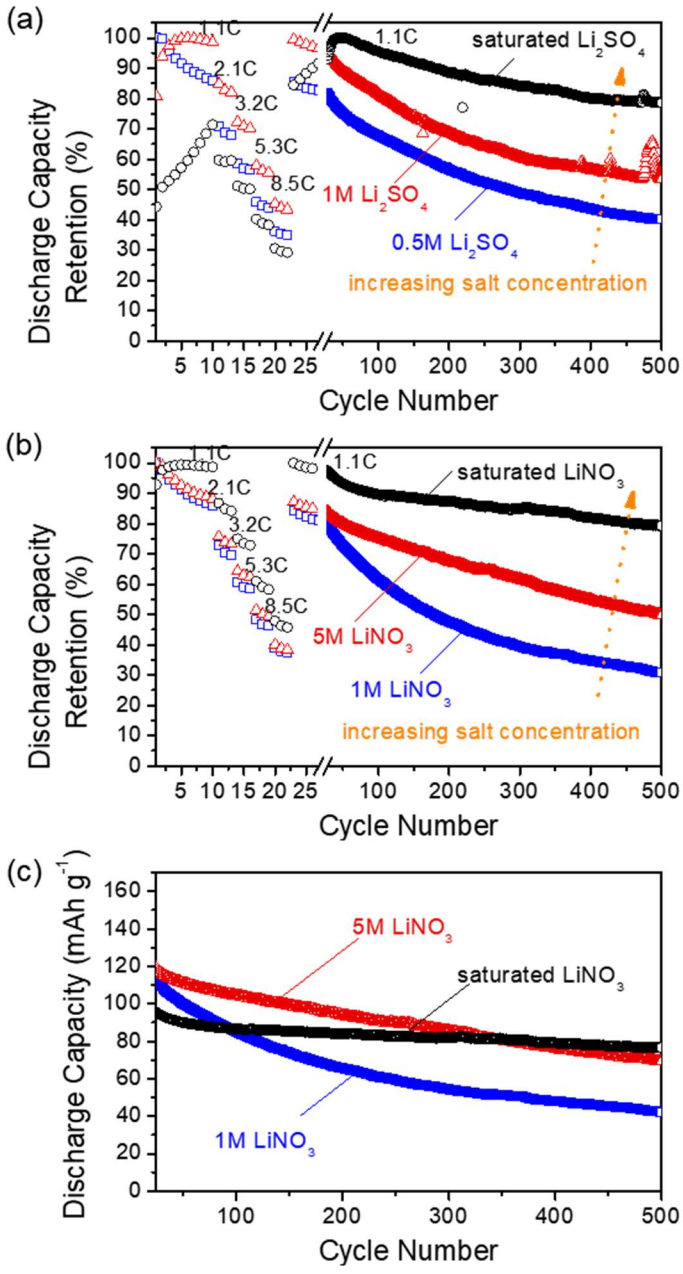


**Figure 27 (a) Discharge capacity retention for electrochemical cells constructed with LiFePO4 working electrodes, $LiFePO_4$ counter electrodes and aqueous solutions of varying $Li_2SO_4$ salt concentration. (b) Discharge capacity retention and (c) gravimetric discharge capacity for electrochemical cells constructed with $LiFePO_4$ working electrodes, $LiFePO_4$ counter electrodes and aqueous solutions of varying $LiNO_3$ concentration. For all cells, counter electrodes had 4-6 times greater mass than working electrodes and were delithiated to $Li_{0.47}FePO_4$ by running a constant current between the counter electrode and a stainless steel electrode prior to conducting the charge-discharge experiment.**

Increasing the concentration of either $LiNO_3$ or $Li_2SO_4$ salt did not have a dramatic impact on the rate performance of LFP, but substantially improved its discharge capacity retention (Figure 27a and b). Similar rate performance, despite differences in ionic conductivity of electrolytes, suggest that lithium insertion/extraction is limited by the rate of surface reactions or solid-state diffusion through the individual particles. The cells in saturated $Li_2SO_4$ electrolyte exhibited some sort of "activation" behavior, where the capacity was improving during the initial ~ 50 cycles. We hypothesize that in spite of the application of vacuum, LFP electrodes might not be initially wetted completely by this electrolyte due to its higher viscosity. Figure 27c shows an example of the changes in absolute capacity values of LFP WE during cycling in $LiNO_3$–electrolyte of different concentration. The initial capacity value variation might be slightly impacted by the mass measurements errors since the thickness and the areal density of the stainless steel current collector was not very uniform. However, we clearly see that reducing the relative $H_2O$ solvent content (increasing the salt concentration) in electrolyte significantly improved LFP cycle stability. Interestingly, we also observed similar trends of increasing stabilities of other cathodes (such as lithium cobalt oxide and lithium nickel manganese cobalt oxide) with increasing aqueous electrolyte molarity. While these studies will be reported separately, we hypothesize that the positive impact of high salt concentration on the stability of ALIBs might be sufficiently broad.

Voltage profiles for the constant-current C-D tests show relatively flat plateaus after several charge-discharge cycles, with cell polarizations on the order of 25-50mV (Figure 28). Such polarization values were comparable or even slightly smaller than what was observed for identical LFP electrodes opposite lithium metal in a typical organic electrolyte

(Figure 28h; also compare Figure 28a-f with Figure 28g). The larger polarization observed for an organic electrolyte "half-cell" may be explained by a higher overpotential for the oxidation/plating of lithium metal – which in turn is related to the formation of solid electrolyte interphase (SEI) on the Li metal surface – and by a higher ionic resistance of the organic electrolyte.

Using a calculated value for the Li insertion/extraction potential for LFP of 3.47V vs. Li/Li+ obtained using a Generalized Gradient Approximation +U method,[60] we selected the potential limits of 3.07V and 3.87V (+/- 0.4V about 3.47V) for electrochemical tests in an organic electrolyte. For comparison, we also conducted tests in a broader window of 2.87V and 4.07V (+/- 0.6V about 3.47V). Organic electrochemical half-cells were charged and discharged with the same routine as the aqueous electrochemical cells, and also at a slower rate of 0.18C. Under all conditions, the discharge capacity was retained over 100-500 cycles (Figure 29) and the rate performance was somewhat similar to that in aqueous cells (Figure 29b). Since aqueous electrolyte exhibits dramatically higher conductivity[27], we conclude that electrolyte conductivity was likely not the limiting factor in all of our electrochemical tests. The cell stability in organic electrolyte was clearly better in aqueous cells (Figure 29a). This suggests a unique mechanism of degradation for LFP cycling in aqueous solutions.

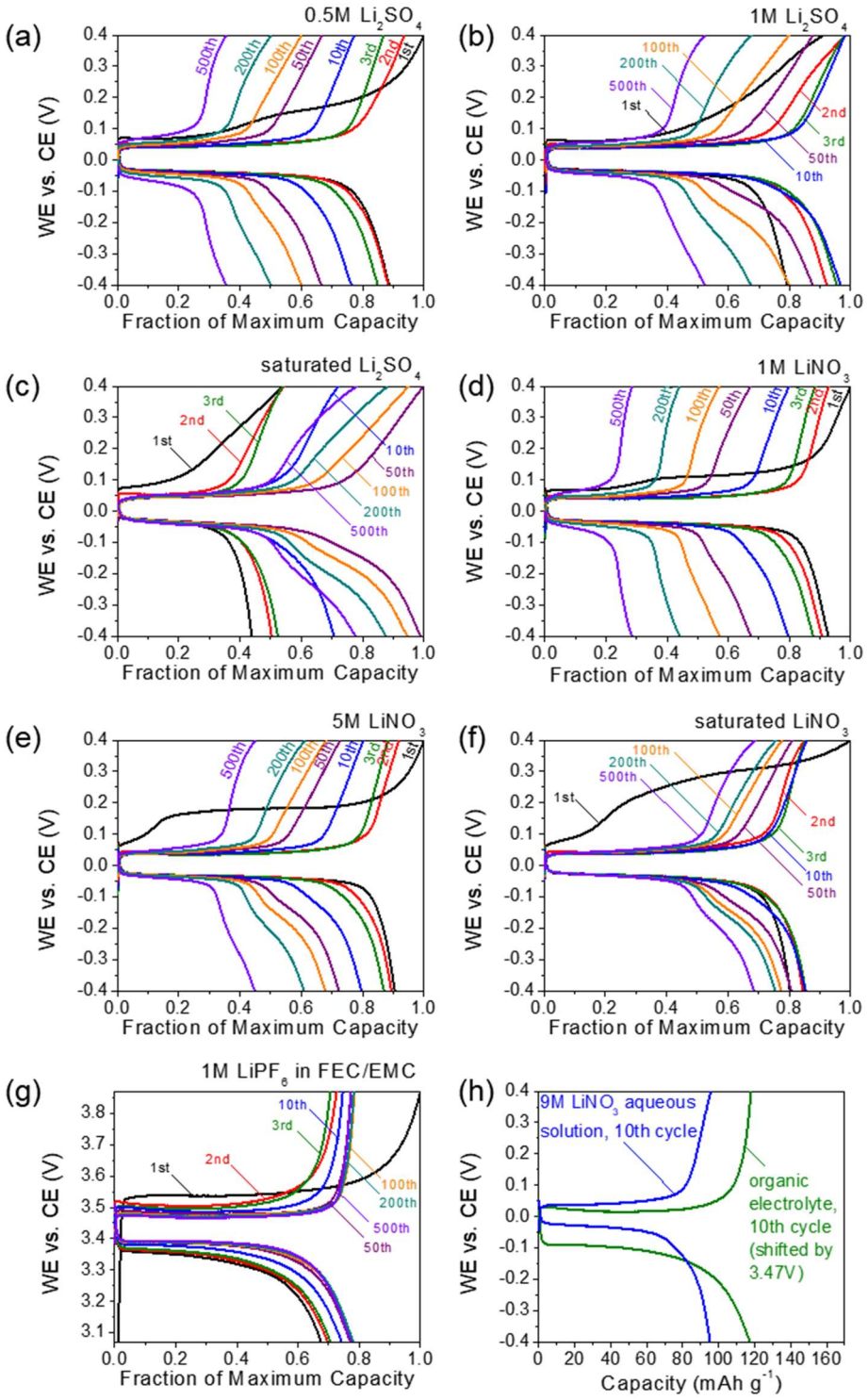


**Figure 28 Voltage profiles for constant-current charge-discharge at 1.1C rate of $LiFePO_4$ working electrodes opposite $LiFePO_4$ counter electrodes in (a-c) aqueous $Li_2SO_4$ solutions of varying molarity and (d-f) aqueous $LiNO_3$ solutions of varying molarity. (g) Voltage profile for constant-current charge-discharge at 1.1C rate of**

**$LiFePO_4$ working electrode opposite Li foil in 1M $LiPF_6$ in FEC/EMC (30:70 by vol.) organic electrolyte. (h) Comparison of voltage profiles for 10$^{th}$ cycle for saturated $LiNO_3$ aqueous electrolyte cell and organic electrolyte cell.**

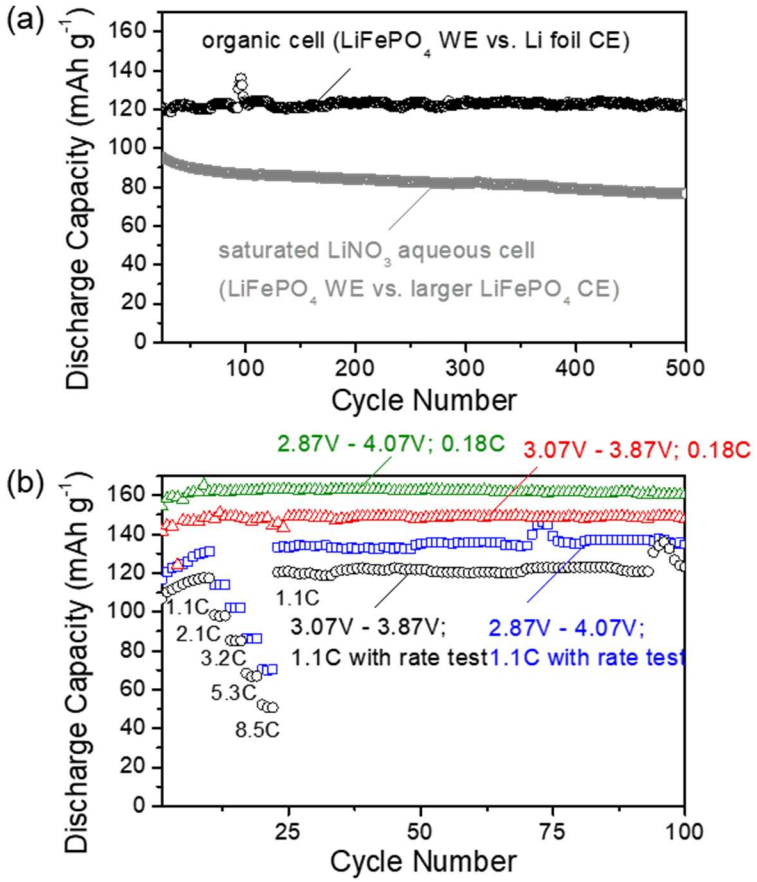


**Figure 29 (a) Comparison of discharge capacity with aqueous and organic electrolytes for electrochemical cells constructed with $LiFePO_4$ working electrodes, and charged and discharged at a 1.1C rate with a 0.8V-wide potential window. (b) Gravimetric discharge capacities for electrochemical cells charged and discharged at various rates with various potential windows. Electrochemical cells with aqueous electrolytes were prepared as described previously. Electrochemical cells with organic electrolyte were assembled with $LiFePO_4$ working electrodes opposite Li foil counter electrodes and 1.0M $LiPF_6$ in FEC/EMC (30:70 by volume) electrolyte.**

To elucidate the unique changes that occur with the electrochemical cycling of LFP in aqueous electrolytes, and investigate the possible reasons for the beneficial impact of higher salt concentration on capacity retention, we conducted electrochemical characterization using electrochemical impedance spectroscopy (EIS) as well as post-mortem characterizations of the electrodes.

EIS was conducted after the 1$^{st}$ and the 300$^{th}$ or 500$^{th}$ charge-discharge cycles. Figure 30 shows Nyquist impedance plots for 0.5M, 1M and saturated $Li_2SO_4$ aqueous electrolyte (similar results were also obtained with 5M and saturated $LiNO_3$ aqueous electrolytes). The equivalent series resistance (ESR) can be determined by the intersection of the Nyquist plot with the horizontal axis. The contributions to ESR include electrical resistance of the electrodes (which should be the same for all the samples), the electrical resistance of the current collector-electrode interface (which should also be the same for all the samples) and electrolyte resistance. The cell with 1M electrolyte solution exhibits the lowest ESR, which is likely related to the highest conductivity of this electrolyte. The use of saturated electrolyte results in the highest ESR. While this electrolyte exhibits the highest charge carrier ($Li^+$) concentration, the mobility of ions in this electrolyte is impeded by the insufficient concentration of solvent molecules. A distinct change in the Nyquist plot is observed after 300 charge-discharge cycles, namely – impedance arcs emerge with diameters on the order of 1000-2000 $\Omega$ cm$^2$. This indicates formation of the resistor-capacitor (R-C) loop (resistor in parallel with a capacitor) in the equivalent circuit, commonly associated with the formation of an ionically conductive surface layer (aka SEI). The data were fit with an equivalent circuit model to help elucidate changes to the resistances within the cells, shown in Figure 30c. In the equivalent circuit model, $R_{ESR}$

represents the equivalent series resistance, $R_{SEI}$ represents the ionic resistance of a surface layer at each electrode, $R_{CT}$ represents the total charge-transfer resistance in the cell, L represents an inductance originating from the measuring instrument and CPE represents a constant phase element (a form of capacitive circuit element). The larger $R_{SEI}$ value for each fit, $R_{SEI\ 1}$, is likely associated with an SEI surface layer at the working electrode. The large initial value for $R_{SEI\ 1}$ suggests that an SEI layer forms within the first charge-discharge cycle. $R_{SEI\ 1}$ decreases from the 1$^{st}$ to the 300$^{th}$ cycle in all three concentrations of electrolyte. The decrease in these resistance values may result from the increase in surface area of the LFP in contact with the electrolyte due to the fracture of the LFP during electrochemical cycling (to be discussed later). The lower values of $R_{SEI\ 1}$ for the electrode cycled in saturated electrolyte suggest a significantly less resistive (e.g., thinner) SEI / surface layer that forms in this high molarity electrolyte.

Comparison of SEM micrographs of the surface of a pristine electrode with the electrodes after 500 charge-discharge cycles is each aqueous electrolyte (0.5M, 1M and saturated $Li_2SO_4$ solution or 1M, 5M and saturated $LiNO_3$ solution) or organic electrolyte revealed formation of cracks induced by electrochemical cycling (Figure 31). Such cracks, in principle, may induce electrical separation of the portion of the active material from the electrode and induce capacity fading. Interestingly, however, we did not observe an obvious correlation between the crack density and the capacity fading. In fact, the LFP cycled in organic electrolyte with literally no capacity fading within 500 cycles (Figure 29) showed density of cracks comparable (possibly only slightly smaller) than what we observed in all aqueous cells.

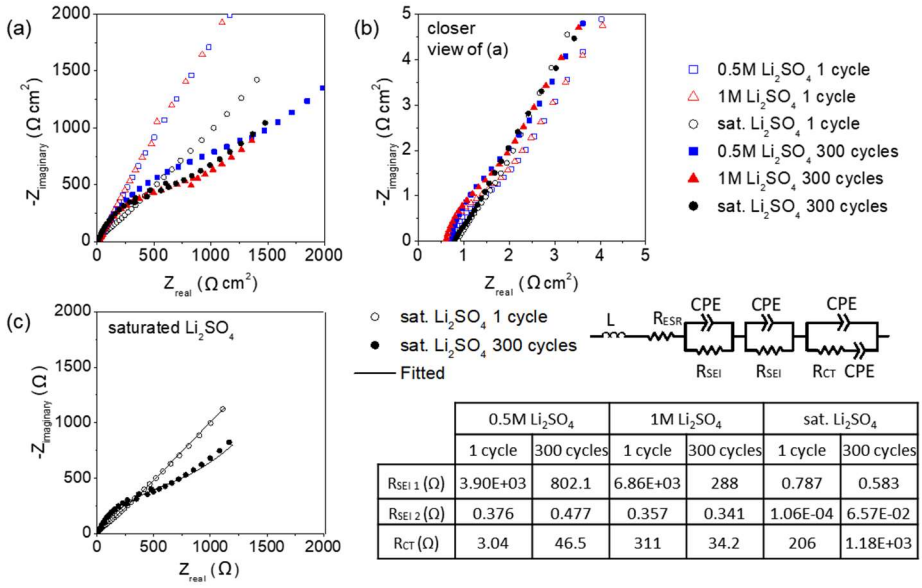


| | 0.5M $Li_2SO_4$ | | 1M $Li_2SO_4$ | | sat. $Li_2SO_4$ | |
|---|---|---|---|---|---|---|
| | 1 cycle | 300 cycles | 1 cycle | 300 cycles | 1 cycle | 300 cycles |
| $R_{SEI\,1}$ (Ω) | 3.90E+03 | 802.1 | 6.86E+03 | 288 | 0.787 | 0.583 |
| $R_{SEI\,2}$ (Ω) | 0.376 | 0.477 | 0.357 | 0.341 | 1.06E-04 | 6.57E-02 |
| $R_{CT}$ (Ω) | 3.04 | 46.5 | 311 | 34.2 | 206 | 1.18E+03 |

**Figure 30 (a, b) Electrochemical impedance spectroscopy (EIS) Nyquist plots for electrochemical cells constructed with $LiFePO_4$ working electrodes, $LiFePO_4$ counter electrodes and aqueous solutions of varying $Li_2SO_4$ salt concentration, and (c) equivalent circuit model, resistance values from fitting of the model to the experimental data, and example plot of the model fit to the experimental data. $R_{ESR}$ represents the equivalent series resistance, $R_{SEI}$ represents the ionic resistance of a surface layer at each electrode, $R_{CT}$ represents the total charge-transfer resistance in the cell, L represents an inductance likely originating from the measuring instrument and CPE represents a constant phase element (a form of capacitive circuit element). For all electrochemical cells, counter electrodes had 4-6 times greater mass than working electrodes and were delithiated to $Li_{0.47}FePO_4$ by running a constant current between the counter electrode and a stainless steel electrode prior to conducting constant current charge-discharge. Electrochemical cells were charged/discharged at a 1.1 C rate except for a rate capability test consisting of three cycles each at each rate of 2.1C, 3.2 C, 5.3C, and 8.5 C (as shown in Fig. 2a). EIS was conducted after the first full charge-discharge cycle, consisting of lithium extraction from the working electrode followed by lithium reinsertion into the working electrode. EIS was conducted again after 300 charge-discharge cycles, again with the working electrode in the reduced state.**

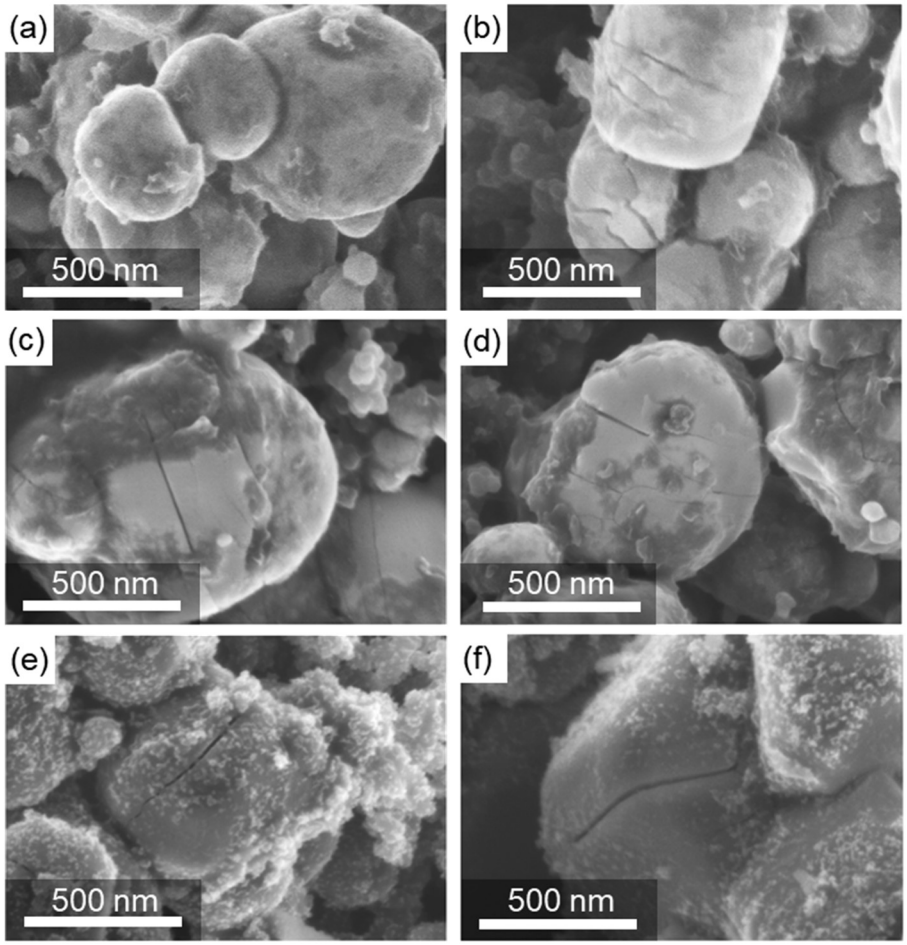


**Figure 31 Scanning electron micrographs of $LiFePO_4$ electrodes: (a) fresh/uncycled electrode (b) electrode after 500 charge-discharge cycles in aqueous 0.5M $Li_2SO_4$ solution (c) electrode after 500 charge-discharge cycles in aqueous 1M $LiNO_3$ solution (d) electrode after 500 charge-discharge cycles in aqueous saturated $LiNO_3$ solution, (e) and (f) electrode after 500 charge-discharge cycles in 1M $LiPF_6$ FEC/EMC (30:70 by vol.) organic electrolyte.**

Transmission electron microscopy (TEM) analyses (Figure 32) demonstrated that cracks propagate deeply into or traverse entire LFP particles. In spite of the great commercial success and adoption of LFP materials by industry, the mechanisms by which $Li_xFePO_4$ transforms between the lithiated and delithiated phases are still debated in literature and the dominant mechanism may vary significantly with variables, such as particle size and charging/discharging current. Cogswell and Bazant describe the impact of coherency strain, proportional to particle volume, on the nucleation barrier for lithiation/delithiation of LFP particles of various geometries.[61] They suggest that particle surfaces are likely to be "wetted" with a single phase, and that particles may transform through a movement of a coherent interface along the (101) plane. Lithiation and delithiation of LFP has been also recently studied via *in situ* TEM. Zhu et al. identified stress-free regions of $FePO_4$ and $LiFePO_4$ separated by a distinct phase boundary, containing periodic dislocations during the electrochemical lithiation of microsized $LiFePO_4$ particles.[62] Niu et al. observed the electrochemical delithiation of LFP nanowires with 200-400 nm diameter. In contrast to several previous studies, they observed the formation of a solid solution zone beginning at the particle surface during delithiation, without the presence of dislocations. [63] Kao et al. constructed a phase transition map indicating combinations of particle diameter and overpotential for which they predict crystalline LFP to transform into either crystalline or amorphous $FePO_4$.[64] Ceder et al. discussed the lithiation and delithiation of LFP as a single phase solid solution at low overpotentials.[65] However, the exact pathways for LFP transformations during Li insertion and extraction in aqueous electrolytes may, in principle, be different. Indeed, the rate of lithium transport through the particles' surface (and thus local current distributions

at the particle/electrolyte interfaces) might be impacted by electrolyte-dependent effects. Formation of new phases originating at the surface may also be electrolyte-dependent. But since we observe fracture of LFP in all electrolytes (Figure 31 and Figure 32) this process appear to be universal (at least for our LFP particles) and likely originating from stresses and strains associated with the approximately 7% difference in volume and lattice mismatch between the lithiated and unlithiated phases, as previously observed in organic electrolytes and following chemical delithiation.[66-68] More specifically, we hypothesize that the particles' cracking occurs due to a fatigue induced by the two-phase lithiation and delithation.

Interestingly, higher resolution TEM studies of particles electrochemically cycled in the lowest concentration 0.5M $Li_2SO_4$ or 1M $LiNO_3$ aqueous electrolytes show that particle surfaces are covered by an amorphous phase. For LFP electrochemically cycled in 1M $LiNO_3$ solution, the amorphous surface layer has approximately 3-6 nm varying thickness. For LFP cycled in 0.5M $Li_2SO_4$ solution, an amorphous phase layer covering the crystalline LFP was also observed, but the overall thickness was slightly smaller - 2-3 nm. Overall, the thickness of the amorphous phase was the largest for the condition in which discharge capacity retention was the worst (1M $LiNO_3$). Such a thick amorphous layer was not visible for the saturated salt conditions: we observe that for LFP electrochemically cycled in saturated solutions, a crystalline phase extends to ~1 nm (for saturated $LiNO_3$) and 1-2 nm (for saturated $Li_2SO_4$ solution) of the particle surface.

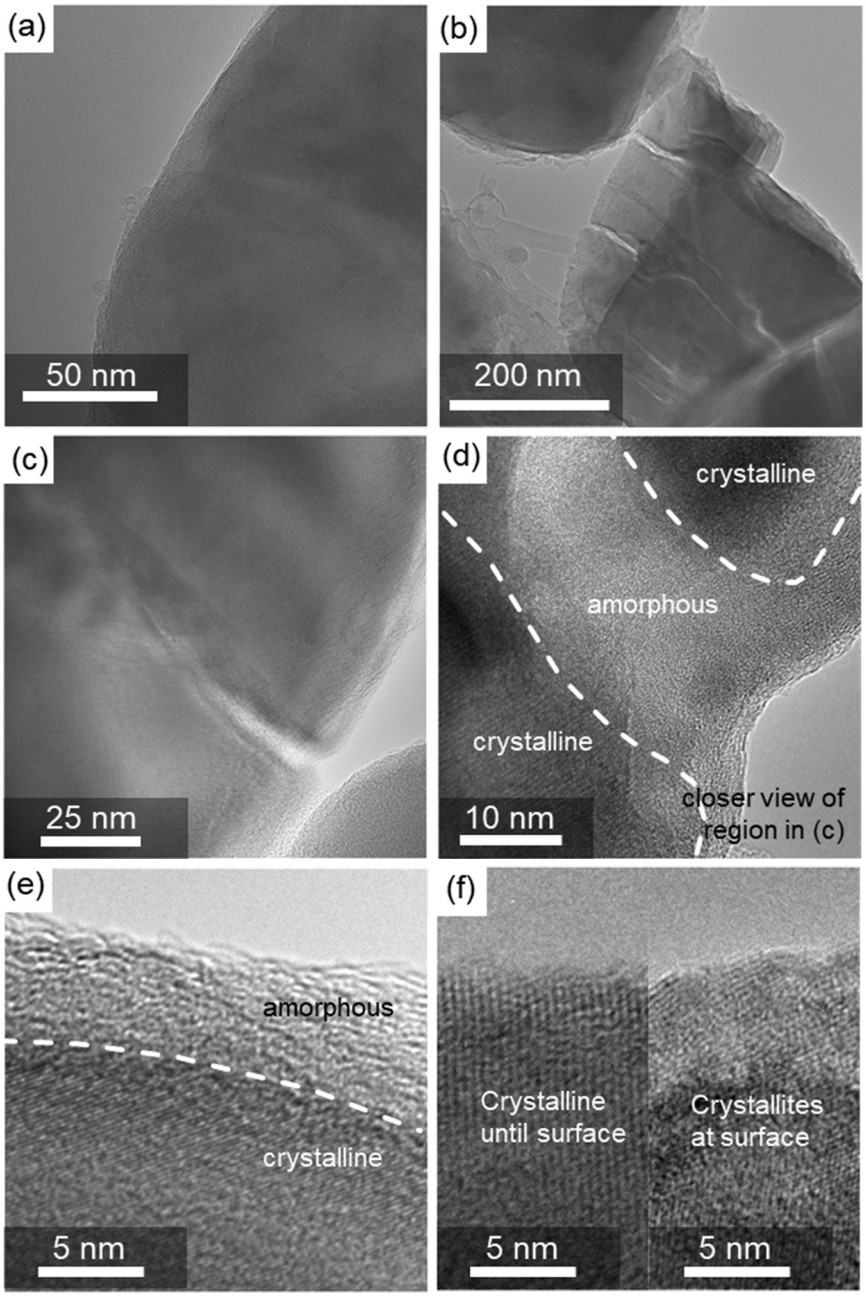


**Figure 32 Transmission electron micrographs of $LiFePO_4$ particles: (a) fresh/uncycled particle (b) particle after 500 charge-discharge cycles in aqueous 0.5M $Li_2SO_4$ aqueous solution (c)-(e) particles after 500 charge-discharge cycles in aqueous 1M $LiNO_3$ solution and (f) particle after 500 charge-discharge cycles in 1.0M $LiPF_6$ in FEC/EMC (30:70 by vol.) organic electrolyte.**

Complete surface coverage by the amorphous layer on the LFP electrochemically cycled in low-concentration aqueous electrolytes was observed in all studies. The fact that amorphous layer extends into the cracks that form during cycling (as shown Figure 32d, for example) indicates that this layer is a newly produced coating formed during cycling in aqueous electrolytes. In contrast, for a particle electrochemically cycled in an organic electrolyte, depending on specific region observed, a crystalline phase crystal appears to extend to within 1nm of the particle surface (or all the way to the particle surface with no amorphous layer visible).

To attempt to identify the chemical composition of the amorphous surface layer, we conducted energy dispersive spectroscopy (EDS), time of flight secondary ion mass spectroscopy (SIMS), and X-ray photoelectron spectroscopy (XPS) with depth profile. In addition, we conducted Attenuated Total Reflectance Fourier Transform Infrared Spectroscopy (ATR FTIR) and X-ray diffraction (XRD) studies to observe any structural/chemical changes to the bulk material. We note that the penetration depth for ATR FTIR is typically 0.5-2 microns, near the diameter of our particles, and X-rays probes deeply into most materials. Figure 33 and Figure 34 show the XRD and FTIR spectra, respectively, for a pristine electrode, an electrode after 500 charge-discharge cycles in aqueous electrolyte, and an electrode after 500 charge-discharge cycles in organic electrolyte. XRD and FTIR studies each confirmed the presence of $LiFePO_4$ initially and after cycling electrodes in either aqueous or organic electrolyte, without revealing additional phases formed during cycling. The FTIR spectra of both initial and cycled LFP are very similar to that obtained by A. Ait Salah et al. for LFP.[69]

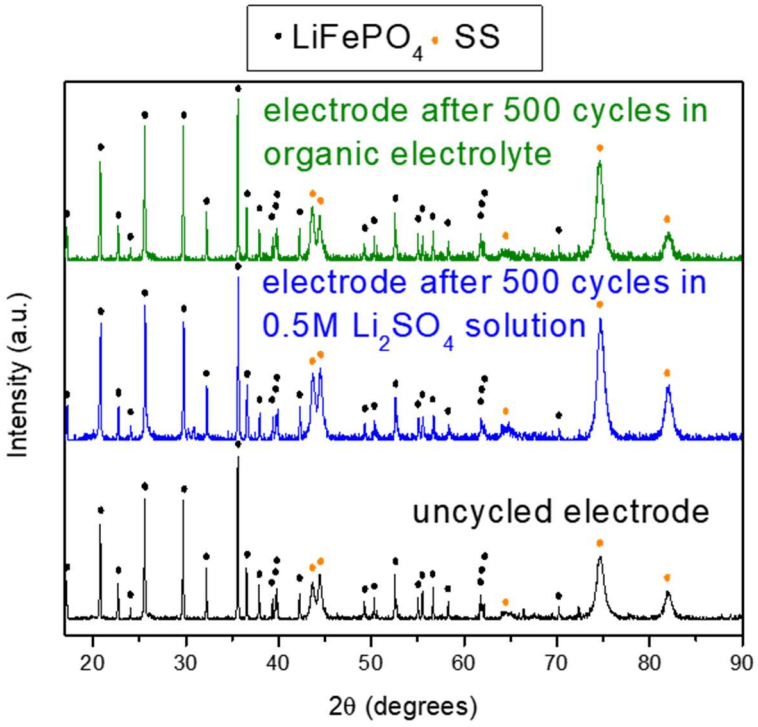


**Figure 33 X-ray diffraction spectra for fresh/uncycled $LiFePO_4$ electrode, $LiFePO_4$ working electrode after 500 charge-discharge cycles in aqueous 0.5M $Li_2SO_4$ solution, and $LiFePO_4$ working electrode after 500 charge-discharge cycles in 1M $LiPF_6$ FEC/EMC (30:70 by vol.) organic electrolyte.**

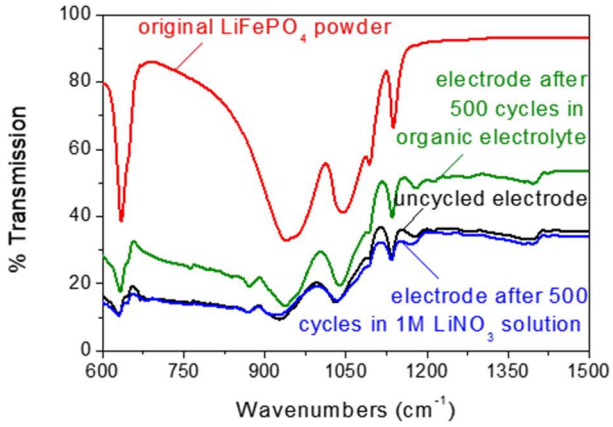


**Figure 34 FTIR spectra for commercial $LiFePO_4$ powder, fresh/uncycled $LiFePO_4$ electrode, $LiFePO_4$ working electrode after 500 charge-discharge cycles in aqueous 1M $LiNO_3$ solution, and $LiFePO_4$ working electrode after 500 charge-discharge cycles in 1M $LiPF_6$ FEC/EMC (30:70 by vol.) organic electrolyte.**

SIMS is more effective in probing compositional changes to the outermost layers of a material and variations with depth from the surface, due to the sub nanometer depth resolution and micron scale lateral resolution. SIMS conducted on a fresh/uncycled electrode and electrodes after 500 charge-discharge cycles in 0.5M $Li_2SO_4$ or 1M $LiNO_3$ aqueous electrolyte revealed a reduction in the ratio of Fe near the surface relative to Fe deeper below the surface after electrochemical cycling. In contrast, SIMS conducted on electrodes after 500 C-D cycles in saturated $Li_2SO_4$ or saturated $LiNO_3$ aqueous electrolyte (samples for which discharge capacity diminished much less) revealed a more similar ratio of Fe near the surface relative to Fe deeper below the surface before and after electrochemical cycling. These trends are evident in Figure 35. For these plots, individual SIMS depth profiles were normalized by the intensity occurring at maximum sputter depth, which was also the depth at which the maximum intensity signal was observed. This accounts for the slight variability of $LiFePO_4$ present in the analysis area for each sample. SIMS provides some hints as to the composition of the surface layer observed in TEM. Since outermost surface of the most degraded samples may be Fe-deficient, the surface may consist of $Li_3PO_4$, as Porter et al. suggest forms on the surface of LFP exposed to water even without electrochemical cycling. The layer thickness may be too small to detect a change for less degraded samples cycled in saturated $Li_2SO_4$ of $LiNO_3$ solutions.

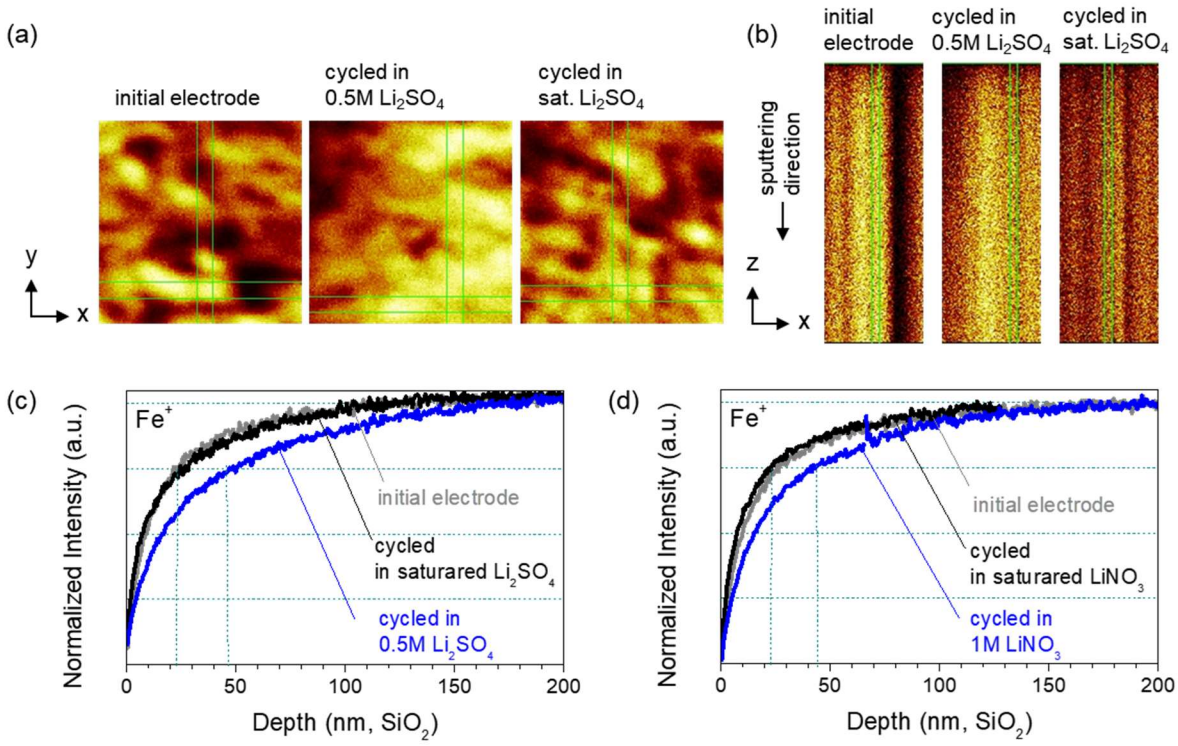


**Figure 35 SIMS data for Fe+ secondary ion species: (a) density of counts in the XY plane (150 micron by 150 micron dimensions) summed over 216 nm $SiO_2$ sputter depth, (b) density of counts in the XZ plane (150 micron by 216 nm $SiO_2$ sputter depth dimensions) for the slice indicated in the XY plane, (c) intensity as a function of sputter depth, normalized by the maximum intensity occurring at the maximum sputter depth, for the fresh electrode and electrodes after 500 charge-discharge cycles in 0.5M or saturated $Li_2SO_4$ aqueous electrolytes, and (d) intensity as a function of sputter depth, normalized by the maximum intensity occurring at the maximum sputter depth, for the fresh electrode and electrodes after 500 charge-discharge cycles in 1M or saturated $LiNO_3$ aqueous electrolytes.**

Unfortunately, EDS was not precise enough to detect compositional changes at the electrode surfaces to provide further information about the composition of the particle surface. Attempts to perform EDS during TEM were challenging since the LFP particles were not stable for prolonged periods under the electron beam. While XPS can reveal the presence of each of the elements of LFP (Li, Fe, P and O) at the electrode surface, the intensity of the Fe3s spectral lines was too low to measure changes in the amount of Fe

present at the surface relative to the amount of P or other elements (Figure 36). In addition, Fe2p spectral lines overlap with F Auger lines (F is present in the PVDF binder), and Fe3p spectral lines overlap with Li1s spectral lines, hence these spectral lines for Fe also cannot be used to measure changes in the amount of Fe.

Below we discuss how the loss of discharge capacity in aqueous solutions of various salt concentrations (Figure 27) may correlate with the observation of amorphous surface layer formation (Figure 32) and changes in impedance (Figure 30).

First, the dissolution of the LFP at the particles' surface likely leads directly to a loss of active material via electrical separation of active particles. Indeed, if the original C surface layer is permeable to water (e.g., through defects), water may attack $LiFePO_4$ underneath the C (as earlier suggested by W. Porcher et al.[59] - by leaching out Fe, followed by the dissolution of Li and $PO_4^{3-}$ into a solution), causing separation of C from the surface of an individual LFP particle and thus electrically disconnecting it from the rest of the electrode. The rate of such dissolution reaction should be reduced when higher salt concentration is present in aqueous electrolytes: due to the common ion effect the presence of higher concentrations of $Li^+$ in the electrolyte will reduce the solubility of $LiFePO_4$ and/or the product of a side reaction such as $Li_3PO_4$ on the surface (which would otherwise stabilize $LiFePO_4$ from dissolution), similar to the impact of high salt concentration on the reduced dissolution of polysulfides in organic electrolytes of Li-S batteries.[70] In other words, because the effective concentration of water molecules available for these dissolution reactions are reduced in concentrated electrolytes, the electrode degradation should also be diminished, as was observed (Figure 27). Our SIMS studies confirmed this conclusion, by revealing significantly more pronounced leaching of Fe from the surface of

electrodes cycled in low molarity aqueous electrolytes (Figure 35). The slightly better discharge capacity retention for LFP cycled in 0.5M $Li_2SO_4$ solution as opposed to LFP cycled in 1M $LiNO_3$ solution, despite equal concentrations of $Li^+$ in the two solutions, might be related to the surface layer chemistry or thickness growth kinetics.

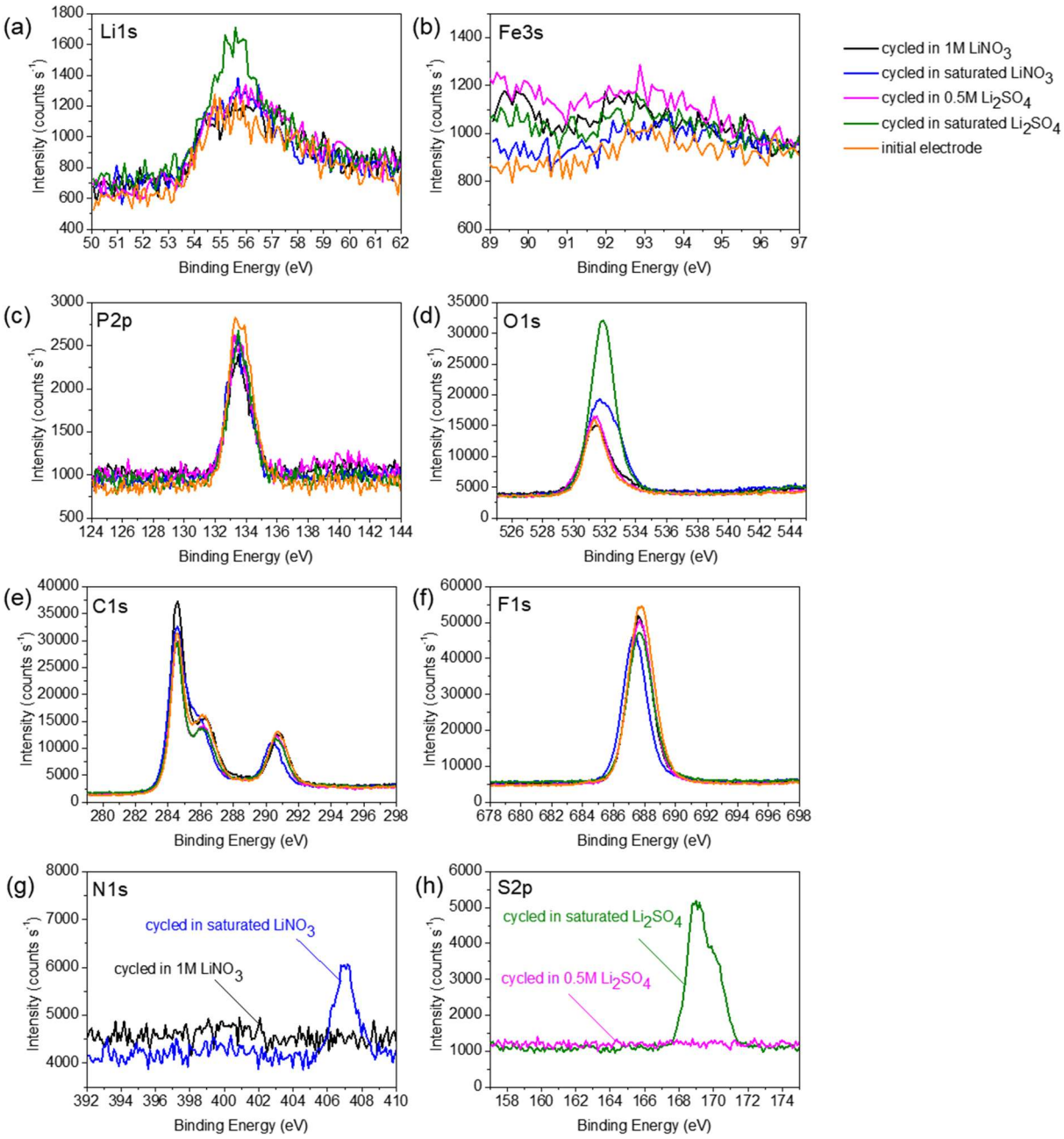


**Figure 36 Surface XPS spectra for initial electrode (orange) and electrodes after 500 charge-discharge cycles in aqueous electrolytes with the following salts and concentrations: 0.5M $Li_2SO_4$ (pink), saturated $Li_2SO_4$ (green), 1M $LiNO_3$ (black) and saturated $LiNO_3$ (blue). High-resolution plots are provided for expected energies for (a) Li1s, (b) Fe3s, (c) P2p, (d) O1s, (e) C1s, (f) F1s, (g) N1s and (h) S2p peaks. (Spectra for all five electrode samples are shown in figures (a)-(f), while spectra for only two electrode samples are shown in figures (g) and (h) for easier comparison.)**

We shall also note that high concentration of lithium salt raises the absolute value of the Li insertion potential of LFP (Figure 37). These changes may also slightly impact the surface layer microstructure and dissolution, although, in the opinion of the authors, to a very limited extent.

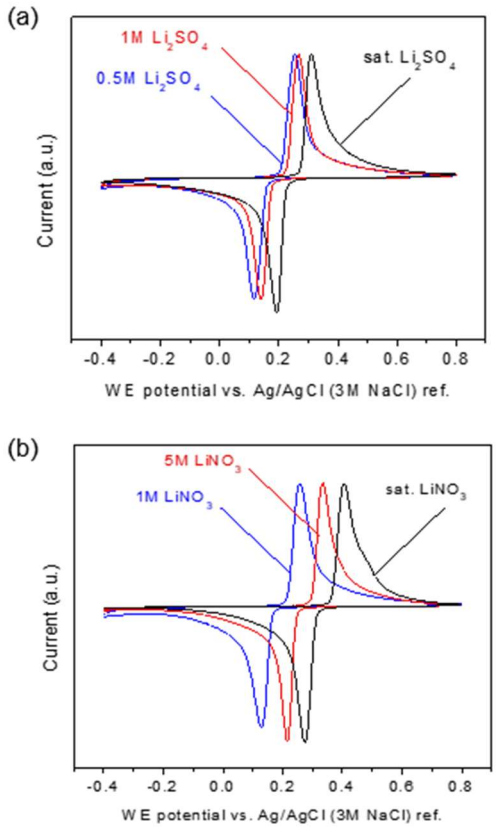


**Figure 37 Cyclic voltammograms of LFP electrodes in (a) aqueous $Li_2SO_4$ solutions of varying molarity and (b) aqueous $LiNO_3$ solutions of varying molarity. The plot shows the second full cycle at a 0.3 mV·s-1 scan rate, with currents normalized by the oxidation peak current since electrodes had slightly different mass loadings.**

Second, the Fe-deficient amorphous layer forming on the particles' surface (Figure 32) should also be electrically insulating and thus should similarly contribute to electrical separation of individual particles when its thickness exceed some critical value (e.g. related

to quantum mechanical tunneling distance for electrons). As a counter-argument one may suggest that that such a resistive surface layer growth would induce some gradual increase in electrode resistance and reveal itself as a polarization increase (increase in the charge-discharge hysteresis), which we did not observe except for the last hundreds of cycles (Figure 28). However, since LFP itself does not contribute much to electrode electrical conductivity (carbon does the job of carrying the electrical current), this scenario could still be plausible assuming that the dependence of the electrical connectivity of the individual particles on the thickness of such a surface layer is very abrupt (almost binary).

Third, the amorphous layer may, in principle, form a barrier for Li ion diffusion. We believe that loss of capacity directly from the prevention of ionic transport is unlikely to be a primary contributor to cell degradation since an ionically insulative layer would likely result in the continuous growth of the overpotential for lithium insertion and extraction, which does not take place (Figure 28). Furthermore, when we increased the cell temperature to 60 °C (which should have increased ionic conductivity due to strong dependence of the Li diffusivity on temperature) we did not observe a significant increase in capacity, while further decay was greatly accelerated (not shown).

Fourthly, the cell degradation may be related to the irreversible loss of Li. However, we used over-built counter electrode and had excess of Li in the system. Therefore, such a scenario (continuous Li loss) would lead to the initial stability of the cell followed by the sudden loss of capacity when the Li excess was exhausted. Since the cell degradation was nearly linear with cycling (and, in fact, initially faster) we find this hypothesis unlikely.

Finally, although a difference in crack density for samples cycled in various

concentrations of aqueous electrolyte and organic electrolyte was not very apparent through SEM, enhanced crack growth plausibly could occur for LFP in aqueous electrolyte due to side reactions. For instance, if the observed surface layer formed on LFP cycled in aqueous solutions is brittle, facture could more easily occur at the crack tip, which could lead to a cycle of re-passivation and fracture. However, because formation of cracks did not affect stability of LFP in organic electrolyte, we believe the impact of cracking on cell degradation is not dominant.

Therefore, based on the discussed above observations we believe that electrochemical separation of the individual particles from the electrode during cycling is a dominant degradation mechanism. This separation is largely impacted by the presence of water in electrolyte. Increasing molarity of aqueous electrolyte thus presents an effective strategy to mitigate the damaging impact of water. Our observation of similar trends of increasing stabilities of other cathodes with increasing aqueous electrolyte molarity suggests that the positive impact of high salt concentration on the stability of ALIBs might be sufficiently broad.

In summary, we have conducted systematic experiments focused on the impact of aqueous electrolyte composition and salt concentration on reversible electrochemical Li deintercalation/intercalation reactions with sub-micron sized $LiFePO_4$. The rate performance and the charge-discharge hysteresis of this material were similar in all aqueous electrolytes and in benchmark organic electrolyte, suggesting that the ionic transport within electrolyte was not a rate-limiting step. The stability of the material was significantly impacted by the electrolyte composition. Higher salt concentration in aqueous electrolyte greatly improved stability. The use of organic electrolyte resulted in virtually

no degradation, consistent with the known literature.[71] Formation of cracks in active material was observed in all cells, including those cycled in organic electrolyte. As such, we conclude that the formation of cracks did not directly impact the cycle stability.

Post-mortem material characterization revealed no structural change in the bulk of the LFP particles, but showed formation of the amorphous surface layer. Thickness of such a layer was found to be electrolyte-dependent and correlated well with the degradation-rate: smaller thickness was consistently observed in more stable cells. Changes in the cycle profiles during cycling indicate that electrical separation of the LFP particles within the electrode during cycling was the most likely root cause of the cell degradation. Since the degradation was significantly impacted by the electrolyte composition, we propose that the undesirable side reactions between the LFP surface with aqueous electrolyte (such as Fe leaching, formation of an insulative layer and surface dissolution) were directly responsible for the electrical separation of the particles and capacity fading during cycling. On a positive note, tuning electrolyte composition could be a promising route for the cell stabilization. In our initial studies with no protective coating, we already demonstrated over 80% capacity retention after 500 cycles. Since the shape of the cyclic voltammetry curves revealed no oxygen evolution at the LFP cathode, this material shows promise as an electrode for low-cost aqueous Li ion batteries.

### 3.3 Experimental Details

***Electrode preparation:*** For constant-current charge-discharge experiments, commercial $LiFePO_4$ (Gelon LIB Co., China), PureBlack C additive (Superior Graphite, USA), and HSV 900 PVDF binder (Kynar, France) were cast onto stainless steel foil

(Trinity Brand Industries, USA) via NMP solvent (Sigma Aldrich, USA) with a 70:15:15 $LiFePO_4$:C:PVDF ratio. The slurry was stirred for at least 2 hours via stir bar and 20 minutes in an IKA Tube Drive before casting a 3 mil thickness via doctor blade. The stainless steel foil was first roughened with 1200/4000P sandpaper and treated with 0.5-1M oxalic acid/deionized water solution (Alfa Aesar, USA) for 3 hours 20 minutes to improve adhesion of the active material layer. After drying in air at room temperature, electrodes were subsequently heated to a maximum temperature of 190-210°C and slowly cooled to melt the PVDF binder to further improve adhesion of the active material layer to the stainless steel.

For cyclic voltammograms, the stainless steel current collector was pre-coated with a C layer. Electrodes were similarly cast with a slurry of $LiFePO_4$ (Gelon LIB Co., China), PureBlack C additive (Superior Graphite, USA), and HSV 900 PVDF binder (Kynar, France) in NMP solvent (Sigma Aldrich, USA) with a 70:15:15 $LiFePO_4$:C:PVDF ratio, dried at room temperature, and heated to a maximum temperature of 190-200°C to improve adhesion of the active material layer to the current collector.

***Electrochemical testing:*** For aqueous electrochemical cells, $LiFePO_4$ working electrodes were punched with ½ inch diameter and $LiFePO_4$ counter electrodes punched with 1 inch diameter. Electrodes were spot welded to stainless steel flags and sandwiched between Teflon blocks using GF/B grade Whatman Glass microfiber filter as a separator. Electrolytes were prepared by dissolving $Li_2SO_4 \cdot H_2O$, $Li_2SO_4$ or $LiNO_3$ salt (minimum 98% purity; Sigma Aldrich and Alfa Aesar, USA) in distilled water. After immersing the cell assemblies in beakers of electrolyte, vacuum was applied for approximately one minute to remove trapped air. Before charge-discharge tests, counter electrodes were initially

delithiated to $Li_{0.47}FePO_4$ by running a constant current between the counter electrode and a third stainless steel flag. The counter electrodes had 4-6 times more active mass than working electrodes (a greater than 1:4 ratio occurred because of variability in mass loading and removal of small areas of active material to enable spot-welding of electrodes).

For organic electrochemical cells, working electrodes were punched with ½ inch diameter and dried under vacuum at 70°C for greater than two days before assembling in 20-32 coin cells opposite Li foil counter electrodes in an Ar-filled glovebox. The electrolyte was BASF Selectilyte A1 Series (1.0M $LiPF_6$ in FEC/EMC 30:70 by volume) and separator Celgard 2500 series. Organic electrochemical cells were rested for at least 19 hours before beginning charge-discharge tests.

Constant-current charge-discharge tests were performed on an Arbin testing system (Arbin Instruments, USA) with potential limits of -0.4 V and +0.4 V for WE versus CE for aqueous electrochemical cells and potential limits as indicated for organic electrochemical cells. EIS measurements were performed on a Gamry Potentiostat with 0.01 Hz to 1MHz frequencies and 10 mV rms amplitude waveform at open circuit potential. Cyclic voltammetry in the potential window of -0.4 to 0.8 V versus Ag/AgCl (3M NaCl) at a scan rate of 0.3 $mV \cdot s^{-1}$ was performed on a Solartron 1480 (Solartron Analytical, USA) multichannel potentiostat. The Ag/AgCl (3M NaCl) reference electrodes were purchased from Bioanalytical Systems, Inc. (USA).

***Post-mortem characterization:*** Electrodes cycled were washed with distilled water (aqueous electrochemical cells) or EMC (organic electrochemical cells) and dried at room temperature prior to further analysis. SEM was conducted with a Hitachi SU8010 Cold

Field Emission SEM as well as LEO 1530 thermally-assisted field emission SEM with EDS. Images were recorded using a variety of accelerating voltages (3-10kV) and EDS spectra were collected using a 10 keV accelerating voltage. Transmission electron microscopy (TEM) images were taken on a Tecnai ™ G2 F30 transmission electron microscope operated at 300 kV and equipped with an Oxford Instruments EDX 6763 for an energy dispersive spectroscopy (EDS). XRD was conducted with an X'Pert PRO Alpha-1 with a Cu K alpha source with a monochromator, using a 45 kV accelerating voltage, 40 mA current. ATR FTIR was conducted with Thermo Scientific Nicolet iS50 with an optical velocity of 0.6329 and resolution of 4 $cm^{-1}$. 32 scans were collected to average for both sample and background signals. Raman spectroscopy was conducted on a Thermo Nicolet Almega XR Dispersive Raman Spectrometer with a 488 nm laser, 50x objective lens and 100 micron pinhole aperture. The collection exposure time was 1.0 s, and 40 sample exposures and 70 background exposures were collected to average. SIMS was conducted with an IONTOF TOF.SIMS$^5$. Once inserted into the TOF.SIMS$^5$, analysis was performed under an UHV of <5e-8 mBar. A 25 kV $Bi^+$ analysis beam was used with a 150x150um analysis window, in positive ion collection mode and with mass collection from 1-800 Da. The sputter source was 2kV $O_2$ with a raster size of 500x500um which was calibrated *vs.* a $SiO_2$/Si wafer to establish an etch rate of 0.36 nm/s for $SiO_2$. XPS was performed on a Thermo K Alpha spectrometer with an Al K alpha source. A pass energy of 50 eV was used for detailed scans and 200 eV for survey scans, with a 0.1 eV resolution.

### 3.4 Chapter Addendum

The benefit of high salt concentration on the cycle stability of $LiFePO_4$ with aqueous electrolytes was also observed in C-D studies with a commercial $LiFePO_4$ powder

obtained from Tatung Co. (rather than Gelon LIB Co.), supporting the universality of this finding. Scanning electron microscopy revealed that the morphology of this particular powder was more oblong (less spherical) than the Gelon LIB Co powder (Figure 38a). XRD confirmed the presence of the olivine crystal structure of $LiFePO_4$ without any obvious crystalline impurity phases, while EDS conducted during SEM revealed the presence of Fe, P, O and C additive with no other impurity elements (Figure 38 b and c). C-D experiments were similarly conducted with a $LiFePO_4$ working electrode assembled opposite a larger, partially-delithiated $LiFePO_4$ counter electrode in a beaker-style setup using aqueous electrolyte of varying salt concentration. Notably, increasing the concentration of $Li_2SO_4$ salt was found to lead to increased discharge capacity retention (see Figure 39). In addition, salt concentration was found to have a minimal impact on the rate capability (see Figure 40). Thus, particle morphology was found to have little impact on the observed trends with regard to electrochemical cycling.

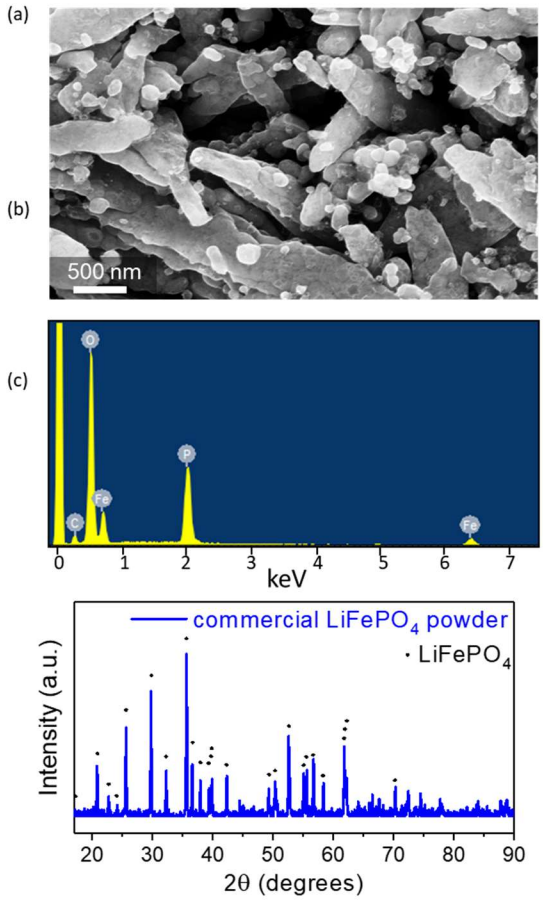


**Figure 38 (a) SEM micrograph of Tatung $LiFePO_4$ powder, (b) EDS spectrum and (c) powder X-ray diffraction pattern.**

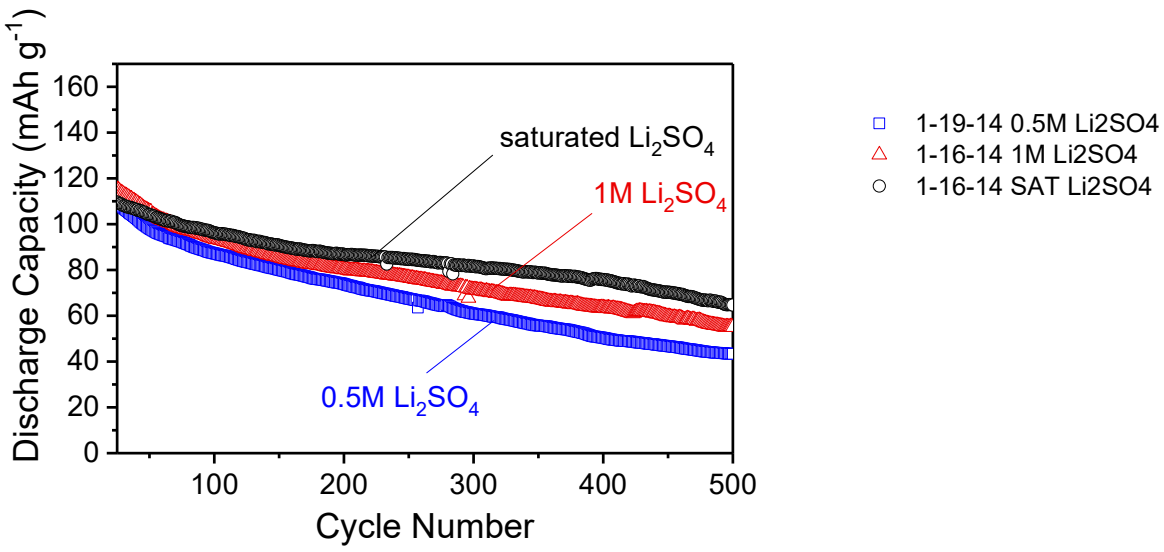


**Figure 39 C-D at a 1C rate for Tatung $LiFePO_4$ working electrodes opposite larger, partially-delithiated Tatung $LiFePO_4$ counter electrodes with varying concentration aqueous $Li_2SO_4$ electrolytes.**

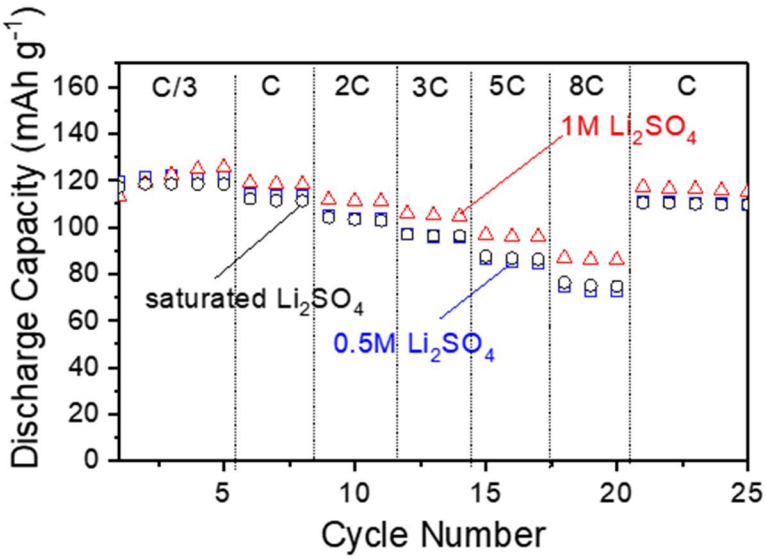


**Figure 40 Rate capability test (C-D) for the same cells as displayed in Figure 39.**

$LiNi_{0.33}Mn_{0.33}Co_{0.33}O_2$ (LMO) is another intercalation cathode material popularly used in commercial LIBs. A preliminary investigation of the electrochemical behavior of this compound in combination of aqueous electrolytes of varying molarity was performed in the form of cyclic voltammograms. As shown in Figure 41, increasing the concentration of $LiNO_3$ salt increases the cycle-to-cycle stability (and also increases the lithiation/delithiation peak potentials). This illustrates that the trends observed for cycle stability as a function of salt concentration may extend to other intercalation materials in combination with aqueous electrolytes, for similar reasons they are observed with $LiFePO_4$ (for instance, higher salt concentration may contribute to lower water activity and thus lower solubility of the intercalation compounds). The benefits of a high electrolyte salt concentration on charge/discharge capacity retention were also observed in a subsequent study on the electrochemical behavior of $LiCoO_2$ in combination with aqueous electrolytes. [54]

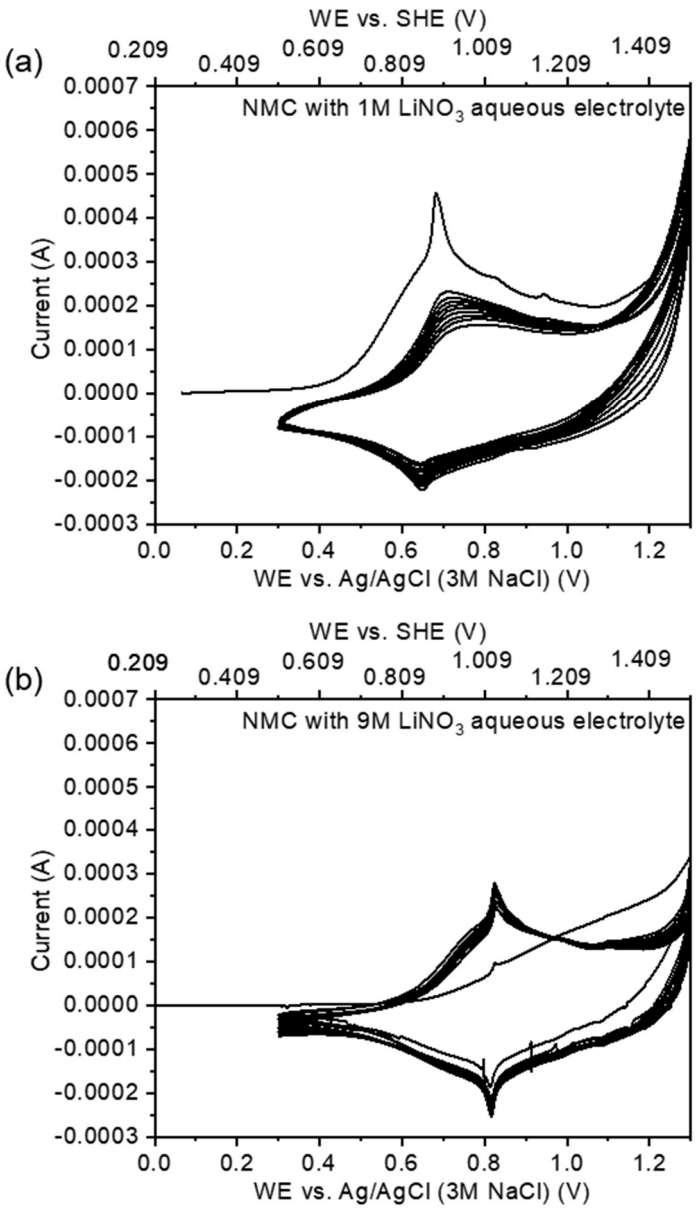


**Figure 41 Cyclic voltammograms for NMC in aqueous $LiNO_3$ electrolytes of 1M or 9M concentration (9M = saturated) using 0.5 mV $s^{-1}$ scan rate.**

# CHAPTER 4. MIXED METAL DIFLUORIDES AS HIGH CAPACITY CONVERSION-TYPE CATHODES: IMPACT OF COMPOSITION ON STABILITY AND PERFORMANCE

*Parts are reproduced with permission from Gordon D., Huang Q., Magasinski A., Ramanujapuram A., Bensalah N, Yushin G. (2018). Mixed Metal Difluorides as High Capacity Conversion-Type Cathodes: Impact of Composition on Stability and Performance. Adv. Energy Mater., 1800213. DOI: 10.1002/aenm.201800213*

## 4.1 Introduction

Metal fluorides are promising candidate compounds for high capacity lithium ion battery (LIB) cathodes that may offer increased cell-level energy density and specific energy over state of the art intercalation materials if coupled with high capacity anodes (such as Li or Si-based) [1]. During discharge, metal fluorides react with $Li^+$ ions and electrons to form new interspersed metal and LiF phases [1]. Insertion of $Li^+$ can occur as a first step of the reduction reaction for metal trifluorides, while for metal difluorides the entire reduction reaction is typically reported to occur as a single step conversion reaction.[72-74] Since more than one $Li^+$ ion can be accommodated per transition metal ion (one for each $F^-$ ion), many metal fluorides offer much greater gravimetric and volumetric capacities than today's state-of-the-art commercial LIB intercalation cathodes such as lithium cobalt oxide (LCO), lithium nickel cobalt manganese oxide (NCM), lithium nickel cobalt aluminum oxide (NCA), among others.[1, 9] Another motivation of moving away from intercalation-type to conversion-type cathodes, such as metal fluorides, is the

potential ability to avoid using toxic cobalt, which induces significant safety hazard during mining, particularly in developing countries where personal protection equipment is not sufficiently controlled.[75] Metal fluoride cathodes constructed with metal fluoride nanoparticles (to shorten electron and ion diffusion pathways) and composites of metal fluorides and electrically conductive carbon or mixed electronic and ionic conductive materials, have substantially improved electrochemical attributes. [76-78] However, large voltage hysteresis and capacity fade remain significant challenges to commercialization.[1] Despite their higher theoretical energy density compared to cells with sulfur (S) cathodes, these materials received dramatically less attention and little is understood about their electrochemical behavior.

While the high electrical resistance of metal fluorides and LiF likely contribute to the hysteresis and capacity fade, the origins of these undesirable attributes remain largely unclear. Wang et al. proposed that the local metal distribution of the lithiated cathode may impact reversibility, based on a comparison of $FeF_2$ (relatively reversible) and $CuF_2$ (relatively irreversible).[73] They suggested that $FeF_2$ transforms into <5nm diameter Fe particles which are well interconnected and interspersed among LiF particles, effectively forming an electrically conductive network for electron travel and high interfacial area for ion diffusion. In contrast, they argued that $CuF_2$ forms larger 5-12 nm diameter Cu particles, which are not interconnected and are more segregated from the LiF particles. In a slightly different take on the impact of local morphology, Li et al. attributed the hysteresis of $FeF_3$ to ohmic voltage drops through resistive phases, a reaction overpotential (neither of these first two factors should be surprising or controversial), and a third factor of "compositional inhomogeneity."[79] That is, they observe that during lithiation and

delithiation there are dissimilar distributions of phases surrounding reaction sites and different pathways for $Li^+$ ions and electrons to reach the current collector or electrolyte, respectively. In contrast, others concluded that voltage hysteresis results from fundamentally different reactions upon charge and discharge. For instance, Ko et al. ascribed the voltage hysteresis for $FeF_2$ to a direct conversion of $FeF_2$ to Fe and LiF and a different reverse reaction involving the intermediate formation of rocksalt $Fe_xLi_{2-2x}F_2$.[80]

Cation and $F^-$ dissolutions into the electrolyte have been proposed as mechanisms of capacity fading. [1, 81] Hua et al. found that while the conversion of $CuF_2$ to Cu and LiF occurs directly (with no intermediate $Cu^+$ oxidation state), $Cu^+$ can be observed during delithiation of the cathode. [81] This intermediate oxidation state of Cu can coordinate with $F^-$ to dissolve the LiF phase into the electrolyte as well. Thus, capacity fades rapidly as a direct result of loss of active material from the cathode. Sin et al., in contrast, attributed the decline in capacity of $FeF_2$ to the increased trapping of $Fe^{2+}$ as FeO within a growing cathode solid electrolyte interphase (CEI) layer, along with incomplete conversion of metallic Fe and LiF back to $FeF_2$ due to the electronic and ionic resistances imposed by this CEI layer. [82] Wang et al. observed that dissolution of Co in the $CoF_2$ during cycling may lead to dramatic growth in the anode solid electrolyte interphase (SEI), which similarly leads to rapid impedance growth and cell-level capacity fading [83]. However, the dissolution of Co could be ameliorated using fluoroethylene carbonate (FEC) solvent additive in order to form a protective CEI layer.

While explanations for the hysteresis and capacity fade require further investigation and clarification, various approaches have been explored to improve metal fluoride electrochemical performance with some very positive results. Gu et al. demonstrated a

method to infiltrate $FeF_2$ into the pores of a spherical C via a $FeSiF_6$ precursor salt solution.[55] They demonstrated high stability, which they argue was the result of the C providing electrical conductivity and a structural backbone, the C pores confining the size of $MF_2$ particles and preventing the segregation of M and LiF phases, and the ability of the C pores to accommodate the volume changes of the active material. Wang et al. extended this methodology to demonstrate relatively stable cycling of multifunctional $CoF_2$-carbon nanotube (CNT) composite cathodes.[83] Gu et al. also explored the use of lithium bis(fluorosulfonyl)-imide (LiFSI) in dimethoxyethane (DME) as an electrolyte with $FeF_2$-infilitrated C composites, as this electrolyte had been previously shown to decompose to form a Li-ion permeable passivating CEI surface layer (particularly with high LiFSI concentration) with the Li-S battery chemistry.[84, 85] Possibly due to prevention of dissolution of the active material through similar CEI surface layer formation, Gu et al. demonstrated high capacity in combination with cycle stability for nearly 1000 cycles (with a loss of no more than 20% of the original capacity).

The desire for a reversible cathode with a higher voltage led Wang et al. to explore the incorporation of Cu metal, although $CuF_2$ has been demonstrated to have poor reversibility. [86] Wang et al. synthesized solid solutions of $CuF_2$ (with a rutile crystal structure) and $FeF_2$ (with a similar monoclinic crystal structure) by ball-milling together the single metal fluorides. They observed two distinct reduction plateaus for the reduction of $Cu^{2+}$ to Cu metal followed by the reduction of $Fe^{2+}$ to Fe metal at a lower potential. Upon charging, they found that Fe is oxidized to $Fe^{2+}$ and subsequently $Fe^{3+}$ concurrently with Cu oxidation to $Cu^{2+}$. The high discharge plateau during the $Cu^{2+}$ to Cu metal transition coupled with the lower voltage hysteresis for $Cu_yFe_{1-y}F_2$ than $CuF_2$ make this an

exciting advance.

In this work, we expand upon the study by Wang et al. on mixed Fe-Cu- difluoride chemistry in order to better understand the general properties of mixed metal difluorides. Our electrochemical testing revealed that in some mixed metal difluorides reduction occurs in a single step at an intermediate reduction potential to that for individual metal fluorides, in sharp contrast to the previously observed behavior [86]. We identified that a solid solution of the two metals is reformed upon repeated lithiation and delithiation. In contrast to previous work on $Cu_yFe_{1-y}F_2$ [86], we did not observe any significant impact of forming mixed $Ni_yFe_{1-y}F_2$, $Co_yFe_{1-y}F_2$ or $Mn_yFe_{1-y}F_2$ on cell stability or voltage hysteresis. However, by synthesizing and conducting electrochemical tests on seven different metal difluoride compositions with very similar morphology and comparing the obtained results, we discovered that the magnitude of the charge transfer impedance for uncycled ("fresh") cathodes correlates well with subsequent cell hysteresis growth and capacity degradation. In addition, the charge transfer resistances were found to grow by the greatest magnitude for the chemistries that suffered the greatest hysteresis growth and the greatest capacity fade during charge-discharge. This implies that the hysteresis growth and capacity degradation may be governed mostly by a resistance to charge transfer, present at the very beginning of cycling and worsening upon repeated lithiation and delithiation. As such, cell performance can be predicted from the initial tests. Post-mortem electron microscopy and energy dispersive spectroscopy point to unfavorable CEI formation as a likely cause of this resistance. Finally, we observed formation of a higher-voltage discharge plateau of some metal difluorides during electrochemical cycling, suggesting the oxidation of the metals from the original $2^+$ to the $3^+$ oxidation state, which was not previously discussed. These

findings provide valuable insights and enhance our understanding of the behavior of metal fluoride cathodes.

## 4.2 Results and Discussion

Single metal difluoride- (s-$MF_2$) and solid solution mixed metal difluoride- (m-$MF_2$) multiwalled carbon nanotube (MWCNT) nanocomposites were synthesized by a facile approach based on a modification of a procedure previously used in our laboratory to obtain s-$MF_2$ and carbon (C) composites. [55, 83] That is, aqueous $MSiF_6$ precursor salt solutions were first prepared and infiltrated onto/into MWCNT powders. The salts were then precipitated upon water evaporation and then converted into metal fluorides upon heat-treatment (see Figure 42). Thermogravimetric analysis revealed that mass loss rapidly occurs – consistent with release of $SiF_4$ and evaporation of water of hydration – before reaching 200°C (with inert gas flow). Thus, for the synthesis of the materials, we raised the tube furnace temperature to 250°C and held it there for 4 hours (with inert gas flow) to ensure complete conversion of the precursor salt to metal difluoride. As further discussed below, powder X-ray diffraction (XRD) confirmed the successful formation of rutile-structured $MF_2$. To synthesize the m-$MF_2$ samples, the procedure was adjusted by mixing precursor salt solutions of two different metal ions before the water was evaporated. Such mixed metal difluoride-MWCNT nanocomposites were prepared for metal compositions not previously studied (Fe-Mn-F, Fe-Co-F and Fe-Ni-F, all with the molar ratio of the two metals chosen to be 1:1).

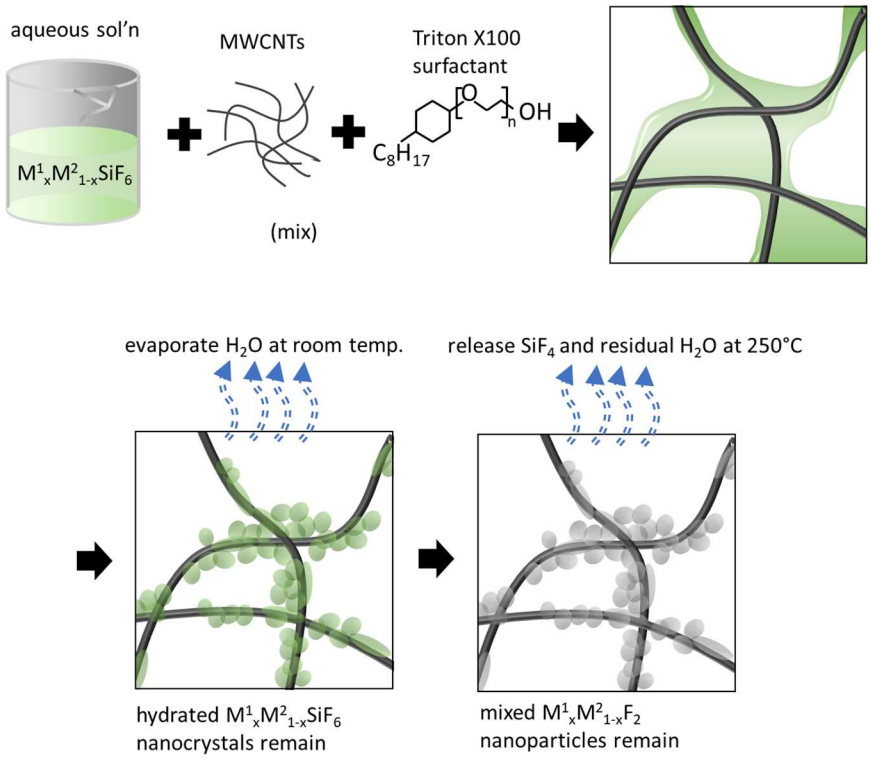


**Figure 42 Diagram of the synthesis process for the nanoparticle $MF_2$ - MWCNT composites.**

CNTs in such composites provided (i) rapid pathways for electron access to the electrochemical reaction sites, (ii) high surface area for deposition of s-$MF_2$ or m-$MF_2$ nanoparticles, which reduce their growth during synthesis and (iii) mechanically robust support, which prevents mechanical degradation of the electrodes during the cycling-induced volume changes [55]. MWCNTs were chosen as the C substrate as they can also be wet by and disperse easily in the utilized aqueous solutions. The proposed approach enabled consistent formation of small and relatively uniform nanoparticles of s-$MF_2$ and m-$MF_2$ (~50 nm in our case). This minimizes ion diffusion distances and electrical

resistance for the intrinsically resistive active material to achieve higher capacity and lower hysteresis. By controlling the s-$MF_2$ or m-$MF_2$ particle size and morphology more tightly than in mechanochemical synthesis (high energy ball milling), we can systematically explore the electrochemical properties of metal difluorides. This approach also aids in the formation of a solid solution without having unreacted single metal difluoride precursor phases.

Scanning electron microscopy (SEM) on each s-$MF_2$- and m-$MF_2$-MWCNT composite showed evenly dispersed $MF_2$ particles among and partially decorating MWCNTs (Figure 43). A transmission electron microscope (TEM) image of a typical region of $MF_2$-MWCNT composite, corroborating observations from SEM, is shown in Figure 45a. We would like to emphasize that despite the changes in the chemical composition of the s-$MF_2$- and m-$MF_2$, morphology of all the produced composites remained indistinguishable by visual observations.

Powder X-ray diffraction (XRD) revealed that the m-$MF_2$ obtained *via* this method are solid solutions of the two different metals and leave behind no single metal fluoride phases. Indeed, the m-$MF_2$-MWCNT powders have peak positions intermediate in angle to those for the corresponding s-$MF_2$-MWCNT powders (Figure 44). This is exceptionally strong indication that the freshly produced m-$MF_2$-MWCNT powders consist of solid solutions of two metals in a rutile crystal structure (with a single, intermediate lattice parameter), rather than intermixed s-$MF_2$ rutile phases (with two distinct lattice parameters). The previously reported $Cu_yFe_{1-y}F_2$ produced by planetary ball-milling two single-metal fluoride compounds showed a similar property [86]. In principle, unique electrochemical behavior may be observed when starting with mixed metal solid solutions

rather than intermixed single metal phases. As such, obtaining solid solutions was highly advantageous for our study.

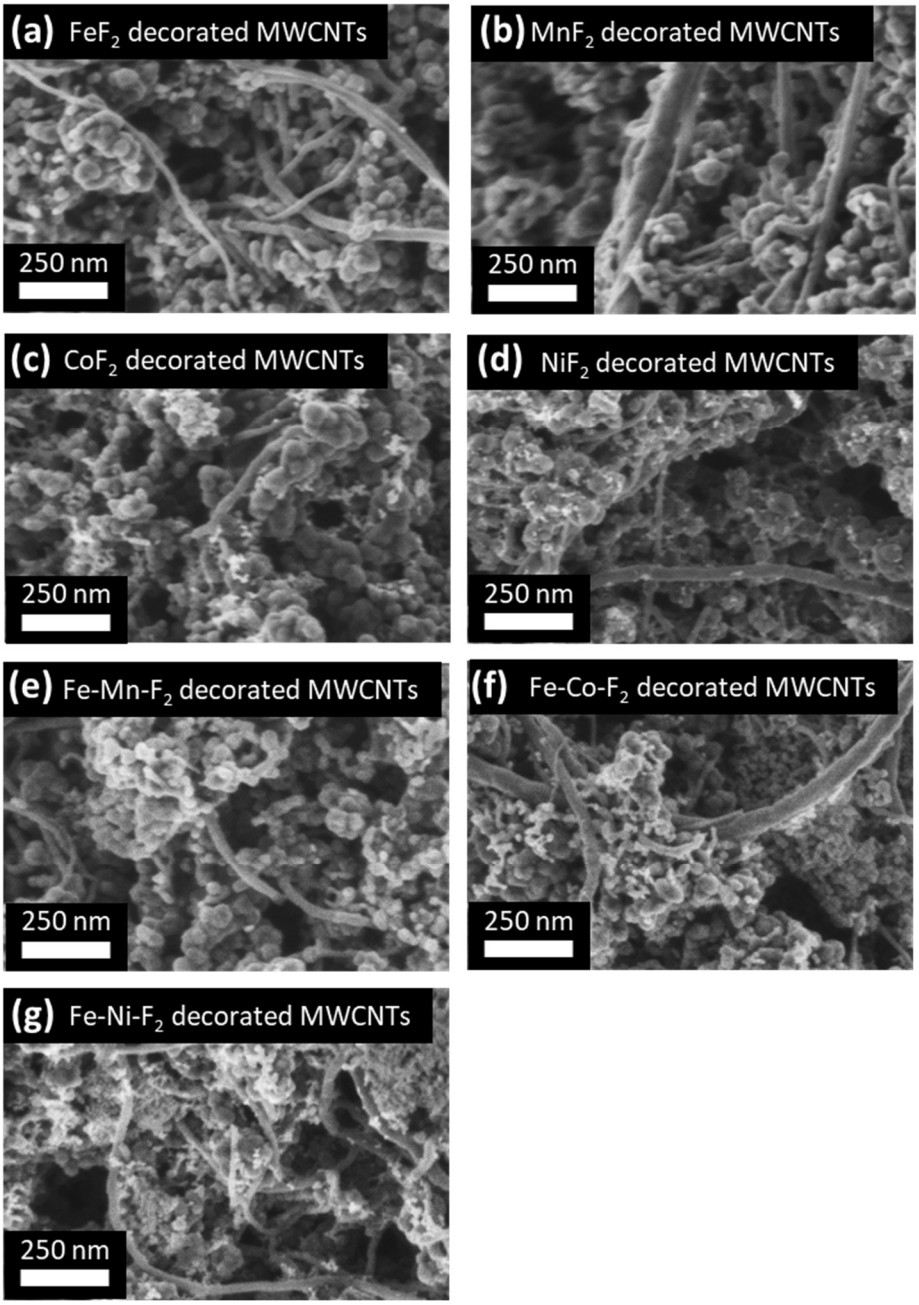


**Figure 43 SEM micrographs of the fresh electrode surface for each metal difluoride composition.**

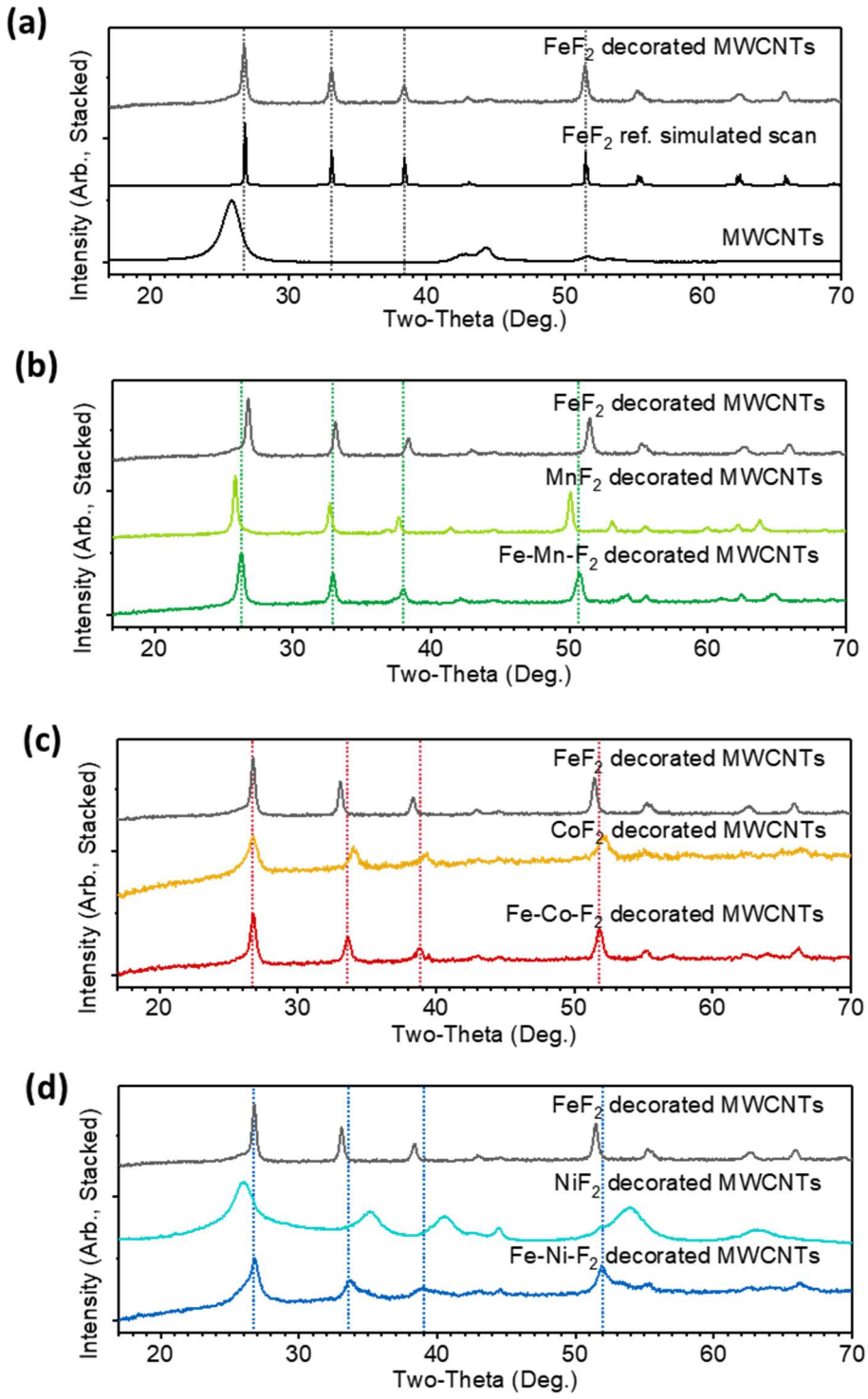


**Figure 44 Powder x-ray diffraction patterns for each metal difluoride composition.**

Selected area electron diffraction (SAED) patterns for m-$MF_2$-MWCNT powders also reveal a set of diffraction rings matching precisely the pattern simulated for a multicrystalline rutile structure (Figure 45 b-d). We note from the high resolution TEM images that in fact typical particles consist of multiple grains/crystals of different orientations, consistent with the ring formations in the SAED patterns. Energy-dispersive x-ray spectroscopy (EDS) line scans (Figure 46) across m-$MF_2$ particles or clusters of particles show that the two metals are present/track together in each instance, providing further evidence that for the fresh samples the metals are not segregated into different phases.

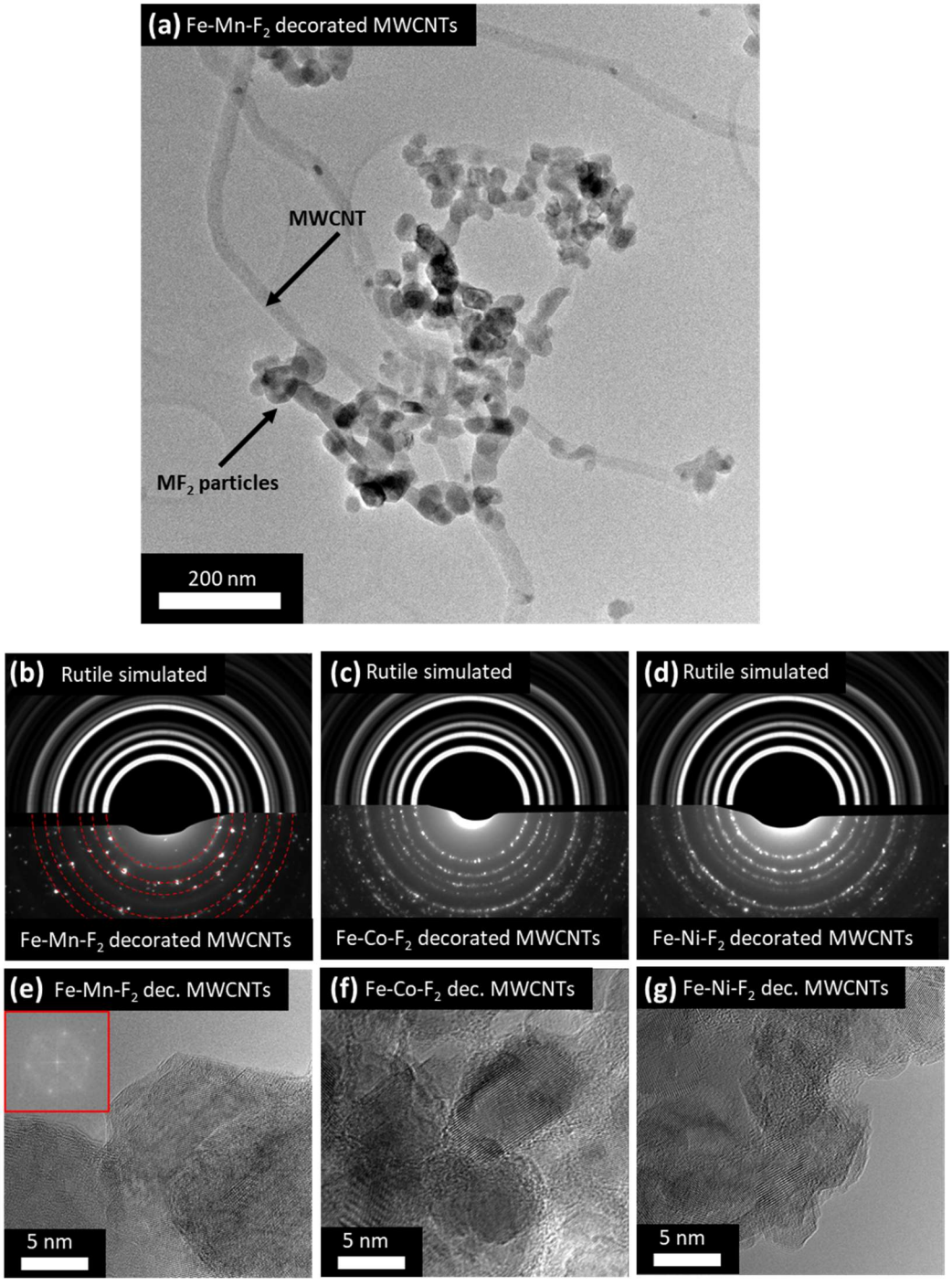


**Figure 45 (a) TEM micrograph of a typical MWCNT-$MF_2$ composite, (b-d) SAED patterns for mixed metal difluoride-MWCNT composites compared with a simulated pattern for a multicrystalline rutile phase (based off of a $MnF_2$ PDF card using PDF-4+), (e-g) and high resolution TEM micrographs of mixed metal difluoride particles.**

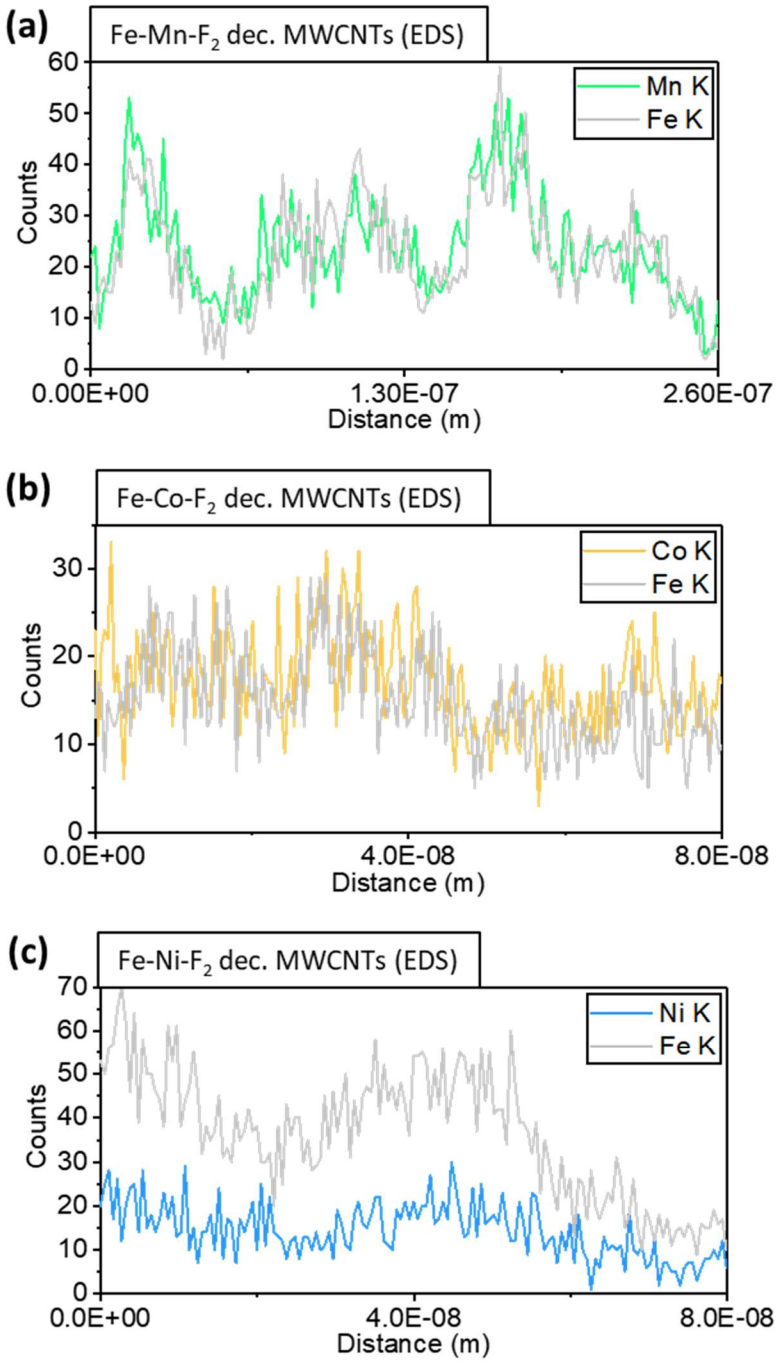


**Figure 46 EDS line scans through clusters of mixed metal difluoride particles.**

The electrochemical behavior was studied via charge-discharge experiments (C-D, Figure 47 a-d, Figure 48), cyclic voltammetry (CV, Figure 49) and electrochemical impedance spectroscopy (EIS, Figure 47e, Figure 50). All electrochemical testing was conducted with Li metal counter electrodes in 2032 coin cells. Working electrodes consisted of 1:1 $MF_2$:C ratio by mass (with the C consisting of a 1:1 ratio of MWCNTs present during the $MF_2$ synthesis to PureBlack® C additive only used in casting electrodes) along with a standard PVDF binder, cast onto Al foil. For C-D experiments, a wide voltage window was chosen (0.4V to 4.0V) such that the fullest redox behavior could be observed for each metal difluoride composition, given the differing redox potentials and the large hysteresis, along with a consistent discharge current of 140 mA $g^{-1}$. For instance, the lithiation of $MnF_2$ initially occurs with an average potential lower than 1V vs. $Li/Li^+$ (Fig. 5 b), while delithiation of LiF/Fe to reform $FeF_2$ occurs with an average potential greater than 2.5V vs. $Li/Li^+$ (Figure 48e), both values being within 0.4V to 4.0V vs. $Li/Li^+$. Meanwhile, this voltage window also avoids Al current collector lithiation and excessive electrolyte decomposition at more extreme voltages.

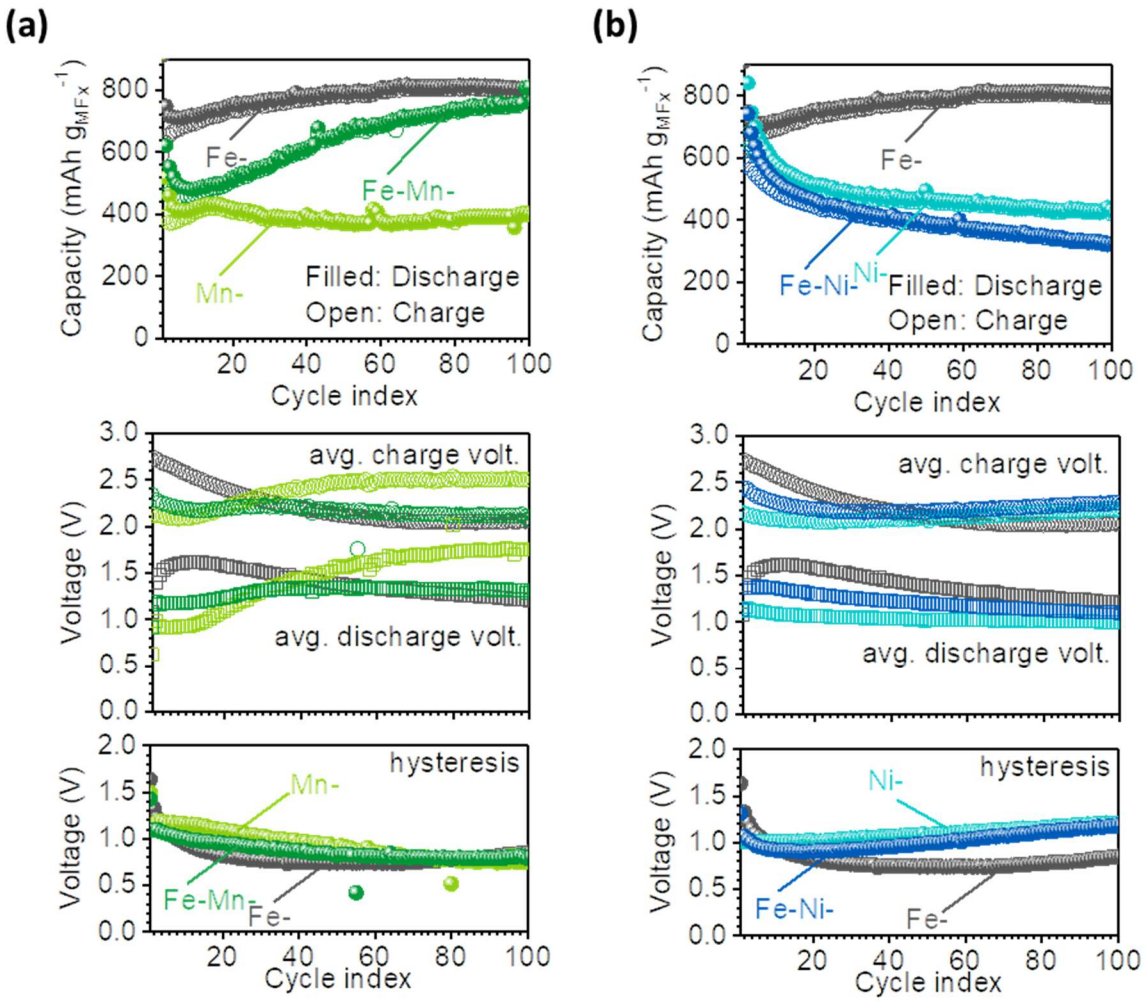


**Figure 47 Gravimetric discharge capacities for each metal difluoride composition, average voltage and hysteresis (avg. charge voltage minus avg. discharge voltage) for each cell, (d) Coulombic efficiency for each cell, and (e) Nyquist plot for EIS from 0.1 Hz to 1MHz with a 10mV rms AC voltage for uncycled (fresh) cells.**

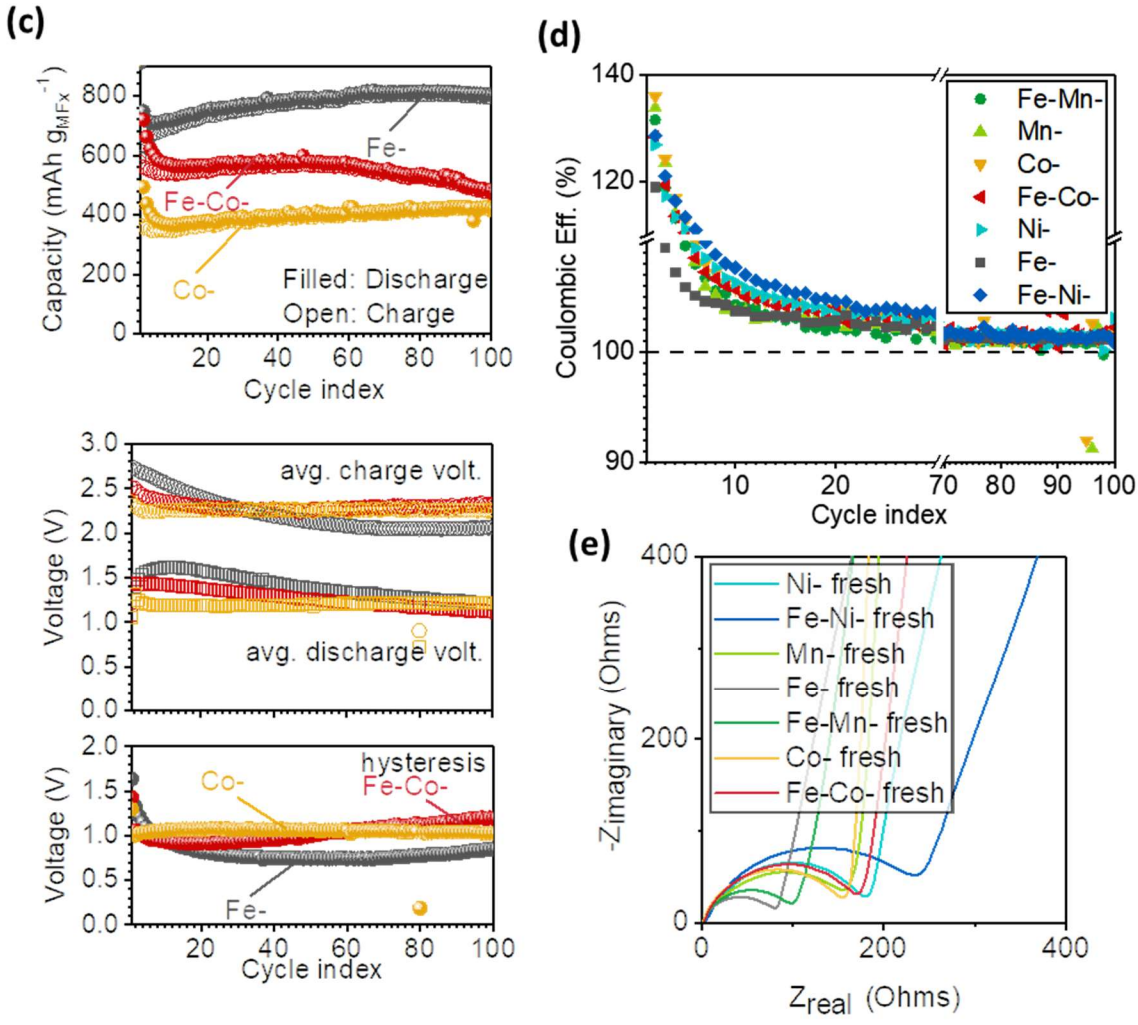


**Figure 47 continued**

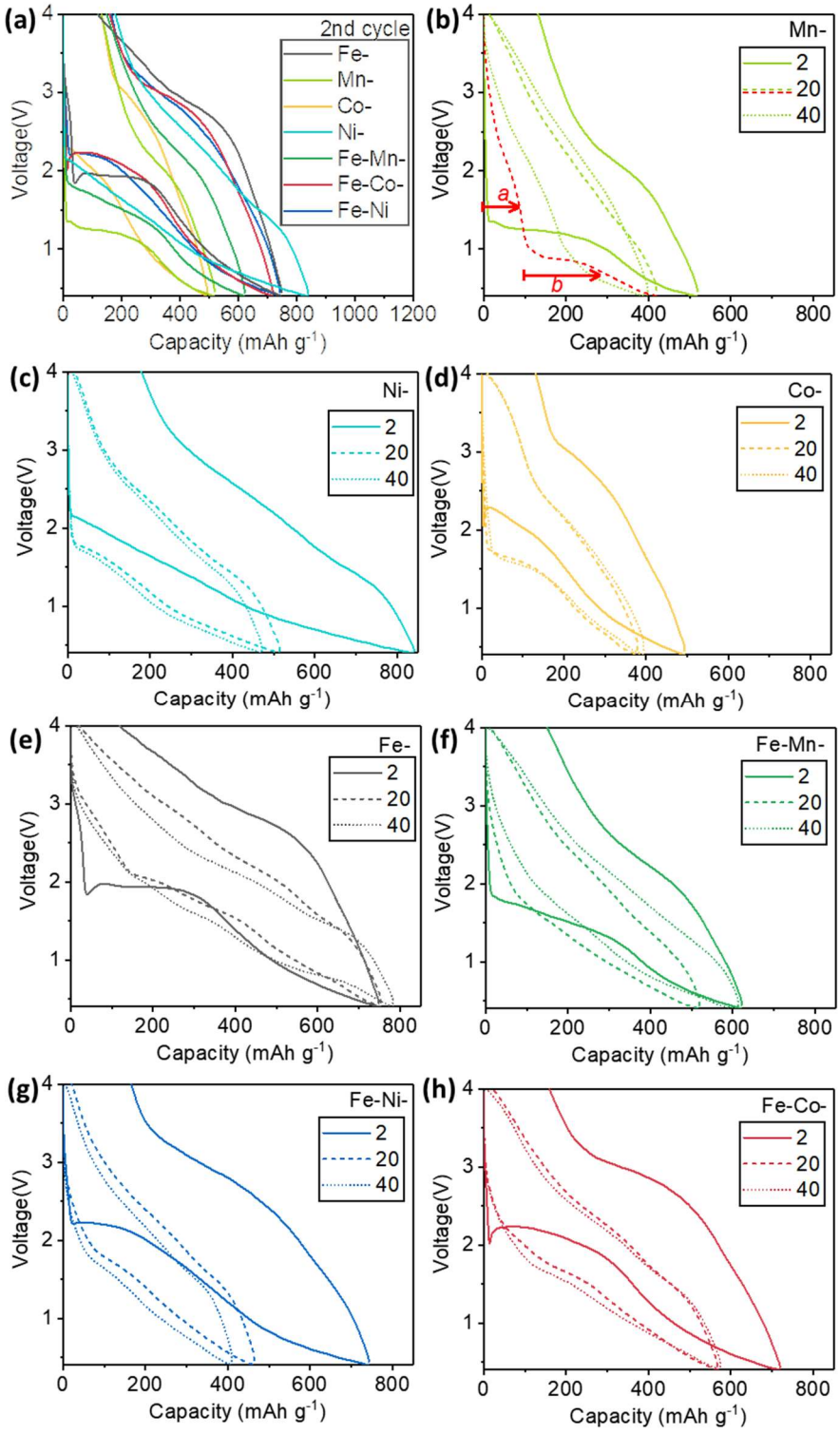


**Figure 48 (a) Voltage-capacity profiles for the 2nd cycle for each metal composition, (b-h) 2nd, 20th and 40th cycle voltage-capacity profiles for each metal difluoride composition.**

Capacities measured in the first 100 cycles range between 400 and 800 mAh $g^{-1}$. These are all significantly higher capacities than those of commercial intercalation cathodes, which typically exhibit a maximum capacity of ~200 mAh $g^{-1}$ or less.[9] Slightly higher than theoretical capacities for some cells should not be surprising due to the decomposition of the electrolyte. Electrolyte reduction and a solid-electrolyte-interphase formation on the electrode surface during the initial discharge to low potentials is a known phenomenon [19] and was evidenced by the coulombic efficiency (CE) deviating substantially from 100% (Fig. 4d). Since the conversion material constantly expands and contracts, the CEI would be expected to partially reform in each cycle.

Interestingly, faster decay in cell capacity correlates well the growing nature of the voltage hysteresis. Indeed, cells which decrease in capacity over the first 100 C-D cycles – Fe-Ni-, Ni- and Fe-Co- chemistries – simultaneously show increase in hysteresis (Figure 47a-c). Conversely, cells which demonstrate excellent stability in capacity or even increasing capacity over the first 100 C-D cycles – Fe-, Mn-, Co, and Fe-Mn- chemistries – demonstrate stable or declining hysteresis (Figure 47a-c). This suggests that either the capacity degradation originates from the growth of a large hysteresis or the origin/cause of the hysteresis is similar to that of the capacity degradation.

The average charge and discharge voltages for m-$MF_2$-MWCNT cells lie between those for the corresponding s-$MF_2$-MWCNT cells (Figure 47a-c), as might be expected for solid solutions or mixed single metal phases. Also notable is the gradual increase in C-D potential in case of Mn- chemistry. The voltage profiles reveal that a second lithiation peak emerges at a higher potential than the original (see the two distinct voltage plateaus are marked as “a” and “b” in Figure 48b). While the average charge and discharge voltages do

not increase dramatically, a separate discharge pleateau at a higher voltage also emerges over the first 20 cycles for $FeF_2$. The steeply sloped/rounded beginning of the discharge profile for Fe-Mn-$F_2$ at 20 cycles – distinct from the single plateau for the first few cycles – similarly suggests the emergence of higher potential redox reaction(s). We propose that this phenomenon likely indicates the progressive oxidation of some of the metal to the 3+ oxidation state, as metal difluorides should transform *via* a single step conversion reaction, as observed in earlier cycles.

Cyclic voltammograms with the same voltage limits as for C-D (0.4 – 4.0 V) and 0.3 mV $s^{-1}$ scan rate corroborate the observations with C-D. A single narrow reduction peak for $FeF_2$ (and some other s-$MF_2$ and m-$MF_2$) can only be clearly distinguished after a small number of cycles (e.g., the $5^{th}$ cycle). Between the $5^{th}$ and $20^{th}$ CV cycles, a single large reduction peak for $FeF_2$ transforms into two distinct reduction peaks (compare Figure 49a-c with Figure 49d-f). The initial Fe-Mn-$F_2$ reduction occurs at an intermediate potential between $FeF_2$ and $MnF_2$ within a single reduction peak (likely in a single reduction step). The reduction reaction continues to occur at an intermediate potential even after 20 CV cycles. This suggests that the individual metals begin in and repeatedly reform a m-$MF_2$ with a characteristic reduction potential intermediate to those for corresponding single metal difluorides. To explain this result, we reason that given the intermediate lattice parameter for the rutile-structured solid solution mixed metal difluorides, the energetics of the conversion reactions are substantially different from the corresponding single-metal difluorides as the conversion reactions involve the breaking and reforming of bonds in which the bond lengths are different than the single-metal difluorides. Also, we expect that the reduction of one metal and then the other metal (instead of simultaneous reduction of

the two metals) would not be energetically preferred because this would require forming an additional single-metal difluoride phase and energetic phase-boundaries, which would increase the Gibbs Free energy of the system. This stands in sharp contrast to the previously reported findings where separate reduction reactions corresponding to the transition of $Cu^{2+}$ to Cu metal and $Fe^{2+}$ to Fe metal were observed [86]. Interestingly, they also find that Fe-Cu-$F_2$ reforms a solid solution upon delithiation with concurrent oxidation of the metals. Since the conversion potentials for Fe-, Ni- and Co- are shown to be similar, we would not expect to easily observe an intermediate potential conversion reaction for Fe-Co-$F_2$ or Fe-Ni-$F_2$.

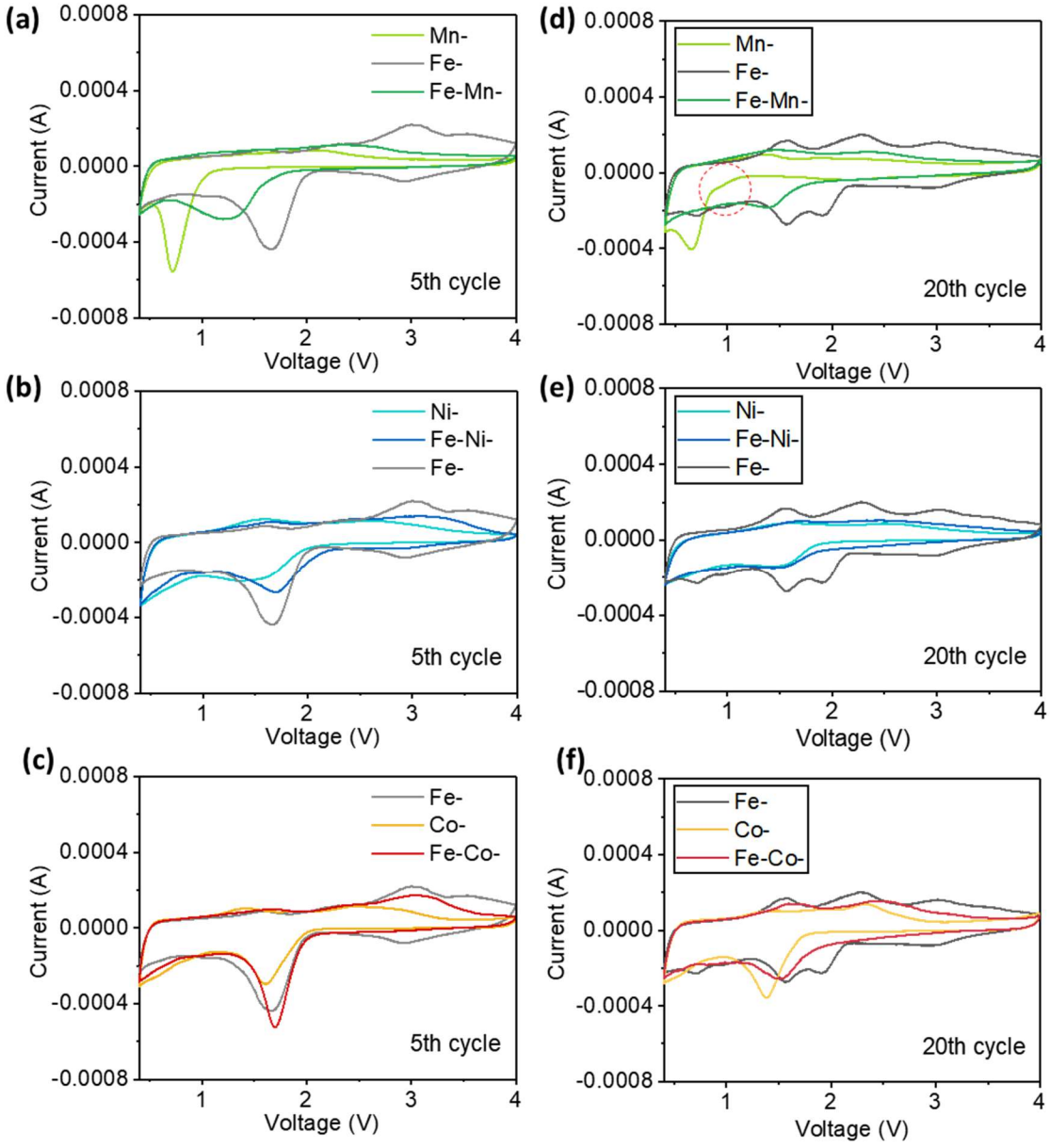


**Figure 49 Cyclic voltammograms of metal difluoride-MWCNT vs. Li foil cells with a scan rate of 0.3 mV s-1 between 0.4 and 4V for each metal fluoride composition: (a-c) 5th cycle and (d-e) 20th cycle.**

Electrochemical impedance spectroscopy (EIS) was performed both on uncycled cells and cells after 1, 5, 9, 13, 17, or 21 CV cycles (Figure 50). Studying the results for uncycled cells, clear impedance arcs, reflecting a resistance and capacitance in parallel, are observed for each chemistry. We observe that the diameter of the semicircles, equal to the magnitude of the resistance, is relatively large for cells which greatly decline in capacity and increase in hysteresis during the first 100 C-D cycles: Fe-Co, Ni-, and especially Fe-Ni- chemistries. Conversely, the semi-circle diameter is the smallest for Fe-, Mn-, Co, and Fe-Mn chemistries, which have relatively stable or decreasing hysteresis and stable or increasing capacity over the first 100 C-D cycles. In addition, we observe that the semi-circle diameter increases the most over the course of CV for those chemistries which degrade in capacity the quickest during C-D. For instance, the Fe-Ni- cell after 17 cycles has an impedance arc with a diameter/charge transfer resistance on the order of 800 Ohms, approximately twice that of the cell with the next highest charge transfer resistance after this many cycles. This demonstrates that *changes* in the magnitude charge transfer impedance after repeated lithiation and delithiation also correlate with hysteresis growth and cell degradation during C-D.

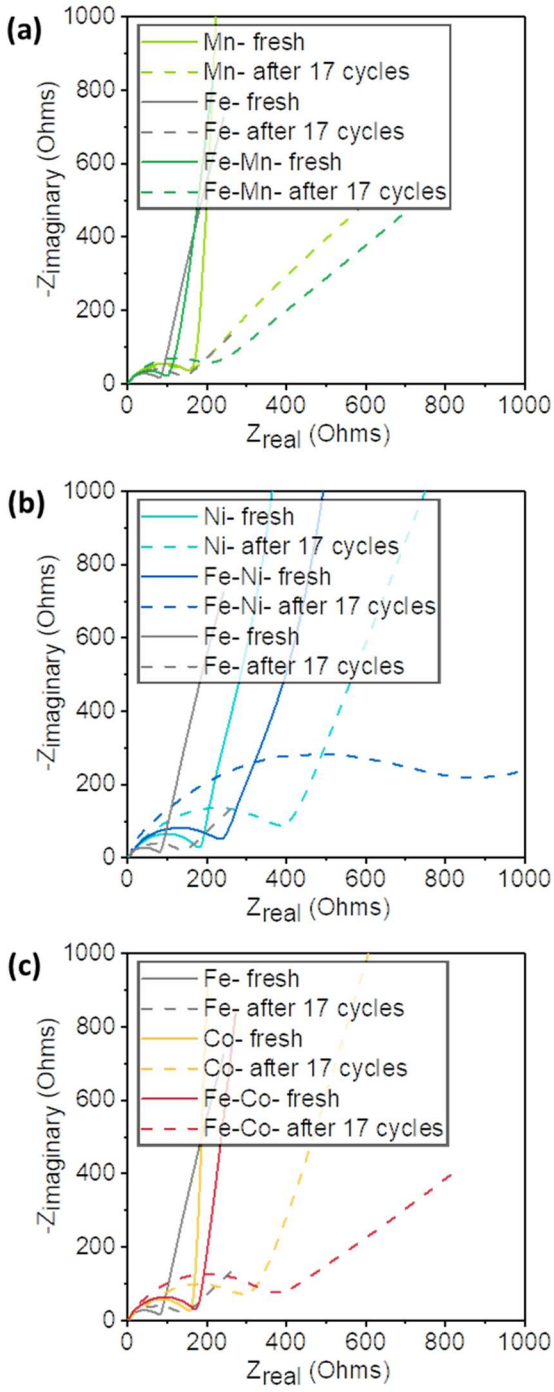


**Figure 50 Nyquist plots for EIS from 0.1 Hz to 1MHz with a 10mV rms AC voltage after pausing cyclic voltammograms at 4V (CVs were resumed at OCV).**

If charge transfer resistance governs not only cell energy efficiency (voltage hysteresis), but also the capacity fading, then the loss of active material (via metal and LiF dissolution) should not be a key degradation mechanism in our samples. The charge transfer resistance is dependent on the metal composition and arises from some phenomenon present at the very beginning of cycling where dissolution is not significant. To test this hypothesis, we conducted additional tests and post-mortem analysis on both working and Li counter electrodes.

Interestingly, EDS conducted during SEM of the Li metal counter electrodes for Ni- and Fe-Ni- chemistry cells after 500 C-D cycles (which suffered very large capacity degradation) did not reveal the presence of any transition metal on the surface (see Figure 51). This strongly suggests that significant metal dissolution did not occur, as some portion of any amount of transition metal that dissolved into the electrolyte would be expected to reach the Li metal counter electrode and spontaneously plate onto the Li metal surface. This supports the study by Wang et al. [86], in which Fe and Co were not found on the Li metal surface if FEC additives were utilized (as they are in the present study).

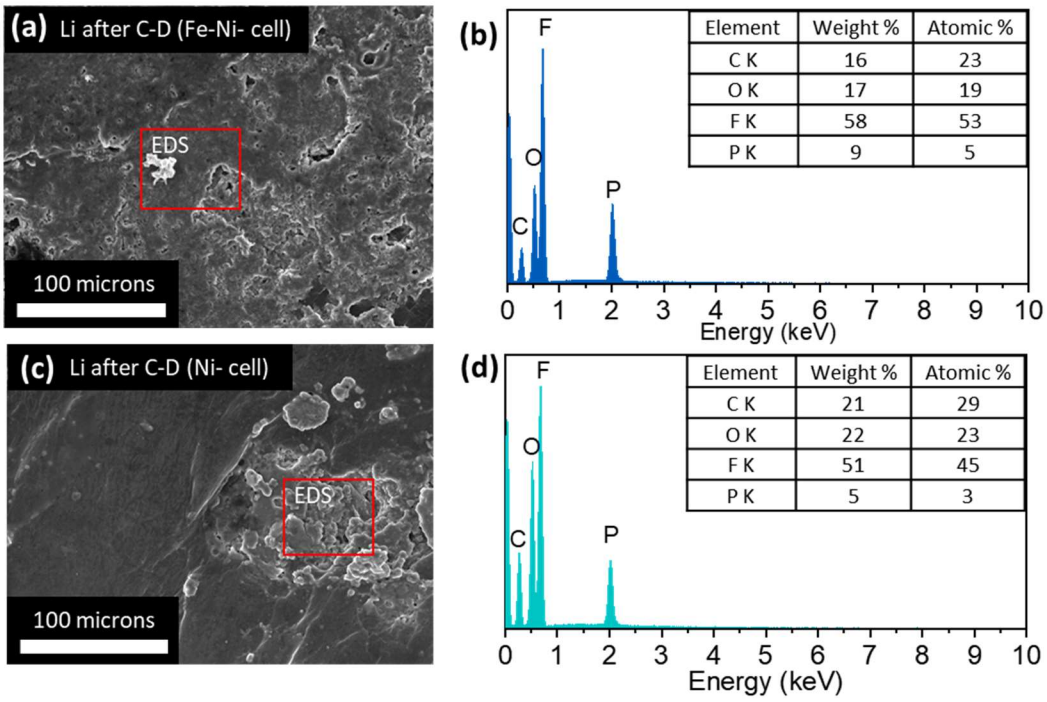


**Figure 51 SEM micrograph of Li foil after C-D (unwashed after disassembly) from Fe-Ni-$F_2$ cell (a) and $NiF_2$ cell (c) with corresponding EDS spectra (b,d).**

Meanwhile, by conducting electron microscopy on the working electrodes after cycling, we find evidence of significant surface layer (CEI) formation that is correlated with relatively large capacity fade during C-D, initial charge transfer impedance and growth of the charge transfer impedance during CV. SEM of Fe, Ni- and Fe-Ni- working electrodes after just 20 C-D cycles reveals significant growth of a surface layer in the case of Ni- and Fe-Ni- chemistries, but not in the case of Fe. That is, the smooth surface of $MF_2$ nanoparticles and $MF_2$-decorated MWCNTs becomes rougher and particle dimensions/radii of the coated MWCNTs increase for Ni- and Fe-Ni- chemistries. (See Figure 52.) The rough surface features observed on the Fe-Ni- working electrode in SEM were also observed in TEM as surface layer protrusions from particles. (Figure 53a.)

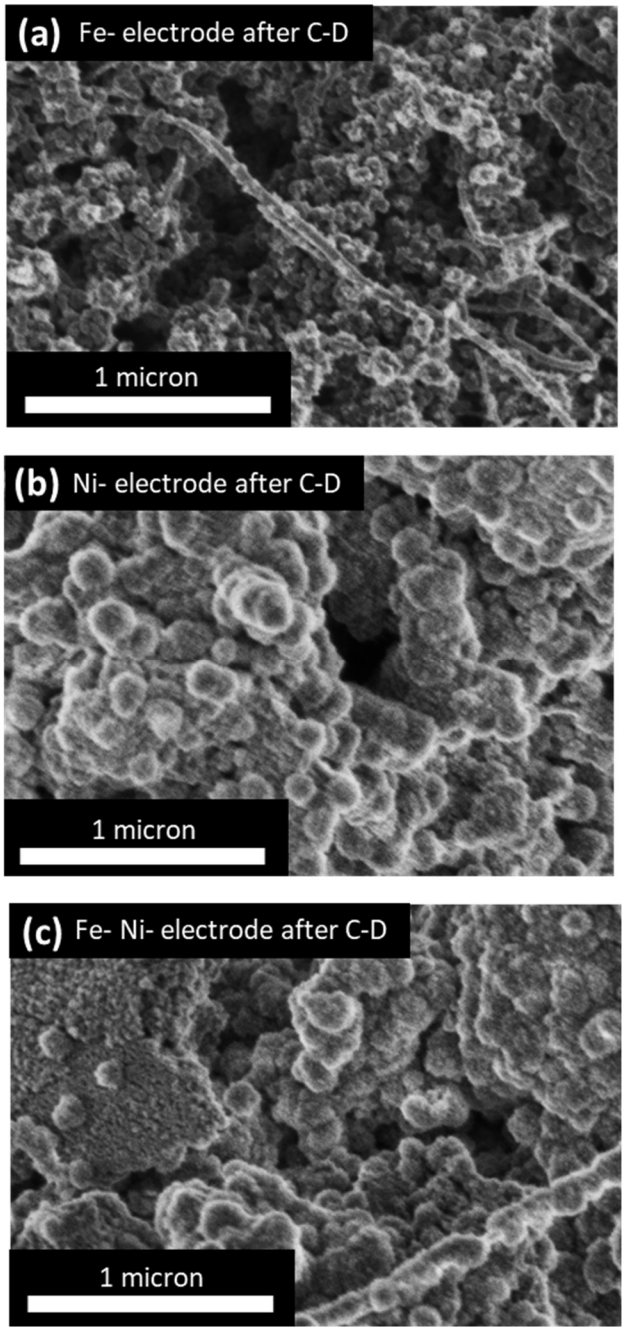


**Figure 52 SEM micrographs of the surfaces of Fe-, Ni- and Fe-Ni-$F_2$-MWCNT electrodes after C-D**

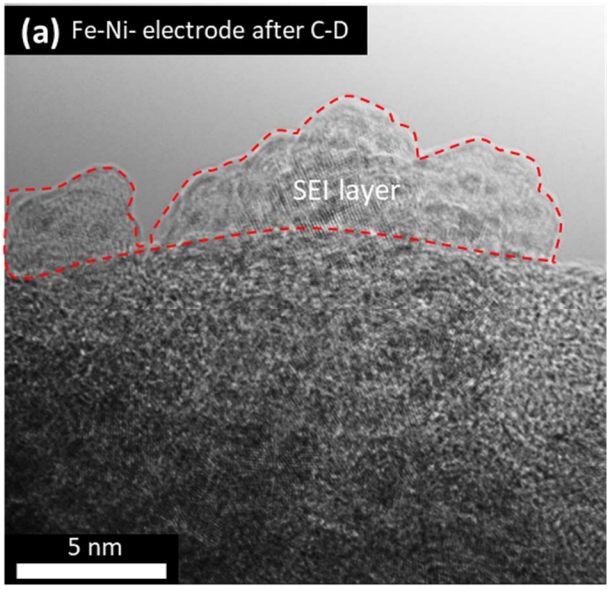


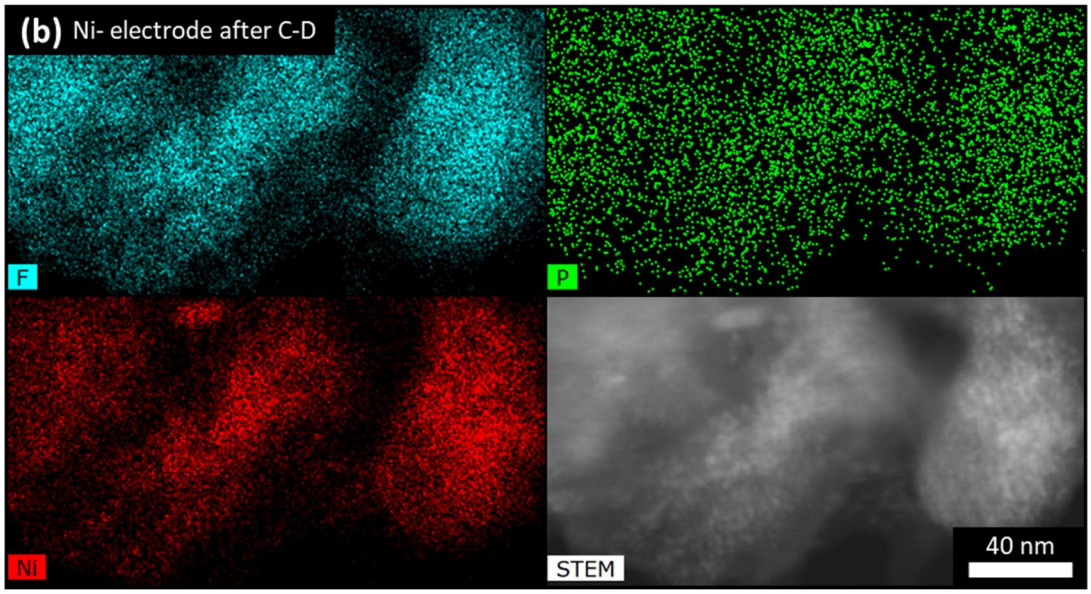


**Figure 53 (a) TEM micrographs of surface layers formed on Fe-Ni-$F_2$-MWCNT electrode after C-D (b) STEM image and EDS mapping of $NiF_2$-MWCNT electrode after C-D.**

In order to ascribe the surface layer formation to electrolyte decomposition (CEI formation) or else identify another phenomenon, we performed STEM with EDS mapping on a $NiF_2$-MWCNT electrode after 500 C-D cycles (at which point it has lost much capacity). (See Figure 53b.) P, an electrolyte constituent due to the use of $LiPF_6$ salt, appeared to be distributed relatively evenly across active material particles, consistent with relatively even coverage of the surface with a CEI layer. In contrast, Ni tracks more closely with high intensity (or high contrast) spherical deposits on the order of ~5 nanometers, which are likely Ni metal or $NiF_2$. As a side note, we observe that F tracks relatively closely with Ni (F is present in the CEI layer as well, but at a lower concentration relative to the bulk active material), indicating little segregation of Ni and F. Furthermore, returning to the C-D results, we see that Coulombic efficiency deviates from 100% the most for those cells which develop a surface layer visible through electron microscopy (Figure 47d; compare Ni- and Fe-Ni- with Fe-). This is consistent with additional reduction of electrolyte on the working electrode surface to form the CEI. Thus, we hypothesize that different transition metals may catalyze the growth of the CEI to varying degrees – with Co and Ni inducing a thicker, more resistive CEI layer. Alternatively, it is possible that the CEI forms at different potentials on the reduced metallic nanoparticle surfaces (for instance, it would form at higher potentials for Ni and Co than Fe and Mn since these nanoparticles themselves form at higher potentials), giving rise to more or less favorable CEI with regard to the resistance it introduces.

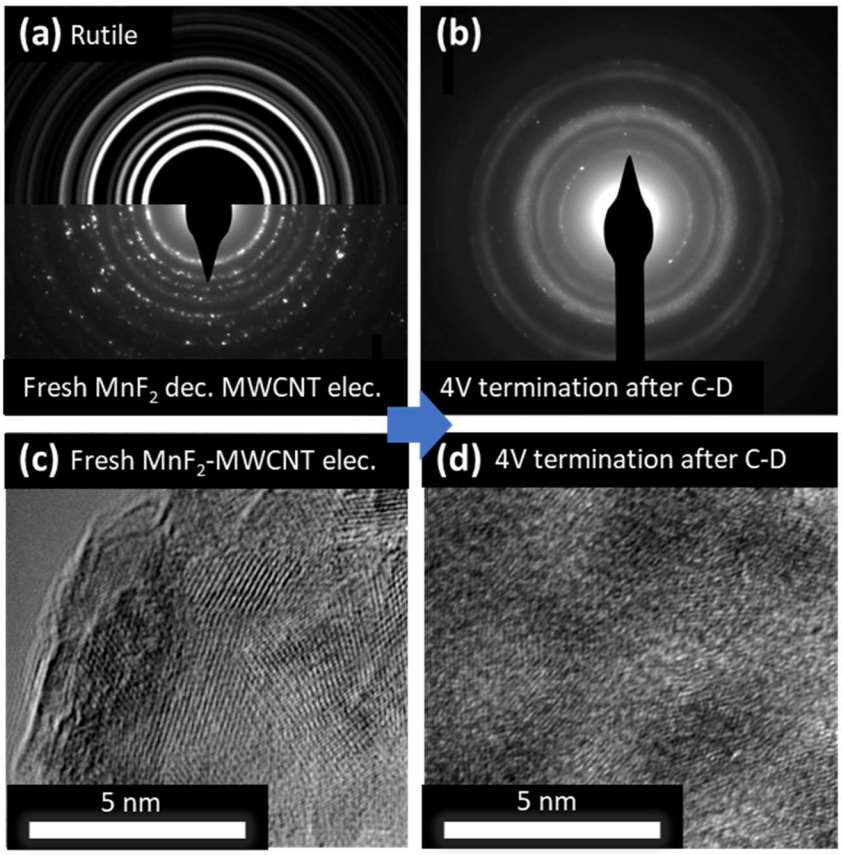


**Figure 54 Fresh $MnF_2$ MWCNT electrode: (a) SAED pattern compared with a simulated pattern for a multicrystalline rutile phase (based off of a $MnF_2$ PDF card using PDF-4+) and (c) high resolution TEM micrograph. $MnF_2$ MWCNT electrode terminated at 4V after 20 C-D cycles: (b) SAED pattern compared with the simulated multicrystalline rutile pattern and (d) high resolution TEM micrograph.**

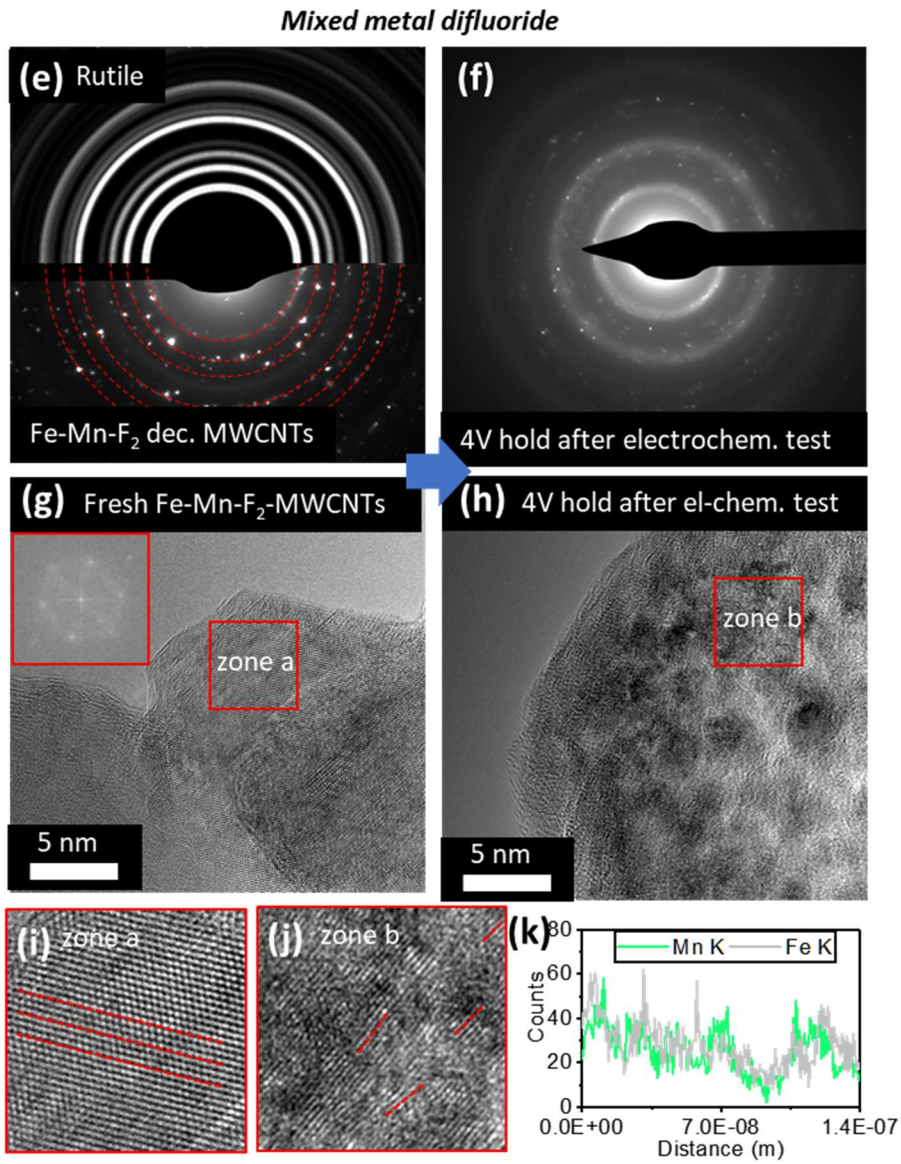


**Figure 55 Fresh Fe-Mn-$F_2$ MWCNT electrode: (e) SAED pattern compared with the simulated multicrystalline rutile pattern (g, i) high resolution TEM image. Fe-Mn-$F_2$ MWCNT electrode held at 4V after a series of CVs and voltage holds between 0.4V and 4V: (f) SAED pattern and (h, j) high resolution TEM micrograph. (k) EDS line scan of Fe-Mn-$F_2$ MWCNT electrode after electrochemical testing.**

Post-mortem TEM was also conducted on selected single- and mixed- metal fluoride-MWCNT composite materials after repeated lithiation and delithiation to detect changes of the crystal structure of the particles. As shown in Figure 55, Mn- and mixed Fe-Mn- samples (terminated at 4V during C-D or after a 4V voltage hold following a series of CVs and lower voltage holds) both have dense spherical deposits within particles, which are likely metal or metal oxide (from the oxidation of high surface area metal nanoparticles during the transfer of the sample through air to the TEM instrument). The formation of some metal fluoride with the metal(s) in the 3+ oxidation state, leaving some metallic particles unable to recombine into metal fluorides, may explain both this observation and the emergence to varying degrees of additional redox reactions in the C-D and CV studies (Figure 48 and Figure 49). Electron diffraction patterns consist of much more diffuse rings than the fresh samples for both single Mn- and mixed Fe-Mn- chemistries. This suggests the possibility of the formation of very small metal fluoride crystallites in each sample. EDS line scans performed through clusters of particles during TEM reveal that metals of the Fe-Mn- mixed metal fluoride sample do not strongly segregate during repeated lithiation and delithiation, consistent with the conclusion that mixed metal fluorides reform on each cycle.

## 4.3 Summary

We wish to emphasize several general observations and conclusions important for the further development of metal fluoride cathodes. Firstly, in this work we demonstrated that the general approach of using metal salt precursors can be successfully applied to synthesize additional single metal difluorides (Mn, Ni) and multiple solid solution mixed metal difluorides (Fe-Co-, Fe-Mn-, Fe-Ni-). This methodology allowed us to produce metal

difluoride particles with even and consistent size and morphology and incorporate MWCNTs or other conductive additives during the synthesis process for systematic studies of the impact of metal composition on electrochemical behavior.

Secondly, we discovered that a mixed metal difluoride can undergo reduction in a single step with a reduction potential intermediate to those for the corresponding single-metal difluorides. This contrasts with the study by Wang et al. on mixed Fe-Cu-$F_2$, where the reduction of $Cu^{2+}$ and $Fe^{2+}$ to Cu and Fe metal occur at two different reduction potentials. However, similar to their studies, we observed that a solid solution of the two components is reformed upon charging.

Thirdly, in the course of these studies, we observed the evolution of a single conversion reaction between $MF_2$ and M + $LiF_2$ to as many as three separable oxidation reactions and two separable reduction reactions (for $FeF_2$). This can be explained by the progressive formation of metal fluorides with some of the metal ions oxidized to the 3+ state of charge, whereby metal that cannot be accommodated remains as nanoparticles.

Finally, we find that the magnitude of the initial cathode charge-transfer resistance (for uncycled cells) as well as the magnitude of the charge-transfer resistance growth during CV correlate with the rates of hysteresis growth and capacity fade during C-D cycling. The opportunity to recognize this correlation arises from the fact that seven different metal difluoride compositions were systematically investigated in this study (Fe-, Mn-, Ni-, Co-, Fe-Mn-, Fe-Co-, Fe-Ni-). This insight indicates the likelihood that growth of a charge transfer impedance gives rise to the worsening hysteresis and capacity fade. Selected SEM and TEM post-mortem studies reveal the formation of a surface layer on the

working electrode for cells which degrade rapidly (Fe-, Fe-Ni-) and the absence of such a layer for a stable cell (Fe-). This illustrates the likely role of transition metal-dependent CEI layer formation in the growth of a large charge-transfer impedance and the critical importance to achieve stable CEI via suitable material selection.

## 4.4 Experimental Details

*Active Material Preparation:* In a typical synthesis process, metal precursor powder (Fe, Mn, $CoCO_3$, or $NiCO_3$) was dissolved/reacted in 10 g $H_2SiF_6$ acid aqueous solution (23% acid by mass) and stirred at room temperature. In order to ensure that the acid fully reacted with the metal precursor (that is, near complete formation of $MSiF_6$ from $H_2SiF_6$), the metal precursor was added in excess. Once fully reacted, the solution was centrifuged to remove the excess solids and diluted with water to 15 mL total volume. The mixed Fe-Co-$SiF_6$, Fe-Mn-$SiF_6$ and Fe-Ni-$SiF_6$ solutions were made by mixing equal volumes of the single metal salt solutions (of equal concentration) such that the ratio of Fe:Co, Fe:Mn and Fe:Ni was 1:1. MWCNTs with length of 10-30 nm (US Research Nanomaterials, Inc., USA) were added to each solution, with a MWCNT mass equal to half that of the final active material mass (calculated from the known number of moles of metal in the solution). Each solution was poured into a plastic container and dried at room temperature overnight. Each powder was then annealed at 250 degrees C for 4 hours under Argon flow.

*Electrode Preparation:* PVDF (Alfa Aesar, USA) binder was fully dissolved in NMP and then the MWCNT-$MF_2$ composite powder and additional PureBlack C conductive additive stirred in. The mass of PureBlack equaled the mass of the MWCNTs,

such that the ratio of PureBlack:MWCNTs:$MF_2$ was 1:1:2. The binder constituted 15% of the final electrode film mass. The slurry was cast with 3 mil thickness onto Al foil using a Doctor Blade and dried in air and then under vacuum at ~70 degrees C, and from there brought directly into an inert gas glovebox. The amount of active material in each cell was on the order of 0.5-0.6 mg.

*Electrochemical Testing:* Working electrodes were punched with a ½ inch diameter and assembled in 2032 stainless steel coin cell casings with Li foil counter electrodes. The electrolyte was BASF Selectilyte A1 series (1.0 M $LiPF_6$ in FEC/EMC 30:70 by volume) and separator Celgard 2400 series. Constant-current C-D tests were performed using an Arbin testing system (Arbin Instruments, USA) with voltage limits of 0.4V and 4V for the working electrode versus the Li foil counter electrode. EIS measurements were performed using a Gamry Potentiostat using a frequency range of 0.1 Hz to 1 MHz for a 10 mV rms AC voltage. Cyclic voltammetry was performed with the same Gamry instrument using a 0.3 mV $s^{-1}$ scan rate and the same voltage limits as for C-D (0.4V and 4V).

*Postmortem Characterization:* Coin cells were disassembled and the working electrodes rinsed with DMC and dried at room temperature prior to further analysis. Li metal counter electrodes were not rinsed to preserve any trace metal on the surface. SEM was performed with a Hitachi SU8010 Cold Field Emission SEM as well as a LEO 1539 Thermally Assisted Field Emission SEM with EDS. Images were recorded using a variety of accelerating voltages (1-15 keV) and EDS spectra were collected using a 15keV accelerating voltage. TEM images were taken with a Tecnai G2 F30 TEM operated at 300 kV and equipped with an Oxford Instruments EDX 6763 for EDS. XRD was conducted with an X'Pert PRO Alpha-1 with a CuK alpha source with a monochromator using a 45

kV accelerating voltage and 40 mA current. STEM with EDS mapping was conducted with a Hitachi HD-2700.

## 4.5 Chapter Addendum

Selected XPS results are displayed in Figure 56. These results are consistent with the formation of a CEI layer during C-D. LiF is detected following C-D, based on the F1s peak binding energy. Meanwhile, the FWHM for peaks associated with the presence of C are broader after C-D, indicating the presence of C in an SEI layer (in addition to the C in the form of MWCNTs and PureBlack additive).

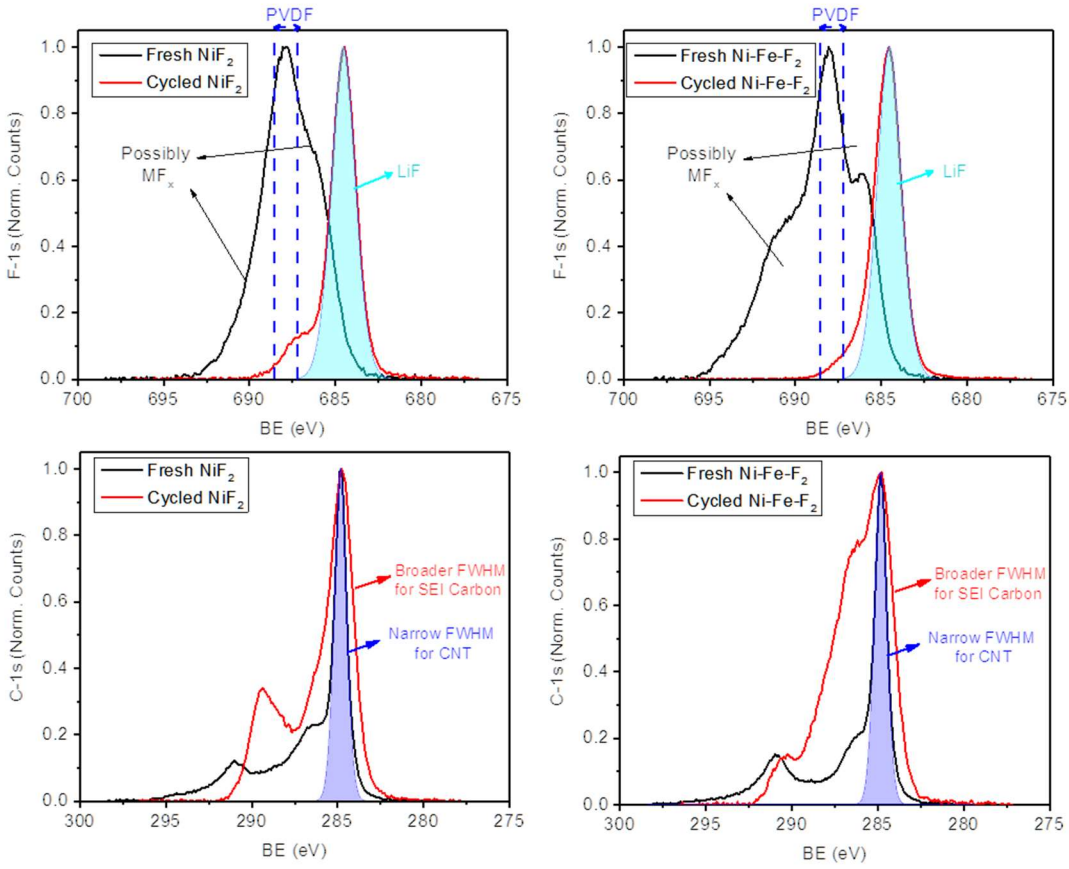


**Figure 56 XPS of fresh and cycled Ni-containing $MF_2$-MWCNT electrodes**

# REFERENCES


1. Wu, F. and G. Yushin, *Conversion cathodes for rechargeable lithium and lithium-ion batteries.* Energy & Environmental Science, 2017. **10**(2): p. 435-459.
2. Kerman, K., et al., *Review—Practical Challenges Hindering the Development of Solid State Li Ion Batteries.* Journal of The Electrochemical Society, 2017. **164**(7): p. A1731-A1744.
3. Ohta, S., et al., *Llz Oxide and LPS Sulfide Composite Solid Electrolyte for Lithium Ion Battery.* Meeting Abstracts, 2016. MA2016-02(5): p. 857.
4. Xu, R., et al., *Recent Developments of All-Solid-State Lithium Secondary Batteries with Sulfide Inorganic Electrolytes.* Chemistry – A European Journal. **0**(0).
5. Gu, W. and G. Yushin, *Review of nanostructured carbon materials for electrochemical capacitor applications: advantages and limitations of activated carbon, carbide-derived carbon, zeolite-templated carbon, carbon aerogels, carbon nanotubes, onion-like carbon, and graphene.* Wiley Interdisciplinary Reviews: Energy and Environment, 2014. **3**(5): p. 424-473.
6. Bard, A.J. and L.R. Faulkner, *Electrochemical Methods: Fundamentals and Applications*. 2000: Wiley.
7. Linden, D. and T. B Reddy, *Handbook of Batteries, 3rd Edition*. 2001.
8. Nitta, N. and G. Yushin, *High-Capacity Anode Materials for Lithium-Ion Batteries: Choice of Elements and Structures for Active Particles.* Particle & Particle Systems Characterization, 2014. **31**(3): p. 317-336.
9. Nitta, N., et al., *Li-ion battery materials: present and future.* Materials Today, 2015. **18**(5): p. 252-264.
10. Padhi, A.K., K.S. Nanjundaswamy, and J.B. Goodenough, *Phospho-olivines as Positive-Electrode Materials for Rechargeable Lithium Batteries.* Journal of The Electrochemical Society, 1997. **144**(4): p. 1188-1194.
11. Wang, Y., et al., *The Design of a $LiFePO_4$/Carbon Nanocomposite With a Core–Shell Structure and Its Synthesis by an In Situ Polymerization Restriction Method.* Angewandte Chemie International Edition, 2008. **47**(39): p. 7461-7465.
12. Qin, G., et al., *The morphology controlled synthesis of 3D networking $LiFePO_4$ with multiwalled-carbon nanotubes for Li-ion batteries.* CrystEngComm, 2014. **16**(2): p. 260-269.
13. Wang, B., et al., *Growth of $LiFePO_4$ nanoplatelets with orientated (010) facets on graphene for fast lithium storage.* Materials Letters, 2014. **118**: p. 137-141.
14. Meethong, N., et al., *Aliovalent Substitutions in Olivine Lithium Iron Phosphate and Impact on Structure and Properties.* Advanced Functional Materials, 2009. **19**(7): p. 1060-1070.
15. Bai, P., D.A. Cogswell, and M.Z. Bazant, *Suppression of Phase Separation in $LiFePO_4$ Nanoparticles During Battery Discharge.* Nano Letters, 2011. **11**(11): p. 4890-4896.

16. Wang, F., et al., *Tracking lithium transport and electrochemical reactions in nanoparticles.* Nature Communications, 2012. **3**: p. 1201.
17. Flamme, B., et al., *Guidelines to design organic electrolytes for lithium-ion batteries: environmental impact, physicochemical and electrochemical properties.* Green Chemistry, 2017. **19**(8): p. 1828-1849.
18. Aurbach, D., et al., *Design of electrolyte solutions for Li and Li-ion batteries: A review*. Vol. 50. 2004. 247-254.
19. Michan, A.L., et al., *Fluoroethylene Carbonate and Vinylene Carbonate Reduction: Understanding Lithium-Ion Battery Electrolyte Additives and Solid Electrolyte Interphase Formation.* Chemistry of Materials, 2016. **28**(22): p. 8149-8159.
20. Peled, E. and S. Menkin, *Review—SEI: Past, Present and Future.* Journal of The Electrochemical Society, 2017. **164**(7): p. A1703-A1719.
21. Weber, C.J., et al., *Material review of Li ion battery separators.* AIP Conference Proceedings, 2014. **1597**(1): p. 66-81.
22. Whitehead, A.H. and M. Schreiber, *Current Collectors for Positive Electrodes of Lithium-Based Batteries.* Journal of The Electrochemical Society, 2005. **152**(11): p. A2105-A2113.
23. Markovsky, B., et al., *On the Electrochemical Behavior of Aluminum Electrodes in Nonaqueous Electrolyte Solutions of Lithium Salts.* Journal of The Electrochemical Society, 2010. **157**(4): p. A423-A429.
24. Spahr, M., *Carbon-Conductive Additives for Lithium-Ion Batteries*. 2009.
25. Coelho, J., et al., *Lithium Titanate/Carbon Nanotubes Composites Processed by Ultrasound Irradiation as Anodes for Lithium Ion Batteries.* Scientific Reports, 2017. **7**(1): p. 7614.
26. Wang, L., et al., *SBR-PVDF based binder for the application of SLMP in graphite anodes.* RSC Advances, 2013. **3**(35): p. 15022-15027.
27. Wessells, C., R.A. Huggins, and Y. Cui, *Recent results on aqueous electrolyte cells.* Journal of Power Sources, 2011. **196**(5): p. 2884-2888.
28. Zhao, M., et al., *Excellent rate capabilities of ($LiFePO_4$/C)//$LiV_3O_8$ in an optimized aqueous solution electrolyte.* Journal of Power Sources, 2013. **232**: p. 181-186.
29. Mikhael, L., et al., *Ultrafast anode for high voltage aqueous Li-ion batteries*. Vol. 16. 2012. pp 3443-3448.
30. Minakshi, M., et al., *Electrochemical behavior of anatase $TiO_2$ in aqueous lithium hydroxide electrolyte*. Vol. 36. 2006. 599-602.
31. Liu, S., et al., *Rechargeable Aqueous Lithium-Ion Battery of $TiO_2$/$LiMn_2O_4$ with a High Voltage.* Journal of The Electrochemical Society, 2011. **158**(12): p. A1490-A1497.
32. Li, W., J.R. Dahn, and D.S. Wainwright, *Rechargeable Lithium Batteries with Aqueous Electrolytes.* Science, 1994. **264**(5162): p. 1115-1118.
33. Li, W. and J.R. Dahn, *Lithium-Ion Cells with Aqueous Electrolytes.* Journal of The Electrochemical Society, 1995. **142**(6): p. 1742-1746.
34. He, P., et al., *Investigation on capacity fading of $LiFePO_4$ in aqueous electrolyte.* Electrochimica Acta, 2011. **56**(5): p. 2351-2357.

35. Kandhasamy, S., A. Pandey, and M. Minakshi, *Polyvinylpyrrolidone assisted sol–gel route $LiCo_{1/3}Mn_{1/3}Ni_{1/3}PO_4$ composite cathode for aqueous rechargeable battery*. Vol. 60. 2012. 170-176.
36. Shao, J., et al., *Core-shell sulfur@polypyrrole composites as high-capacity materials for aqueous rechargeable batteries.* Nanoscale, 2013. **5**(4): p. 1460-1464.
37. Wang, G., et al., *An Aqueous Rechargeable Lithium Battery with Good Cycling Performance.* Angewandte Chemie International Edition, 2007. **46**(1-2): p. 295-297.
38. Ruffo, R., et al., *Electrochemical behavior of $LiCoO_2$ as aqueous lithium-ion battery electrodes.* Electrochemistry Communications, 2009. **11**(2): p. 247-249.
39. Reiman, K.H., et al., *Lithium insertion into $TiO_2$ from aqueous solution – Facilitated by nanostructure.* Electrochemistry Communications, 2006. **8**(4): p. 517-522.
40. Vujković, M., et al., *Gel-combustion synthesis of $LiFePO_4$/C composite with improved capacity retention in aerated aqueous electrolyte solution.* Electrochimica Acta, 2013. **92**: p. 248-256.
41. Minakshi, M., *Lithium intercalation into amorphous $FePO_4$ cathode in aqueous solutions*. Vol. 55. 2010. 9174-9178.
42. Bao, J., et al., *$Li_{0.3}V_2O_5$ with high lithium diffusion rate: a promising anode material for aqueous lithium-ion batteries with superior rate performance.* Journal of Materials Chemistry A, 2013. **1**(17): p. 5423-5429.
43. Suo, L., et al., *"Water-in-salt" electrolyte enables high-voltage aqueous lithium-ion chemistries.* Science, 2015. **350**(6263): p. 938-943.
44. Lux, S.F., et al., *LiTFSI Stability in Water and Its Possible Use in Aqueous Lithium-Ion Batteries: pH Dependency, Electrochemical Window and Temperature Stability.* Journal of The Electrochemical Society, 2013. **160**(10): p. A1694-A1700.
45. Roth, E. and C.J. Orendorff, *How Electrolytes Influence Battery Safety*. Vol. 21. 2012. 45-49.
46. Yang, C., et al., *4.0 V Aqueous Li-Ion Batteries.* Joule, 2017. **1**(1): p. 122-132.
47. Chang, Z., et al., *A lithium ion battery using an aqueous electrolyte solution.* Scientific Reports, 2016. **6**: p. 28421.
48. Luo, J.-Y., et al., *Raising the cycling stability of aqueous lithium-ion batteries by eliminating oxygen in the electrolyte.* Nat Chem, 2010. **2**(9): p. 760-765.
49. Suo, L., et al., *Advanced High-Voltage Aqueous Lithium-Ion Battery Enabled by "Water-in-Bisalt" Electrolyte.* Angewandte Chemie International Edition, 2016. **55**(25): p. 7136-7141.
50. Yang, C., et al., *Flexible Aqueous Li-Ion Battery with High Energy and Power Densities.* Advanced Materials, 2017. **29**(44): p. 1701972.
51. Yamada, Y., et al., *Hydrate-melt electrolytes for high-energy-density aqueous batteries.* Nature Energy, 2016. **1**: p. 16129.
52. Wang, X., et al., *An Aqueous Rechargeable Lithium Battery Using Coated Li Metal as Anode.* Scientific Reports, 2013. **3**: p. 1401.
53. Wang, Y., J. Yi, and Y. Xia, *Recent Progress in Aqueous Lithium-Ion Batteries.* Advanced Energy Materials, 2012. **2**(7): p. 830-840.

54. Ramanujapuram, A., et al., *Degradation and stabilization of lithium cobalt oxide in aqueous electrolytes.* Energy & Environmental Science, 2016. **9**(5): p. 1841-1848.
55. Gu, W., et al., *Metal Fluorides Nanoconfined in Carbon Nanopores as Reversible High Capacity Cathodes for Li and Li-Ion Rechargeable Batteries: $FeF_2$ as an Example.* Advanced Energy Materials, 2015. **5**(4): p. n/a-n/a.
56. Verbrugge, M.W. and P. Liu, *Analytic Solutions and Experimental Data for Cyclic Voltammetry and Constant-Power Operation of Capacitors Consistent with HEV Applications.* Journal of The Electrochemical Society, 2006. **153**(6): p. A1237-A1245.
57. Butler, H.J., et al., *Using Raman spectroscopy to characterize biological materials.* Nature Protocols, 2016. **11**: p. 664.
58. Wang, X., et al., *An Aqueous Rechargeable Lithium Battery Using Coated Li Metal as Anode.* Sci. Rep., 2013. **3**.
59. Porcher, W., et al., *Is $LiFePO_4$ Stable in Water?: Toward Greener Li–Ion Batteries.* Electrochemical and Solid-State Letters, 2008. **11**(1): p. A4-A8.
60. Zhou, F., et al., *The Li intercalation potential of $LiMPO_4$ and $LiMSiO_4$ olivines with M=Fe, Mn, Co, Ni.* Electrochemistry Communications, 2004. **6**(11): p. 1144-1148.
61. Cogswell, D.A. and M.Z. Bazant, *Theory of Coherent Nucleation in Phase-Separating Nanoparticles.* Nano Letters, 2013. **13**(7): p. 3036-3041.
62. Zhu, Y., et al., *In Situ Atomic-Scale Imaging of Phase Boundary Migration in FePO4 Microparticles During Electrochemical Lithiation.* Advanced Materials, 2013. **25**(38): p. 5461-5466.
63. Niu, J., et al., *In Situ Observation of Random Solid Solution Zone in LiFePO4 Electrode.* Nano Letters, 2014. **14**(7): p. 4005-4010.
64. Kao, Y.-H., et al., *Overpotential-Dependent Phase Transformation Pathways in Lithium Iron Phosphate Battery Electrodes.* Chemistry of Materials, 2010. **22**(21): p. 5845-5855.
65. Malik, R., F. Zhou, and G. Ceder, *Kinetics of non-equilibrium lithium incorporation in $LiFePO_4$.* Nat Mater, 2011. **10**(8): p. 587-590.
66. Gabrisch, H., J. Wilcox, and M.M. Doeff, *TEM Studies of Carbon Coated $LiFePO_4$ After Charge Discharge Cycling.* ECS Transactions, 2007. **3**(36): p. 29-36.
67. Chen, G., X. Song, and T.J. Richardson, *Electron Microscopy Study of the $LiFePO_4$ to $FePO_4$ Phase Transition.* Electrochemical and Solid-State Letters, 2006. **9**(6): p. A295-A298.
68. Yu, Y.-S., et al., *Dependence on crystal size of the nanoscale chemical phase distribution and fracture in $Li_xFePO_4$.* Nano Letters, 2015.
69. Ait Salah, A., et al., *FTIR features of lithium-iron phosphates as electrode materials for rechargeable lithium batteries.* Spectrochimica Acta Part A: Molecular and Biomolecular Spectroscopy, 2006. **65**(5): p. 1007-1013.
70. Lee, J.T., et al., *Sulfur-Infiltrated Micro- and Mesoporous Silicon Carbide-Derived Carbon Cathode for High-Performance Lithium Sulfur Batteries.* Advanced Materials, 2013. **25**(33): p. 4573-4579.

71. Omar, N., et al., *Lithium iron phosphate based battery – Assessment of the aging parameters and development of cycle life model.* Applied Energy, 2014. **113**: p. 1575-1585.
72. Conte, D.E. and N. Pinna, *A review on the application of iron(III) fluorides as positive electrodes for secondary cells.* Materials for Renewable and Sustainable Energy, 2014. **3**(4): p. 37.
73. Wang, F., et al., *Conversion Reaction Mechanisms in Lithium Ion Batteries: Study of the Binary Metal Fluoride Electrodes.* Journal of the American Chemical Society, 2011. **133**(46): p. 18828-18836.
74. Zhang, W., et al., *In Situ Electrochemical XAFS Studies on an Iron Fluoride High-Capacity Cathode Material for Rechargeable Lithium Batteries.* The Journal of Physical Chemistry C, 2013. **117**(22): p. 11498-11505.
75. Frankel, T.C., *The cobalt pipeline: Tracing the path from deadly hand-dug mines in Congo to consumers' phones and laptops.* The Washington Post, 2016.
76. Badway, F., et al., *Structure and Electrochemistry of Copper Fluoride Nanocomposites Utilizing Mixed Conducting Matrices.* Chemistry of Materials, 2007. **19**(17): p. 4129-4141.
77. Kim, S.-W., et al., *Fabrication of $FeF_3$ Nanoflowers on CNT Branches and Their Application to High Power Lithium Rechargeable Batteries.* Advanced Materials, 2010. **22**(46): p. 5260-5264.
78. Badway, F., et al., *Carbon Metal Fluoride Nanocomposites: High-Capacity Reversible Metal Fluoride Conversion Materials as Rechargeable Positive Electrodes for Li Batteries.* Journal of The Electrochemical Society, 2003. **150**(10): p. A1318-A1327.
79. Li, L., et al., *Origins of Large Voltage Hysteresis in High-Energy-Density Metal Fluoride Lithium-Ion Battery Conversion Electrodes.* Journal of the American Chemical Society, 2016. **138**(8): p. 2838-2848.
80. Ko, J.K., et al., *Transport, Phase Reactions, and Hysteresis of Iron Fluoride and Oxyfluoride Conversion Electrode Materials for Lithium Batteries.* ACS Applied Materials & Interfaces, 2014. **6**(14): p. 10858-10869.
81. Hua, X., et al., *Comprehensive Study of the $CuF_2$ Conversion Reaction Mechanism in a Lithium Ion Battery.* The Journal of Physical Chemistry C, 2014. **118**(28): p. 15169-15184.
82. Sina, M., et al., *Investigation of SEI Layer Formation in Conversion Iron Fluoride Cathodes by Combined STEM/EELS and XPS.* The Journal of Physical Chemistry C, 2015. **119**(18): p. 9762-9773.
83. Wang, X., et al., *Carbon Nanotube–$CoF_2$ Multifunctional Cathode for Lithium Ion Batteries: Effect of Electrolyte on Cycle Stability.* Small, 2015. **11**(38): p. 5164-5173.
84. Gu, W., et al., *Lithium–Iron Fluoride Battery with In Situ Surface Protection.* Advanced Functional Materials, 2016. **26**(10): p. 1507-1516.
85. Kim, H., et al., *In Situ Formation of Protective Coatings on Sulfur Cathodes in Lithium Batteries with LiFSI-Based Organic Electrolytes.* Advanced Energy Materials, 2015. **5**(6): p. 1401792-n/a.
86. Wang, F., et al., *Ternary metal fluorides as high-energy cathodes with low cycling hysteresis.* Nat Commun, 2015. **6**.

# LIST OF PUBLICATIONS

**Daniel, G.,** Qiao, H., Alexandre, M., Anirudh, R., Nasr, B., & Gleb, Y. Mixed Metal Difluorides as High Capacity Conversion-Type Cathodes: Impact of Composition on Stability and Performance. *Advanced Energy Materials*, 1800213. doi:doi:10.1002/aenm.201800213

Nitta, N., Lei, D., Jung, H.-R., **Gordon, D.,** Zhao, E., Gresham, G., Yushin, G. (2016). Influence of Binders, Carbons, and Solvents on the Stability of Phosphorus Anodes for Li-ion Batteries. *ACS Applied Materials & Interfaces, 8*(39), 25991-26001. doi:10.1021/acsami.6b07931

Ramanujapuram, A., **Gordon, D.**, Magasinski, A., Ward, B., Nitta, N., Huang, C., & Yushin, G. (2016). Degradation and stabilization of lithium cobalt oxide in aqueous electrolytes. *Energy & Environmental Science, 9*(5), 1841-1848. doi:10.1039/C6EE00093B

Wu, F., Zhao, E., **Gordon, D.**, Xiao, Y., Hu, C., & Yushin, G. (2016). Infiltrated Porous Polymer Sheets as Free-Standing Flexible Lithium-Sulfur Battery Electrodes. *Advanced Materials, 28*(30), 6365-6371. doi:10.1002/adma.201600757

**Gordon, D.**, Wu, M. Y., Ramanujapuram, A., Benson, J., Lee, J. T., Magasinski, A., Nitta, N., Huang, C., Yushin, G. (2016). Enhancing Cycle Stability of Lithium Iron Phosphate in Aqueous Electrolytes by Increasing Electrolyte Molarity. *Advanced Energy Materials, 6*(2), 1501805. doi:10.1002/aenm.201501805

Boukhalfa, S., **Gordon, D.**, He, L., Melnichenko, Y. B., Nitta, N., Magasinski, A., & Yushin, G. (2014). In Situ Small Angle Neutron Scattering Revealing Ion Sorption in Microporous Carbon Electrical Double Layer Capacitors. *ACS Nano, 8*(3), 2495-2503. doi:10.1021/nn406077n